# Characterization of electrical properties and defects in Er- and Yb-doped ZnO thin films grown by sol-gel spin coating

by

**Mohammed Elagib Ibrahim Ahmed**

Submitted in partial fulfilment of the requirements for the degree

Doctor of Philosophy (PhD) in Physics

in the Department of Physics

in the Faculty of Natural and Agricultural Sciences

University of Pretoria

Pretoria

February 2023

Supervisor: Prof. Jackie M. Nel

Co-Supervisor: Prof. Walter E. Meyer

# Declaration

I, Mohammed Elagib Ibrahim Ahmed declare that the thesis, which I hereby submit for the degree Philosophiae Doctor at the University of Pretoria, is my own work and has not previously been submitted by me for a degree at this or any other tertiary institution.

SIGNATURE: 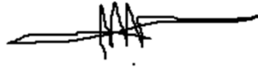

DATE: 07/02/2023

# Characterization of electrical properties and defects in Er- and Yb-doped ZnO thin films grown by sol-gel spin coating

by
Mohammed Elagib Ibrahim Ahmed

## Abstract

ZnO thin films have been used in various applications such as optoelectronic devices, solar cell window layers, UV detectors and space applications. The devices based on ZnO should be able to operate in harsh radiation conditions and over a wide range of temperatures, so the information of radiation effects on devices performance is required. ZnO is a wide, direct band gap semiconductor, and this makes it a good candidate for optoelectronic devices and an ideal host lattice for doping by rare-earth elements such as Er and Yb.

In this study, the effect of rare-earth (Er and Yb) doping and co-doping of ZnO thin films deposited using a sol-gel spin coating technique, as well as the temperature dependence of the electrical properties of the Schottky diodes based on these films were investigated. The electrical properties and defects in Er-doped, Yb-doped and (Er, Yb) co-doped ZnO thin films were studied. The effect of alpha particle irradiation on the electrical properties of the Schottky barrier diodes and the resulting defects in the undoped ZnO thin films were also studied.

The SEM images revealed the grain shape of the undoped material changed from spherical shape to rod-shaped after doping by Er and Yb (both 3 at.%). The XRD spectrum exhibited peaks corresponding to the hexagonal wurtzite structure with random orientations in all samples. A sharp peak corresponding to the $E_2$ (high) phonon mode in the Raman spectra confirmed the wurtzite ZnO structure along with other small peaks observed. The films exhibited good transmittance in the visible region and a sharp absorption peak in the UV region. The optical band gap of the films was found to increase as the Er concentration increased, and decreased after co-doping with (Er, Yb) at different concentrations. Photoluminescence spectroscopy of Er and Yb doped found that all samples exhibited strong UV emission and a broad green emission band, with the undoped sample showing weaker green emission. The electrical properties improved through doping with either Er or Yb as well as co-doping of both Er and Yb, and were also found to improve with an increase in the measurement temperature (Schottky barrier height increased and ideality factor decreased). A common defect seen in single crystal ZnO $E_4$ was also detected in the ZnO thin films deposited using the sol-gel spin coating method. Alpha particle irradiation induced new defects in the undoped ZnO thin films, some new and some corresponding to known defects.

# Dedication

To my father, to my brothers and sisters for their encouragement and support

&

To my mother's soul

# Acknowledgements

I would like to extend my appreciation to the following people for their contributions towards the completion of my PhD study:

- My supervisor, Prof. Jackie M. Nel and co-supervisor, Prof. Walter E. Meyer for all the guidance, support and discussions.
- Prof. F. D. Auret for his guidance and discussions during my study.
- The head of Physics Department, Prof. C. Theron.
- Dr. Mustaffa Ahmed, Dr. Benard, Dr. Helga, Dr. Malven, Mr. J. Janse van Rensburg, Mr. Matshisa Legodi and Mr. Abdulraoof for their help with the deposition systems, measuring equipment and discussions.
- Dr. Huzifa Elnour, Dr. Ammar Abdalgabar and Dr. Mohammed Daffa Allah for their encouragement and support.
- My colleagues in the Physics Department of the University of Pretoria for their support and encouragement.
- University of Free state for their help with PL measurements.
- Prof. M. Diale for the UV-Vis measurements.
- Prof. M. Rademeyer, Dr. F. Malan at the Chemistry Department for the XRD measurements.
- Sudan University of Science and Technology and Ministry of Higher Education and Scientific Research for financial support.
- My father, my sisters and my brothers for their encouragement and support.

# Contents

**Declaration** I

**Dedication** III

**Acknowledgements** IV

**1 Introduction** 1

1.1 Research motivation . . . 2

1.2 Aim and objectives of this Research . . . 2

1.3 Thesis layout . . . 3

**2 Theoretical aspects** 4

2.1 Introduction . . . 4

2.2 ZnO crystal structure . . . 4

2.3 Band gap structure . . . 6

2.4 ZnO lattice dynamics . . . 7

2.5 ZnO thin films growth techniques . . . 8

2.6 Rare-earth (Er and Yb) doped ZnO thin films . . . 10

2.7 Metal-semiconductor contacts . . . 11

2.8 Current transport mechanisms . . . 19

2.9 Defects in semiconductor materials . . . 22

2.10 Deep-level transient spectroscopy (DLTS) . . . 27

**3 Experimental and characterization techniques** 33

3.1 Introduction . . . 33

3.2 Samples preparation . . . 33

3.3 ZnO thin film characterization . . . . . . . . . . . . . . . . . . . . . . . . . . 38

**4 Results and discussion** **49**

4.1 Structural and optical characterization and the effect of alpha particle irradiation on the electrical properties of ZnO thin films prepared by sol-gel spin coating . . . . . . . . . . . . . . . . . . . . . . . . . . . . . . . . . . . . . 49

4.2 Effect of Er and Yb doping and temperature on electrical properties of ZnO thin films Schottky diode prepared by sol-gel spin coating . . . . . . . . . . . . 60

4.3 Structure and optical properties of Er-doped ZnO thin films prepared by sol-gel spin coating, and electrical properties of Schottky diodes prepared thereon . . . 74

4.4 Structure and optical properties of (Er, Yb) co-doped ZnO thin films prepared by sol-gel spin coating, and electrical properties of Schottky diodes prepared thereon . . . . . . . . . . . . . . . . . . . . . . . . . . . . . . . . . . . . 88

**5 Conclusions and future work** **97**

5.1 Conclusion . . . . . . . . . . . . . . . . . . . . . . . . . . . . . . . . . . . 97

5.2 Future work . . . . . . . . . . . . . . . . . . . . . . . . . . . . . . . . . . 99

**Bibliography** **115**

# Chapter 1

# Introduction

Zinc oxide (ZnO) is one of the II-VI semiconductor materials with a wide direct band gap of approximately 3.4 eV and a large exciton binding energy of 60 meV at room temperature [1]. It has interesting electrical properties such as high electron mobility, high electron saturation velocity and good thermal stability, as well as being highly resistant to radiation damage, making it an excellent candidate for optoelectronic devices and space applications [2]. Pure ZnO is a white powder. However in the nature, occurs as the rare mineral zincite in the earth's crust, which usually contains a certain amount of manganese and other impurities and it is yellow to red colour [3]. It almost insoluble in the water, but it will dissolve in any alcohol solvent and most acids [4, 5]. This material crystallizes in three types of lattice structures wurtzite structure, zinc blende and the rock-salt. The most common form is wurtzite that is a thermodynamically stable phase under ambient conditions.

In the industrial applications, ZnO has been used as a white pigment since 1835 [6], and is produced in hundreds of thousands of tons for use in paints, additive for rubber and plastics, catalysts, ceramics, pharmaceuticals and cosmetics (sun creams), and coating material for paper [7]. In the form of thin films, it is used in technical applications such as optoelectronic devices like transparent electrodes and solar cell as window layers, gas sensors, varistors, photocatalysts, spintronic devices and nanolasers [8]. Several deposition techniques can be employed, include sputtering, pulsed laser deposition, chemical vapour deposition, electrochemical deposition, spray pyrolysis, hydrothermal method and sol-gel. Among these techniques, the sol-gel process is widely used for ZnO thin film deposition due to several advantages. For example, the ability to prepare high-quality thin films on a large scale, the excellent control of stoichiometry, simplicity, safety, low-cost type of equipment resulting in smooth and homogeneous thin films [7].

ZnO is a very attractive host lattice for doping with different elements to tailor the optical, electrical and magnetic properties, due to its excellent physical and chemical stability [9]. Rare-earth elements have been used as dopants for many applications, for example, opto-electronic devices such as visible and infra-red luminescent devices, based on their optical emission occurring with 4f-4f shell transitions [10, 11].

## 1.1 Research motivation

The study of the electrical properties of ZnO, semiconductor-based devices are required, for example, metal-semiconductor interface, p-n junction, heterojunction interface and metal-oxide-semiconductor devices [12]. For these applications, metal-semiconductor contacts (M-S) have been used to produce either ohmic or Schottky contacts. Fabrication of high performance ZnO-based devices requires deposition of high-quality Schottky barrier diodes. To obtain high-quality Schottky barrier diodes is difficult since it depends on several conditions such as the quality of the interface between ZnO surface and metal, as well as surface states and defects in the semiconductor [13]. Undoped ZnO is rich in native (intrinsic) point defects, such as oxygen vacancies, $V_o$, and zinc interstitials, $V_i$. These defects are believed to contribute to the n-type conductivity of ZnO. The green emission of ZnO in photoluminescence originates from the oxygen vacancies, which could be significantly affected by dopant incorporation, post-annealing and preparation conditions [14].

Although Sol-gel spin coated ZnO films have been studied before, that the electrical properties of the films grown using this technique have not been studied extensively. It is important to understand the electrical properties and the effects of doping and irradiation on these electrical properties for future applications. In this study the material's electrical properties were good enough that, for the first time deep-level transient spectroscopy could be used to study the defects in sol-gel spin coated undoped, Er-doped and Yb-doped ZnO thin films. The studied ZnO thin films can used in optoelectronic devices, UV detectors, photodiode and photosensor and gas sensors.

## 1.2 Aim and objectives of this Research

The aim and objectives of this work are stated in the following points:

- Doping of ZnO thin films with rare-earth elements such as Er and Yb in order to study

their effect on the electrical properties of the Schottky diodes, the morphology, structure and optical properties of undoped, Er-doped and Yb-doped ZnO thin films also formed part of this research.

- Investigate the temperature dependence of the electrical properties at different temperatures on Er-doped and Yb-doped ZnO thin films.
- Identify the native electrical defects in ZnO, Er-doped and Yb-doped ZnO, as well as the irradiation-induced defects in undoped ZnO. Due to possible space applications, the devices based on ZnO should be able to operate in harsh radiation conditions, and information of radiation effects on device performance is required.

Sol-gel spin coating has been used to prepare undoped and doped ZnO thin films, and several techniques have been used to characterize the ZnO thin films, these include scanning electron microscopy (SEM) for surface morphology, XRD for structure, Raman spectroscopy, photoluminescence and UV-Vis for optical properties, current-voltage ($I$-$V$) and capacitance-voltage ($C$-$V$) for electrical properties, DLTS and Laplace DLTS for defect identification in undoped, Er-doped and Yb-doped ZnO thin films.

## 1.3 Thesis layout

This thesis contains five chapters. Chapter 1 is an Introduction. Chapter 2 covers the theoretical aspects of the properties of ZnO, metal-semiconductor contacts, defects in semiconductors and DLTS technique. The experimental techniques used in this work are given in Chapter 3. The results and discussion obtained during this work are presented in Chapter 4. Chapter 5 gives the conclusion of the study.

# Chapter 2

# Theoretical aspects

## 2.1 Introduction

In this chapter theoretical aspects of semiconductors with particular reference to ZnO is discussed. The crystal structure of ZnO, band gap structure and ZnO lattice dynamics are presented in Section 2.2 to 2.4. The growth techniques of ZnO thin films and doping of ZnO by rare-earth such as Er and Yb are presented in Section 2.5 to 2.6. Metal-semiconductor contacts such as Schottky and ohmic contacts, and the extraction of the electrical parameters of Schottky barrier diode from *I-V* and *C-V* measurements are described in Section 2.7. Section 2.8 discusses the current transport mechanisms through the metal-semiconductor junction. The defects in semiconductor materials are presented in Section 2.9. Deep-level transient spectroscopy (DLTS) and Laplace-transform deep-level transient spectroscopy (L-DLTS) is described in Section 2.10.

## 2.2 ZnO crystal structure

ZnO is a semiconductor materials compound of the group-$II^b$ element ($_{30}Zn$) and the group VI element ($_{8}O$). Zn has five isotopes; the common ones are $^{64}Zn$ (48.89%), $^{66}Zn$ (27.81%), and $^{68}Zn$ (18.57%). All these isotope are stable, whereas $O_2$ consists of the isotope $^{16}O$ (99.76%). Zn has the electron configuration $(1s)^2(2s)^2(2p)^6(3s)^2(3p)^6(3d)^{10}(4s)^2$. The oxygen configuration is $(1s)^2(2s)^2(2p)^4$ [15].

A crystal structure is created when atoms are uniquely arranged in a crystal. ZnO has three types of lattice structures shown in Figure 2.1, the rock-salt, zinc blende and wurtzite structure. The rock-salt can be obtained from wurtzite at relatively high pressures of about 9 GPa [16]. Zinc blende structure can be stabilized only by growth on cubic substrates. Wurtzite structure

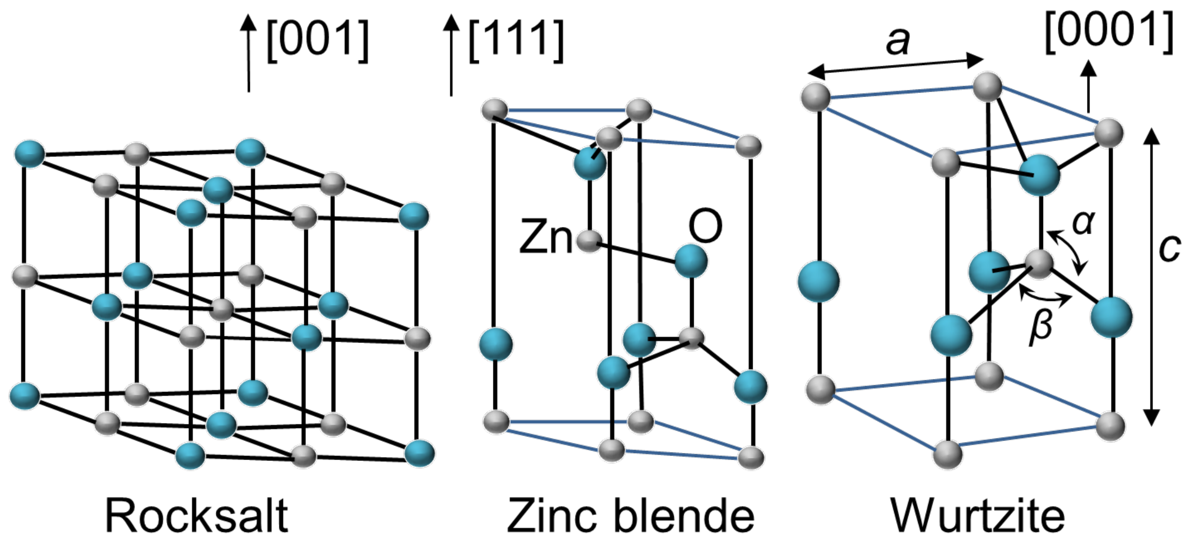


Figure 2.1: ZnO crystal structures. Redrawn from ref [17].

is a thermodynamically stable phase under ambient conditions, thus it is most common. In ZnO wurtzite lattice (see Figure 2.1), each zinc atom is surrounded by four nearest neighbour oxygen atoms at the corners of a tetrahedron and vice versa [18]. The wurtzite structure has a hexagonal unit cell with two lattice parameters $a$ = 3.249 Å and $c$ = 5.207 Å in the ratio $c/a$ = 1.63 corresponding to the space group $C^4_{6v}$ (in the Schoenflies notation) or *P63mc* (in the Hermann-Mauguin notation) [15, 19]. In a real ZnO crystal, the wurtzite structure deviates from the ideal arrangement by changing the c/a ratio or the value of internal parameters (nearest-neighbor distance) [19]. The variation between the zinc blende and wurtzite structures is that the zinc blende is cubic, while the wurtzite is a distortion of the cube in the [111] direction [20]. ZnO has a partially ionic character. Although the wurtzite tetrahedral coordination is ideal for $sp^3$ covalent bonding nature, the ionic property of ZnO tends to increase the band gap, and it is responsible for the preferred formation of wurtzite structure rather than zinc blende structure. ZnO also has a strong piezoelectric character. The tetrahedral coordination gives rise to the polar symmetry along the hexagonal axis. This polarity gives rise to several properties of ZnO. The wurtzite ZnO have four common face terminations. Two are polar, Zn terminated (0001), the O terminated $(000\bar{1})$ faces (c-axis oriented), and two non-polar $(11\bar{2}0)$ (a-axis) and $(10\bar{1}0)$ faces, which both contain an equal number of Zn and O atoms [21]. The polar faces have different chemical and physical properties. The O-face has a slightly different electronic structure from the other three faces [22].

## 2.3 Band gap structure

All semiconductors have a forbidden energy region in which allowed electron states are not present, this is called the band gap. The allowed electron states are present in two bands. Above the band gap is the conduction band, and below is the valence band (see Figure 2.2).

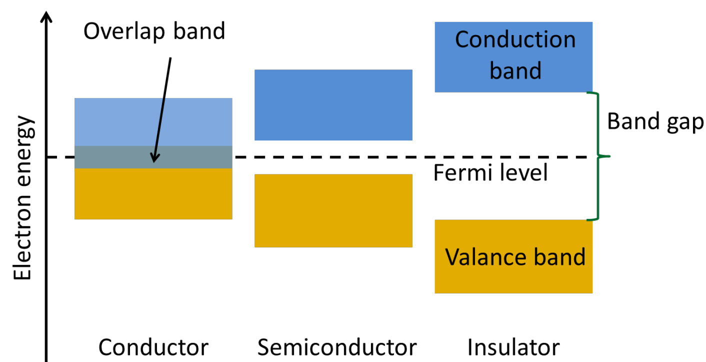


Figure 2.2: Band gap energy diagram of the conductor, semiconductor and an insulator. Redrawn from ref [23].

The band gap is defined as the minimum energy required to excite an electron from the valence band to the conduction band [24]. The band structure varies from one solid to another, and this variation plays an important role and is responsible for the wide range of electrical characteristics in different materials [25]. The concept of energy bands can be used to define three types of solids. Metals, semiconductors and insulators. There is no band gap in metal because the conduction band either overlaps the valence or is partially filled. Semiconductor materials have a band gap separating a filled valence band from an empty conduction band, so the band structure of semiconductors at 0 K is basically the same structure as for insulators [25]. The difference between semiconductors and insulators lies in the size of the band gap. The band gap in semiconductors the order of 1 eV, whereas in insulators, the energy band gap is in the range of 5 - 15 eV [26].

The ZnO binding in its crystal lattice involves $sp^3$ hybridization of the electron states, leading to four equivalent orbitals, directed in a tetrahedral geometry. In the resulting semiconducting crystal, the bonding sp3 states constitute the valence band, while the conduction band originates from its antibonding counterpart. The resulting energy gap is 3.4 eV, i.e., in the UV spectral range, which has triggered interest in ZnO as a material for transparent electronics [15].

The ZnO binding in its crystal lattice involves $sp^3$ hybridization of the electron states, leading to four equivalent orbitals, directed in a tetrahedral geometry. In the resulting semiconducting crystal, the bonding $sp^3$ states constitute the valence band, while the conduction band ori-

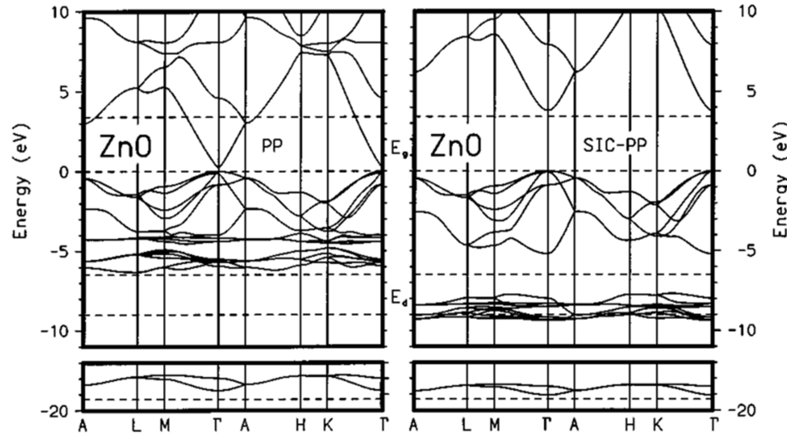


Figure 2.3: LDA bulk band structure of ZnO as calculated using standard pseudopotentials (PP) method on the left panel and self-interaction-corrected pseudopotentials (SIC-PP) method on the right panel. All energies are measured with respect to the top of the valence band. The horizontal dashed lines indicate the measured gap energy [27].

ginates from its antibonding counterpart. The resulting energy gap is 3.4 eV, i.e., in the UV spectral range, which has triggered interest in ZnO as a material for transparent electronics [15].

Different theoretical approaches and several experimental techniques have been used to determine the band structure of wurtzite ZnO. These techniques including the X-ray (photoelectron spectroscopy and resonant x-ray emission spectroscopy), UV (reflection/absorption or emission) techniques. These techniques measure the energy difference by inducing transitions between electronic levels. Another technique used to calculate the band structure is angle-resolved photoelectron spectroscopy [19]. Some of the theoretical calculation methods of the band structure of ZnO using pseudopotentials methods are based on the local-density approximation (LDA). Figure 2.3 shows the LDA bulk band structure of ZnO as calculated using standard pseudopotentials (PP) and self-interaction-corrected pseudopotentials (SIC-PP) methods [27].

## 2.4 ZnO lattice dynamics

The wurtzite structure of ZnO belongs to the $C_{6v}^{4}$ (*P63mc*) space group, both the Zn and O atoms occupying $C_{3v}$ sites [28]. The wurtzite ZnO has 4 atoms per unit cell, leading to 12 phonon modes. These modes are useful for understanding the optical, thermal and electrical properties of the Wurtzite ZnO crystal. The phonon modes belong to the 3 acoustic modes (one longitudinal acoustic (LA), two transverse-acoustic (TA)) and 9 optical phonons (three longitudinal-optical (LO) and six transverse-optical (TO) branches). At the center of the Bril-

louin zone (Γ point) (see Figure 2.4), group theory predicts the following lattice optical phonons have the following irreducible representation [29]:

$$\Gamma_{opt} = 1A + 2B + 1E + 2E_2, \tag{2.1}$$

where the 1A and 1E branches (polar modes) are Raman and infrared active, which may be split into longitudinal (LO) and transversal (TO) optical phonon with different frequencies due to macroscopic electric fields associated with the (LO) phonons. The two $E_2$ branches (non-polar) are Raman active only. The $E_2$ (low) mode is related to the Zn sublattice, whereas the $E_2$ (high) mode is associated with the motion of oxygen atoms [30]. The $B_1$ (low) and $B_1$ (high) branches are inactive or silent modes [31].

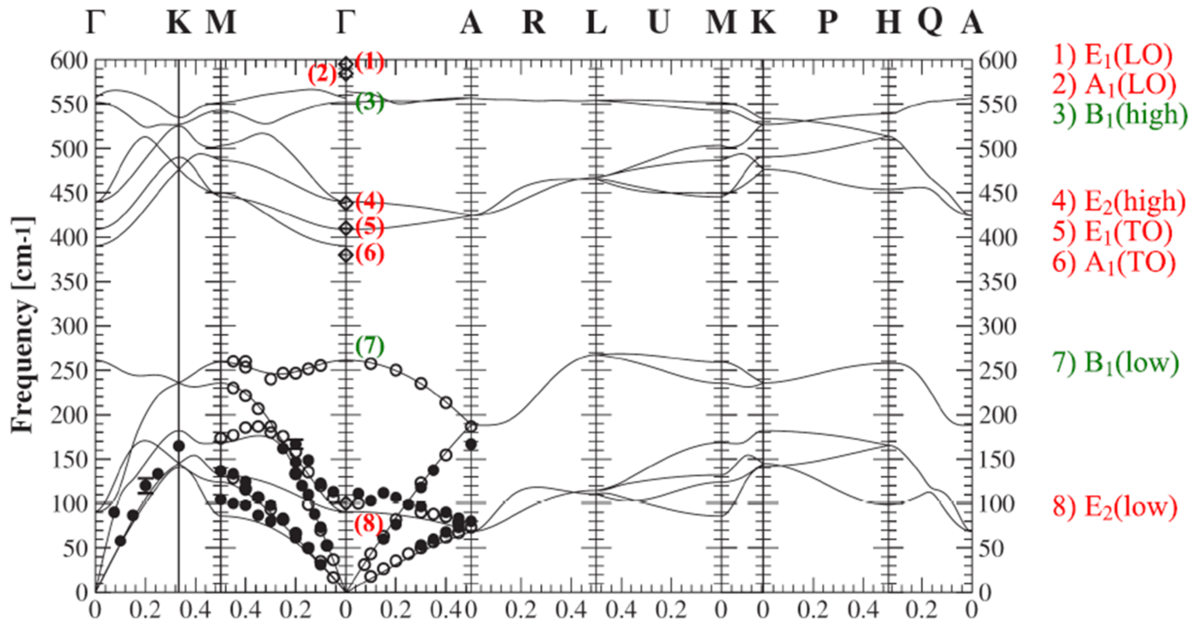


Figure 2.4: Phonon dispersion relationship of wurtzite zinc oxide is calculated at Γ point in the specified direction of the Brillouin zone center by using the lattice dynamics equation. Molecular vibration represented by red font ($E_1$, $E_2$, $A_1$) can be observed through Raman scattering, while $B_1$ mode represented by green font can't be observed through Raman scattering. [32].

## 2.5 ZnO thin films growth techniques

ZnO is obtainable as thin films, nanorods and as bulk single crystals. Thin film is defined as a low-dimensional material fabricated by precipitating atomic, molecular or ionic species of matter. The thickness of the films is typically less than several microns [33]. Thin film materials are used in a wide range of industrial applications, such as protective, conductive or

photoactive layers, as dry lubricants, as catalysts, as gas separation membranes, and as optical layers. The thin film parameters such as film composition, crystal orientation, film thickness, and microstructure depend on the deposition conditions. The deposition of thin films involves three main steps [33]:

1. Production of the appropriate atomic, molecular or ionic species.
2. Transport of these species to the substrate through a medium.
3. Condensation on the substrate, either directly or via a chemical or electrochemical reaction to form a solid deposit.

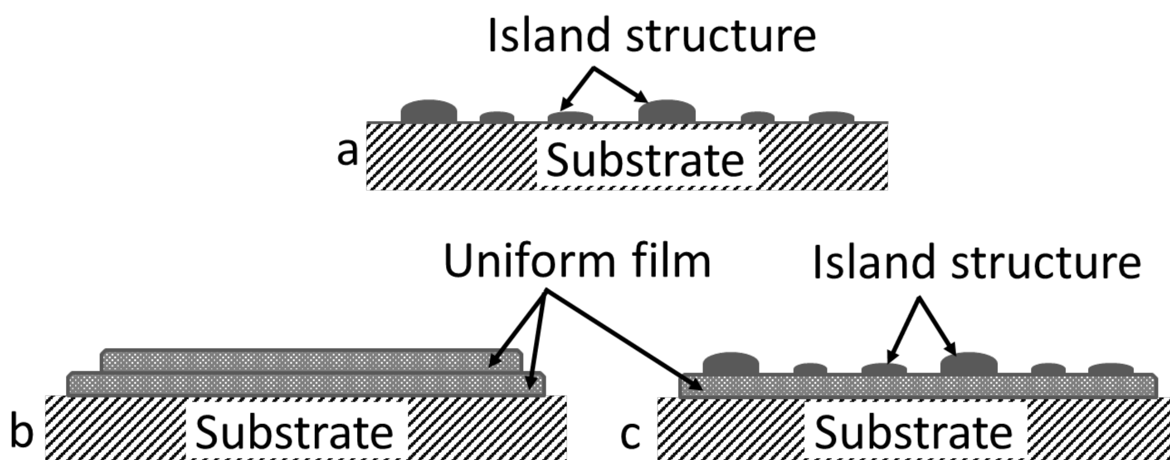


Figure 2.5: The modes of thin films growth processes (a) Volmer-Weber type (b) Frank-van der Merwe type (c) Stranski-Krastanov type. Redrawn from ref [33].

There are three modes of the thin film growth process depending on the thermodynamic parameters of the deposited and the substrate surface, these modes namely, island type, known as Volmer-Weber type (see Figure 2.5 (a)), layer type, known as Frank-van der Merwe type (see Figure 2.5 (b)), and mixed type, known as Stranski-Krastanov type (see Figure 2.5 (c)).

A variety of techniques have been used to synthesis ZnO thin films, which include pulsed laser deposition, chemical vapour deposition, electrochemical deposition, spray pyrolysis, hydrothermal method, and sol-gel [7, 34–39]. From these techniques, sol-gel deposition is preferred in the preparation of high-quality ZnO thin films due to the low cost equipment required, the resulting homogeneous and relatively smooth thin films, the simplicity and ability to deposit large area films, and easily controlled film thickness by controlling the number of spin coating and pre-annealing cycles [40, 41]. The sol-gel network properties depend on several factors, including pH, temperature, reaction time, reagent concentration, nature and

concentration of the catalyst, aging temperature and time and the drying process. These factors affect the rate of hydrolysis and condensation reaction. The sol-gel process generally involves four stages: hydrolysis, condensation and polymerization of monomers for particle formation, growth of particles, and agglomeration of particles [4].

Evaluation of the properties of thin films and correlation between growth conditions and the properties of the resultant thin film are important to study [42], since it has been shown that the growth conditions influence the properties of the film, but these resulting properties also influence other properties [33], as summarised in Figure 2.6.

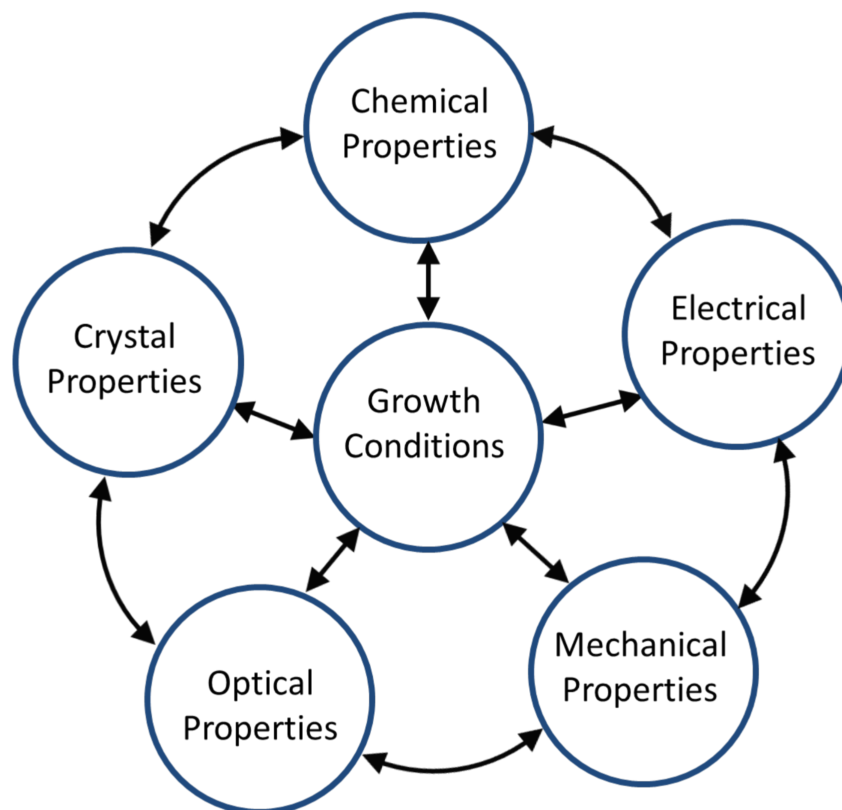


Figure 2.6: Correlations between growth conditions and the properties of the resultant thin films. Redrawn from ref [33].

## 2.6 Rare-earth (Er and Yb) doped ZnO thin films

Improving the properties of ZnO thin films as a technological material for applications such as optoelectronic devices is possible by tuning their behavior when adding impurities [43]. Dopants in nanocrystals of semiconductors lead to phenomena not found in the bulk because their electronic states are confined to a small volume. For example, n- or p-type dopants

can auto-ionize without thermal activation. This occurs because a carrier inside the crystal occupies one of the confined electronic states, which increases in energy with decreasing nanocrystallite size. The confinement energy below a critical radius exceeds the Coulomb interaction between the ionized impurity and the carrier, which automatically occupies a nanocrystal state [44]. ZnO is an ideal host lattice for doping with rare-earth elements to improve the optical, electrical and magnetic properties due to its wide band gap 3.4 eV, high exciton binding energy (60 meV) at room temperature and its excellent physical and chemical stability [45]. ZnO doped by rare-earth elements are important materials and have been used for many applications, such as optoelectronic devices including visible (blue, green, and red) and infrared luminescent devices, spintronic, and photocatalytic application, UV-light emitting diodes and laser diodes [14, 45]. Rare-earth elements have intense emission peaks in the visible and near IR region due to their 4f intra-shell transitions that can generate narrow and intense emission lines [46, 47]. Many studies focus on rare-earth element such as (Er and Yb) doped ZnO to enhance the structure and optical properties using different techniques [48–52]. Whereas only a few research studies reported the effect of rare-earth doping on electrical properties of Schottky diodes based-on ZnO. M.A.M Ahmed *et al.* [53] investigated the effect of Sm doping ZnO nanorods on structural optical and electrical properties of Schottky diodes and reported that Sm-doped ZnO nanorods improved the rectification behavior of Schottky diodes. M.A.M Ahmed *et al.* [54] also reported the influence of (Ce and Sm) co-doping ZnO nanorods on the structural, optical and electrical properties of the fabricated Schottky diode. In our studies, the interest is focused on the effect of Er and Yb doping on the electrical properties and electrical defects using Schottky diodes on ZnO thin films.

## 2.7 Metal-semiconductor contacts

The metal-semiconductor contact, discovered by Braun in 1874, forms the basis of one of the oldest semiconductor devices. Schottky developed the first acceptable theory in 1930. In his honor, metal-semiconductor devices are frequently referred to as Schottky barrier devices. Usually this name denotes the use of these devices as rectifiers with distinctly non-linear current-voltage characteristics [55].

In order to understand the electrical properties of semiconductor materials, different types of semiconductor-based devices are used, such as metal-semiconductor interface, p-n junction, heterojunction interface, and metal-oxide-semiconductor structure [12]. Among these devices, metal-semiconductor contacts (M-S) have been used to produce devices such as Schottky barrier diodes (SBDs). High performance ZnO-based SBDs require fabricating high-quality

of Schottky barrier diodes. This not an easy task since the quality of Schottky barrier diodes depends on the quality of the interface between the ZnO surface and the metal. Residual surface contamination and defects in semiconductors have an effect on the quality of these diodes [13].

### 2.7.1 Schottky contacts

A Schottky contact is a metal-semiconductor contact that allows electrical current to flow easily in one direction (in the forward biased mode), and allows negligible or no current to flow in other direction (the reverse bias). Schottky contacts are also known as rectification contacts. An ideal Schottky contact (ignoring the effects of surface and interface states) is created when a difference in potential is present between the Fermi energy level of the metal and the band edge where majority charge carriers reside [23]. The difference in potential between the Fermi energy level of the metal (Pd) and semiconductor (ZnO) form a barrier of height $\phi_b$. For n-type semiconductors, the Schottky barrier height is predicted by [56].

$$\phi_b = \Phi_m - \chi_s, \tag{2.2}$$

where $\chi_s$ is the electron affinity of semiconductor. $\Phi_m$ is the work function of metal, defined as the amount of energy required to raise an electron from the Fermi level to a state of rest outside the surface of the metal (vacuum level). In a semiconductor, the work function is the energy difference between the Fermi level and the vacuum level. It is a variable quantity because the Fermi level in the semiconductor varies with the doping [57]. The work function of semiconductor is related to electron affinity as [58]:

$$\Phi_s = \chi_s + \xi, \tag{2.3}$$

where $\xi$ is the energy difference between the Fermi level and the bottom of the conduction band.

The barrier height for p-type semiconductors is given by the difference between the valence band edge and the Fermi level in the metal [23]:

$$\phi_b = \frac{E_g}{q} + \chi_s - \Phi_m. \tag{2.4}$$

Figure 2.7 shows the energy band diagrams of metal and n-type semiconductor contacts in an ideal case. Figure 2.7 (a) on the left side shows the metal and semiconductor separated

from each other (not in contact). As can be seen, the semiconductor has no charges at the surface so that the band structure of the surface is the same as that of the bulk and there is no band bending [57]. After metal and semiconductor contact together (see Figure 2.7 (b) on the left), and due to the difference in the work function between the metal and semiconductor, the free electrons will flow between the metal and semiconductor. If the metal work function $\Phi_m$ is greater than that of the semiconductor $\Phi_s$, that is, $\Phi_m > \Phi_s$ and assuming that there are no surface states present. The electrons will pass from the semiconductor to the metal. Then, the Fermi levels of the metal ($E_{F,m}$) and semiconductor ($E_{F,s}$) will align [59]. Under equilibrium (see Figure 2.7 (c) on the left), a Helmholtz double-layer will be established at the metal/semiconductor interface, where the metal which is negatively charged is balanced by a positive charge in the semiconductor near its surface due to electrostatic induction [60].

Figure 2.7 on the left describes the ideal metal-semiconductor Schottky contact without interface layer. According to Schottky-Mott theory, the barrier height depends on the metal work function (Equation 2.2), and this is valid for ideal Schottky contacts. But in experimental contacts it is found that the barrier height is a less sensitive function or independent of the metal work function. Bardeen explains and suggested that the difference between the theoretical and experimental value of the barrier may be due to the effect of surface states. Suppose that the metal and semiconductor remain separated by a thin insulating layer, as shown in Figure 2.8. In an actual Schottky contact, there are chemical reactions between the metal and the semiconductor that led to disturbing the periodic nature of semiconductor crystal at the interface, this causes an interface stats in the band gap of the semiconductor near the interface. One of the interface types creates between the semiconductor and the metal is a thin film of native oxide layer (interfacial layer or insulating layer) created during the surface preparation of a highly polarizable semiconductor [57, 61]. The interfacial layer is very thin in thickness of 10 to 20 Å thick. Therefore, the electrons can easily tunnel through it [62].

Experimentally, many studies reported the wide and variable range values of Schottky barrier heights based on ZnO measured using the same metal contacts. This shows that the barrier height is affected by many factors such as insulating interfacial layers, surface states, defects and the image force barrier lowering in the actual Schottky contact [58]. Table 2.1 shows a variation in Schottky barrier height (SBH) values based on ZnO measured by different techniques, using various deposition techniques of metal contacts.

Schottky contacts can be used in device applications such as rectifiers, mixers, microwave receiver detectors and field effect transistors [63]. The Schottky contacts can also be used to form a space charge region that can be used to investigate the semiconductor energy band gap and measure the properties of the deep-level defects present at and below the M-S interface.

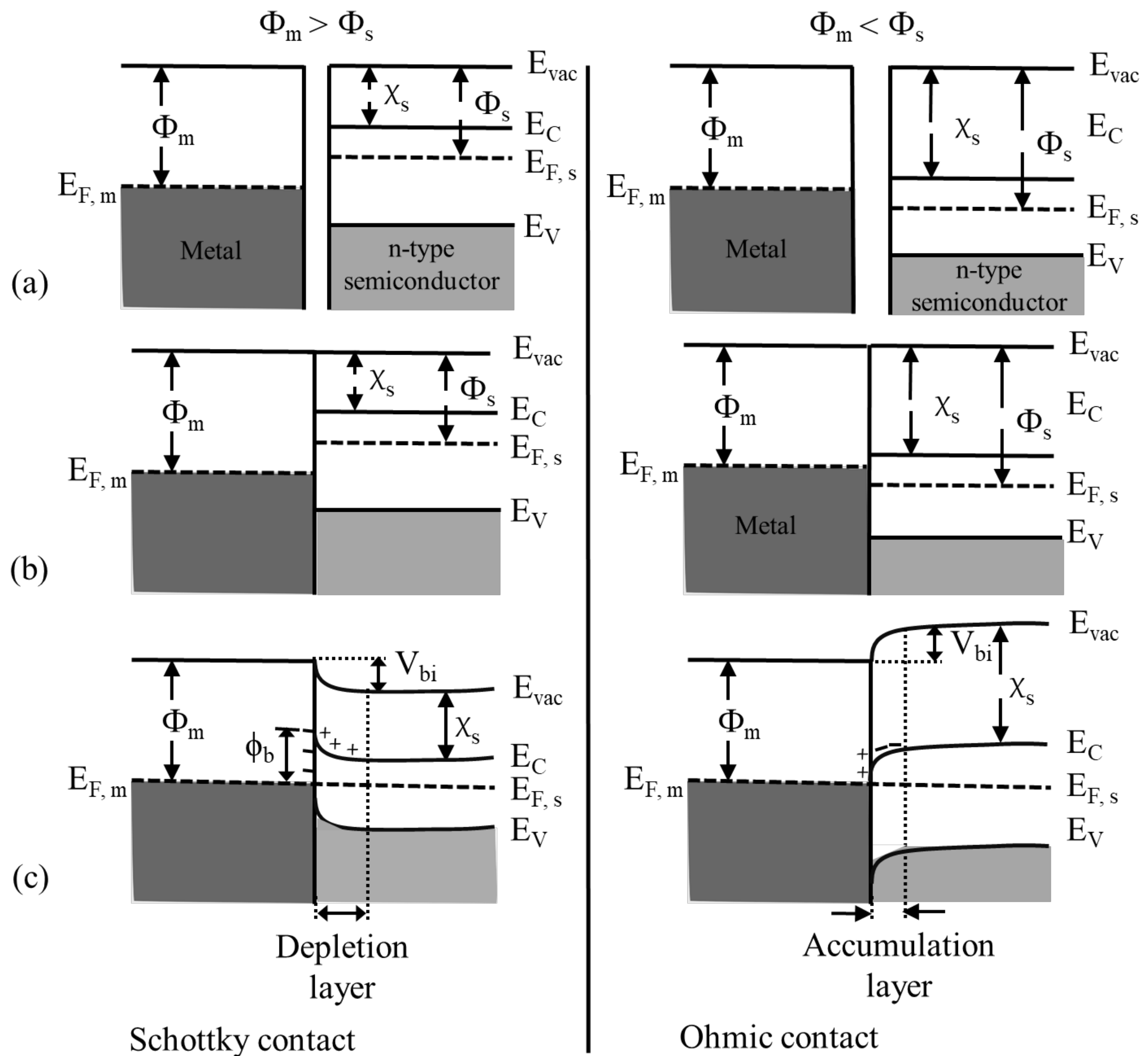


Figure 2.7: Energy band diagrams of metal and n-type semiconductor contacts (a) not in contact (b) in contact (c) in contact under equilibrium. Redrawn from ref [60].

The reliability, performance and stability of devices is highly dependent on the interface properties. The quality of the M-S junction is determined by the difference between the Fermi energies of the metal and semiconductor, the processing of the semiconductor before fabrication of the contact and the techniques used in the fabrication of devices.

### 2.7.2 Schottky barrier height under forward and reverse bias

Under zero bias conditions (V = 0), the electrons in the metal and semiconductor have the same barrier height relative to their Fermi energy. Thus, there is no nett electron flow over

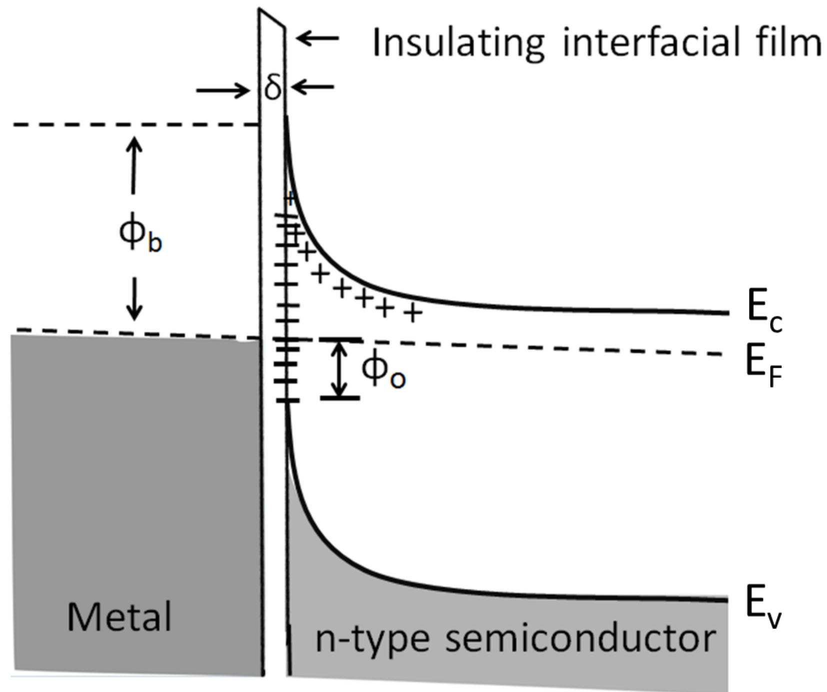


Figure 2.8: Electron energy band diagram of a metal-semiconductor contact with surface states and interfacial layer. Redrawn from ref [57].

Table 2.1: Variation in Schottky barrier height values based on ZnO measured by different techniques.

| Metal | SBH (eV) | Measurement Technique | Deposition Technique | Ref |
|---|---|---|---|---|
| Pd | 0.74 | I-V | Vacuum deposition | [64] |
| Pd | 0.784 | I-V | Resistive evaporation | [54] |
| Pd | 0.67, 0.67 | I-V, H(I) I | Thermal evaporation | [65] |
| Au | 0.59, 0.61 | I-V,C-V | Resistive evaporation | [66] |
| Au | 0.70, 0.73 | I-V, C-V | DC magnetron sputtering | [67] |
| Au | 0.61, 0.92 | I-V, C-V | e-beam deposition | [68] |
| Ag | 0.70, 0.76, 0.68 | lnI-V, H(I)-I, F(V)-V | RF sputtering | [69] |
| Ag | 0.89 and 0.92 | I-V, C-V | e-beam deposition | [70] |
| Ag | 0.85, 1.68 | I-V, C-V | RF sputtering | [13] |
| Pt | 0.65, 0.74, 0.80 | I-V | e-beam deposition | [71] |
| Pt | 0.66, 0.41 | I-V, H(I)-I | Sputtering | [72] |
| Ir | 0.837, 0.837, 0.924 | I-V, F(V)-V, C-V | e-beam deposition | [73] |

the barrier. When a positive bias is applied (see Figure 2.9 (a)) to the metal, the Fermi energy of the semiconductor moves up relative to the Fermi level of the metal, thereby decreasing the barrier height, band bending and disturbing the balance between diffusion and drift. Thus, more electrons will diffuse towards the metal than the number drifting into the semiconductor. This leads to a positive current flow through the junction [23].

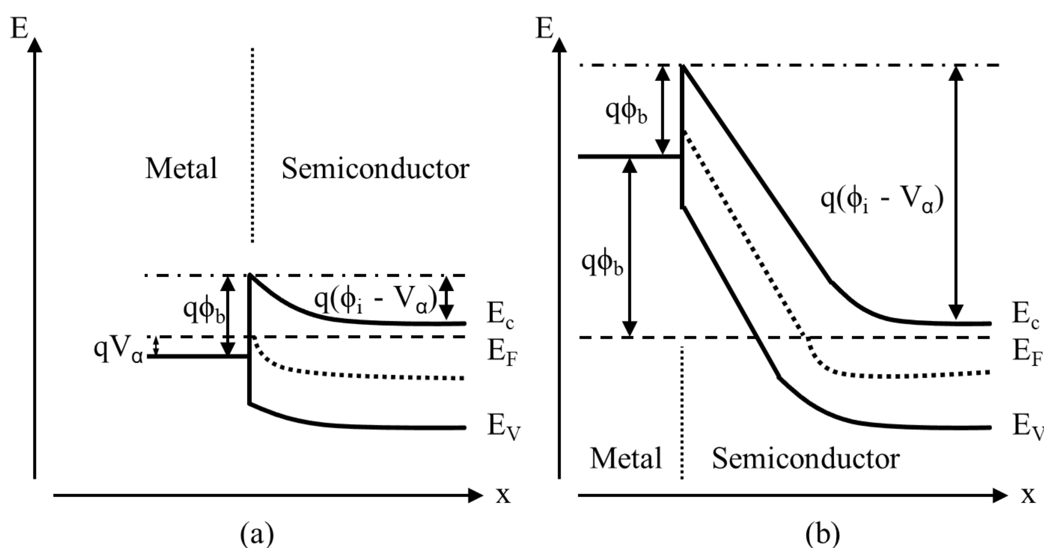


Figure 2.9: Electron energy band diagram of a metal-semiconductor contact under (a) forward bias (b) reverse bias. Redrawn from ref [23].

As reverse bias is applied (see Figure 2.9 (b)), the Fermi level of the semiconductor is lowered (moves down) relative to that of the metal, yielding a larger band bending and an increase in the potential barrier and the depletion region width. Increasing of the barrier makes the flow of the charge carriers over the barrier difficult. So very little or negligible current flows from the semiconductor to the metal under reverse bias. The lower or negligible flow of electrons under reverse bias will continue until the electric field in the depletion region is large enough to cause a dielectric breakdown of the semiconductor. This will result in a large current flow across the barrier, possibly causing irreversible damage to the device [62].

### 2.7.3 Extraction of Schottky barrier height

**i. From current-voltage *(I-V)* measurements:**

From the characteristic *I-V* measurement of a Schottky diode, different parameters such as barrier height, ideality factor and series resistance can be determined. Practically, the real barrier height $\phi_b$ is less than the ideal barrier height $\phi_{b0}$ due to image force barrier lowering and

other factors. Taking into account the image force barrier lowering, the real barrier height is then given by $\phi_b$ = $\phi_{b0}$ - $\Delta\phi_b$, where $\phi_b$ is called effective barrier height. Thermionic emission predicts the current-voltage relationship of Schottky barrier diode (neglecting series and shunt resistance) can be written as [55]

$$I = AA^*T^2 \exp(-\frac{q\phi_b}{kT})[\exp(\frac{qV}{nkT}) - 1] = I_s[\exp(\frac{qV}{nkT}) - 1], \tag{2.5}$$

where $A$ is the diode area, $A^*$ is the Richardson constant = $4\pi qk^2m^*/h^3$ = $120(m^*/m)A/cm^2.K^2$, $\phi_b$ is the effective barrier height, $I_s$ is the saturation current, $T$ is the absolute temperature, $k$ is the Boltzmann constant, $V$ is the bias voltage and $n$ is the ideality factor.

When plotting semilogarithmic $I$ versus $V$, the barrier height $\phi_b$ is calculated from the current $I_s$, determined by extrapolating the semilogarithmic $I$ versus $V$ curve at V = 0. The barrier height $\phi_b$ is calculated from $I_s$ in equation 2.5 according to [55]

$$\phi_b = \frac{kT}{q} ln(\frac{AA^*T^2}{I_s}). \tag{2.6}$$

The ideality factor can be calculated from the slope of the linear region of the curve, and is given as

$$n = \frac{q}{2.3kT[d(lnI/dV)]}. \tag{2.7}$$

**ii. From capacitance-voltage *(C-V)* measurements:**

In capacitance-voltage *(C-V)* measurements, the capacitance of the Schottky diode is measured as a function of applied reverse bias [57]. Under reverse bias, the depletion region capacitance is given by [58]

$$C = A[\frac{\varepsilon_s q N_D}{2(\phi_b - \xi + V_r - kT/q)}]^{1/2}, \tag{2.8}$$

where $A$ is the diode area, $\varepsilon_s$ is the permittivity of the semiconductor, $V_r$ is the applied reverse voltage and $\xi$ is the difference in energy between the Fermi level and the bottom of the conduction band in the bulk semiconductor. Hence

$$C^{-2} = \frac{2(\phi_b - \xi + V_r - kT/q)}{A^2 \varepsilon_s q N_D}, \tag{2.9}$$

The plot of $C^{-2}$ against $V$ gives a straight line and using intercept on the voltage axis.

The barrier height is given as

$$\phi_b = V_{bi} + \xi + kT/q, \tag{2.10}$$

where $V_{bi}$ is the built-in potential, the $kT$ factor comes from the contribution of majority carriers to the space charge. Equation 2.10 does not include the image force barrier lowering $\Delta\phi_b$. Thus, if we take $\Delta\phi_b$ into account, the Equation 2.10 can be given as [74]

$$\phi_b = V_{bi} + \xi + kT/q - \Delta\phi_b. \tag{2.11}$$

### 2.7.4 Ohmic contacts

A metal-semiconductor contact has ohmic behavior if there is no barrier formed between the metal and semiconductor. With an ohmic contact, the current-voltage characteristics should have a linear relationship (obey Ohm's law). In an ideal case, the charge carriers are free to flow from the metal to the semiconductor and vice versa, and the contact resistance should be low [75]. The characteristic electrical property of ohmic contacts is called specific contact resistance $R_c$ evaluated at zero volts applied bias and can be defined as

$$R_c = (\frac{(\partial J)}{\partial V})^{-1}_{V=0}, \tag{2.12}$$

where $J$ is the current density of M-S contact.

In order to fabricate an ohmic contact on an n-type semiconductor, the metal work function should be lower than that of the semiconductor work function $\Phi_m < \Phi_s$, as shown in Figure 2.7 on the right. Figure 2.7 (c) shows that when $\Phi_m < \Phi_s$, the electrons transfer from metal to the semiconductor and accumulate in the space charge region. This region is called the accumulation layer. As a result, the Fermi-level of the metal and semiconductor will be aligned and the energy bands of the semiconductor are bent downwards near the interface. This reduces the barrier or results in potential barrier between the metal and semiconductor. Thus, the electrons can flow freely across the contact [61]. The low resistance metal-semiconductor contact will be obtained if the barrier height is small, as shown in the following equation [12]

$$R_c = \frac{(k)}{qA^*T} \exp(\frac{q\phi_b}{kT}). \tag{2.13}$$

Practically, ohmic contact formation is affected by external factors such as surface states, conditions under which the contacts are fabricated, interface states, and reactions between the metal and semiconductor [58]. The most practical ohmic contact is called a tunnel contact, when the semiconductor layer adjacent to the metal is heavily doped (the doping density required

is $10^{19}$ cm$^{-3}$ or higher), the depletion region within the semiconductor becomes thin enough for the carriers to tunnel through. Thus the contact behaves ohmic and is called a tunnel contact [75]. So the specific contact resistance $R_c$ for high doping levels is given by [12]

$$R_c = \exp[\frac{4\sqrt{m_n \varepsilon_s}\phi_b}{\sqrt{N_D}\hbar}], \tag{2.14}$$

where $m_n$ is the electron effective mass, $\varepsilon_s$ is the dielectric permittivity of the semiconductor, $N_D$ is the donor concentration and $\hbar$ is the reduced Planck constant.

Equation 2.14 shows that in the tunneling range, the specific contact resistance $R_c$ depends strongly on doping concentration and varies exponentially with the factor $\frac{\phi_b}{\sqrt{N_D}}$.

## 2.8 Current transport mechanisms

Current transport through the metal-semiconductor contacts via charge carrier transport by various mechanisms under forward bias are shown schematically for an n-type semiconductor in Figure 2.10. These mechanisms are:

1. Thermionic emission (TE) of carriers over the top of the barrier from the semiconductor into the metal.
2. Quantum-mechanical tunneling through the barrier, carriers tunnels through across the full barrier width (the preferred mode for ohmic contacts).
3. Carrier generation and recombination in the space-charge region.
4. Hole injection from the metal to the semiconductor (recombination in the neutral region).

### 2.8.1 Thermionic emission

Current flow through the metal-semiconductor contact takes place in different ways depending on the doping levels, ambient temperatures, and barrier height. For moderately doped semiconductors, $N_D \leq 10^{17}$ cm$^{-3}$, the width of the depletion region is relatively large. Thus, in an ideal case (assuming no defects exist), it is difficult for electrons to tunnel through the barrier. The thermionic-emission theory makes the assumption that the barrier height is much greater than $kT$ (the current density is calculated only for electrons with sufficient energy to overcome the potential barrier), thermal equilibrium is established at the plane that determines emission, and the presence of a net current flow does not affect this thermal equilibrium [76]. According to the thermionic-emission theory, the current density is given by [58]

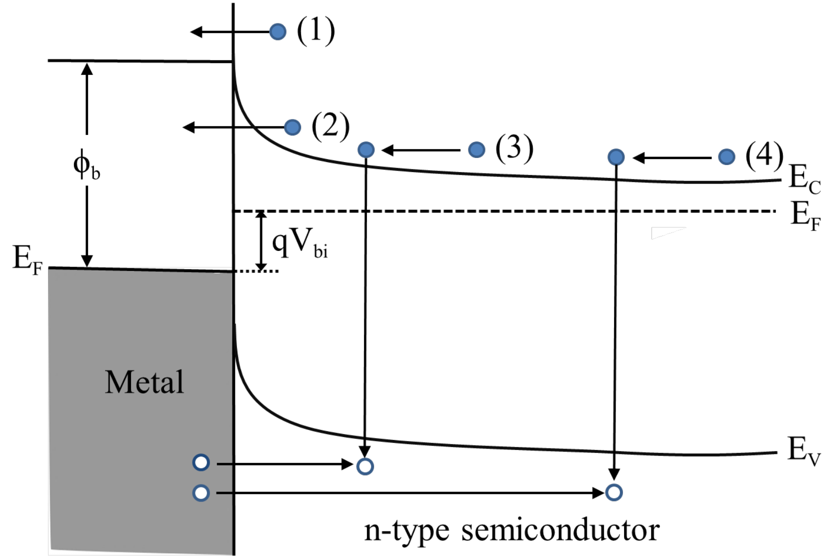


Figure 2.10: The basic transport processes in forward biased Schottky barrier on an n-type semiconductor. These are (1) thermionic emission, (2) Quantum-mechanical tunneling, (3) carrier generation and recombination and (4) hole injection. Redrawn from ref [77].

$$J_n = A^* T^2 \exp(-\frac{q\phi_b}{kT})[\exp(\frac{qV}{kT}) - 1], \tag{2.15}$$

where $A^*$ is the effective Richardson constant, $T$ is the absolute temperature, $k$ is the Boltzmann constant, $\phi_b$ is the barrier height and $V$ is the bias voltage.
Equation 2.15 also can be written as

$$J_n = J_s[\exp(\frac{qV}{kT}) - 1], \tag{2.16}$$

where $J_s$ is the saturation current density and given as

$$J_s = [A^* T^2 \exp(-\frac{q\phi_b}{kT})]. \tag{2.17}$$

Equation 2.16 gives the current density of an ideal case. For the non-ideal case, in which series resistance $R_S$ and ideality factor $n$ will be included, the expression is given as

$$J_n = J_s \exp(\frac{qV - IR_S}{nkT})[1 - \exp(\frac{qV - IR_S}{kT})]. \tag{2.18}$$

The ideality factor $n$ is calculated from the gradient of the linear region of the semi-logarithmic $I$-$V$ plot and is given as

$$n = \exp(\frac{q}{kT})\exp(\frac{dV}{d(lnI)}). \tag{2.19}$$

The series resistance $R_S$ is obtained from the deviation of the semi-logarithmic *I-V* plot from linearity at high current and is given as [55]

$$R_s = \frac{\Delta V}{I}. \tag{2.20}$$

### 2.8.2 Quantum-mechanical tunneling

Under certain conditions such as heavily doped semiconductors and low operating temperatures, the electrons with energies lower than the top of the barrier can tunnel through the barrier by quantum-mechanical tunneling (tunneling becomes the dominant process). This may modify the thermionic process into the field emission and thermionic field emission. The occurrence of the current in the forward bias due to tunneling of electrons with energies close to the Fermi energy in semiconductors is known as "field" emission. When the temperature is raised, electrons are excited to higher energies where the barrier is very thin and tunneling can occur. This is known as "thermionic field" emission [76].

### 2.8.3 Generation-recombination current

The generation-recombination of the carriers occurs in the space charge region. The recombination in the depletion region occurs via localized (defect) states. According to the theory (Schottky and Read, Hall), the most effective centers are those with energies lying near the band gap center. The current theory describing such a recombination centre is the same for both Schottky diodes and p-n junctions. The current density under low forward bias is given as [58]

$$J_r = J_{r0} \exp(\frac{qV}{2kT})[1 - \exp(-\frac{qV}{kT})], \tag{2.21}$$

where $J_{r0} = qn_i w/2\tau_r$, $n_i$ is the intrinsic electron concentration proportional to $exp(-E_g/2kT)$, $w$ is the depletion width and $\tau_r$ is the lifetime of carriers within the depletion region. This equation is derived by assuming, firstly, that the energy levels of the centers coincide with intrinsic Fermi-level, secondly, that the capture cross sections for holes and electrons are the same and thirdly, that the centers are distributed uniformly through the depletion region [58]. Recombination phenomena can be classified into two processes, direct and indirect processes:

1. Direct recombination process occurs when an electron jumps from the conduction band and recombines with a hole in the valence band. In this process, the law of conservation of momentum is obeyed. This process is also called band-to-band recombination. In the direct recombination, a quantum of energy is released in the form of a photon, and when

a photon is emitted this is called radiative recombination. Direct recombination usually dominates in direct band gap semiconductors such as gallium arsenide and ZnO.

2. Indirect recombination process takes place when an electron falls into a trap level in the band gap and can recombine with a hole later. Also, in indirect recombination, the free electron can recombine with a free hole through recombination centers located into the band gap. Recombination centers are permitted energy levels introduced by contaminants, impurity atoms or crystal defects. These energy levels act as catalysts. The indirect recombination process via band gap recombination centers dominates in indirect band gap semiconductors, such as silicon and germanium.

### 2.8.4 Hole injection

When the height of the Schottky barrier diode on the n-type semiconductor material is greater than half of the band gap of the semiconductor, the region near to the metal contains a high density of holes, and becomes p-type. When the forward bias is applied, some of these holes diffuse into the neutral region of the semiconductor. Thus giving rise to the injection of holes [58].

## 2.9 Defects in semiconductor materials

Defects in semiconductor materials may be foreign atoms (impurities) or crystalline defects. The crystalline defects are classified according to their geometry and shape into four types [78, 79]:

1. Point defects (zero-dimensional defects), these defects affect isolated lattice sides. In this section, the discussion will be a focus on point defects.

2. Linear defects (one-dimensional defects) are also known as dislocations. These defects can be formed during material solidification, vacancy condensation and plastic deformation. Dislocations are classified into two types; edge dislocations and screw dislocations.

3. Interfacial defects (two-dimensional defects) also are called planar defects. These defects include external surfaces, grain boundaries and stacking faults.

4. Bulk or volume defects (three-dimensional defects). These defects include pores, cracks and foreign inclusions in crystalline materials.

Impurities can be introduced either deliberately or unintentionally during crystal growth and device processing. It can be intentionally incorporated as dopant atoms (shallow level impurities), or as recombination centers (deep level impurities) [55]. The defects may induce electronic energy states in the band gap of semiconductor materials. These electronic states can be divided into two types, namely shallow levels and deep levels, depending on their location with respect to the conduction or valence band edge. The shallow level defects have state levels located near the valence band for acceptors or near the conduction band for donors, their states levels are approximately 0.1 eV from the band edge [80]. Shallow levels created by dopants in semiconductor materials are ionized at room temperature and provide free carriers to form p-type or n-type semiconductors. Deep-level defects have levels located deeper in the band gap. Deep-level defects can act as traps, recombination centers, or generation centers, depending on electron and hole capture cross section.

### 2.9.1 Point defects

Point defects cause the perturbation of the lattice to remain localized. Many different point defects in semiconductor materials are possible and some of these are shown in Figure 2.11. Point defects are classified into two types intrinsic and extrinsic defects. Intrinsic or native point defects are defects in the crystal lattice that involve only the constituent materials. These defects include vacancies (missing atoms at the regular lattice points that form during solidification as a result of local disturbances), interstitials (extra or small atoms occupying interstitial site between occupied lattice sites in a crystal) and antisite (host atoms occupying the wrong lattice sites). The most common native point defects in ZnO include the oxygen vacancy $V_o$, zinc vacancy $V_{Zn}$, oxygen antisites $O_{Zn}$, zinc antisites $Zn_o$, oxygen interstitials $O_i$ and zinc interstitials $Zn_i$ [81]. Native defects can strongly affect on electrical, optical and magnetic properties of a semiconductor. These defects influence the minority carrier lifetime, luminescence efficiency, diffusion mechanisms and device degradation. Understanding the nature, origins and behavior of point defects in ZnO is essential to its successful application in semiconductor devices. Oxygen vacancies $V_o$ and zinc interstitials $Zn_i$ have often been invoked as sources of n-type conductivity in ZnO.

The small aggregates of several point defects such as divacancies and vacancy-donor complexes also cause only a local perturbation of the lattice. They are generally considered as point defects as well [62]. Extrinsic point defects occur due to impurity atoms or dopant ions occupying substitutional or interstitial sites. Extrinsic point defects in ZnO include hydrogen and other impurities introduced during growth, e.g., group III related elements [82].

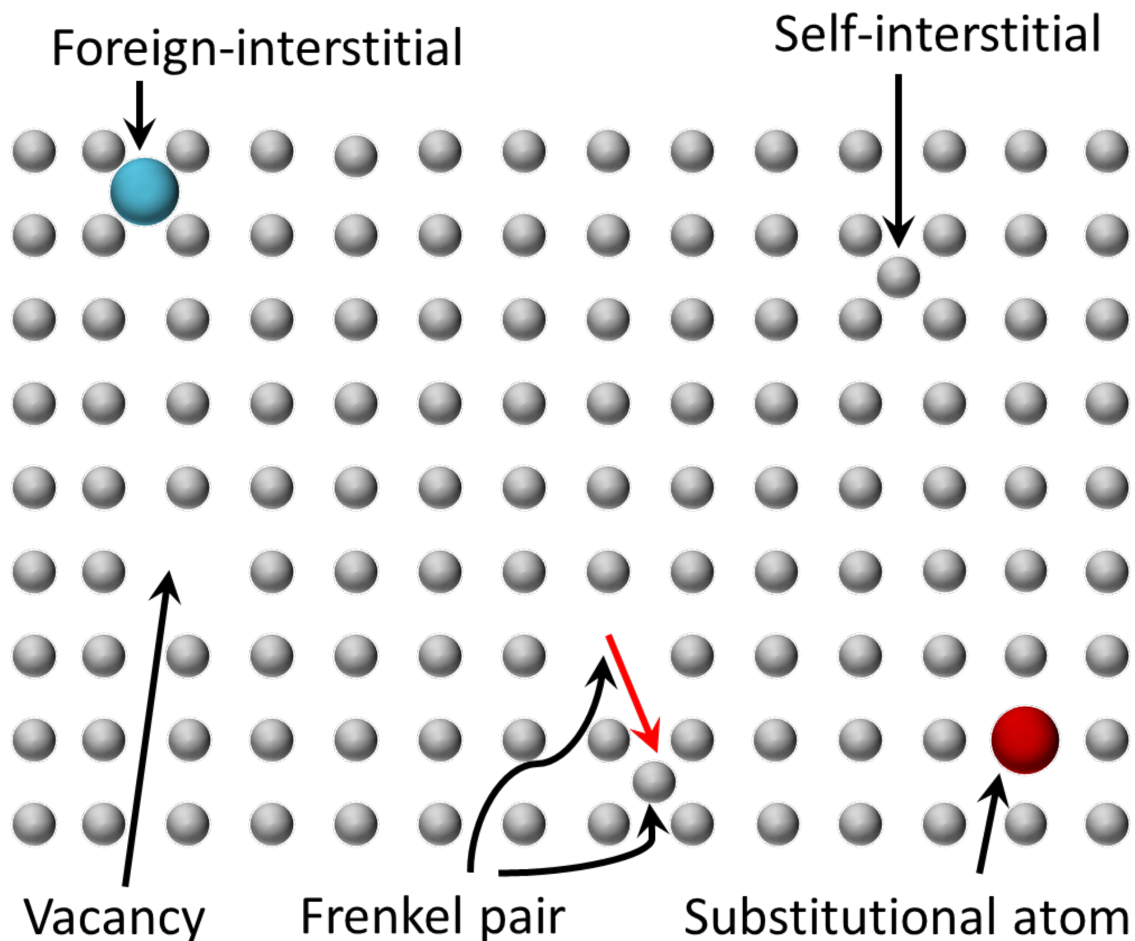


Figure 2.11: A schematic diagram of point defects. Redrawn from ref [83].

### 2.9.2 Defect characterization

Defects in semiconductors play a critical role in determining the viability of a given material for device applications. The electrical properties of semiconductor materials and the performance and reliability of devices based on semiconductor materials can be significantly influenced by the density of undesirable defects. Therefore, it is essential to control and characterize the electrical properties of defects in a semiconductor using a reliable and accurate technique. Since device operation depends mainly on the electrical properties, electrical characterization is, therefore, more relevant. Also, the activation of defects due to electrical processes requires scrutiny as it directly impacts the performance and reliability of a device. The deep level transient spectroscopy (DLTS) is an appropriate technique for characterizing electrically active defects in semiconductor materials [84].

### 2.9.3 Emission and capture of carriers from deep levels

The band diagram of an ideal single crystal semiconductor consists of a valence band and a conduction band separated by the band gap, with no energy levels within the band gap. When defects are introduced in the single crystal, the defect energy levels are generated in the band gap represent by $E_T$ in Figure 2.12. These defects are described as generation-recombination centers or traps (electron taps and hole traps). Generation-recombination centers are located deep in the band gap of semiconductor and are called deep energy level defects. They act as recombination centers when there are excess carriers in the semiconductor and as generation centers when the carrier density is below equilibrium [55].

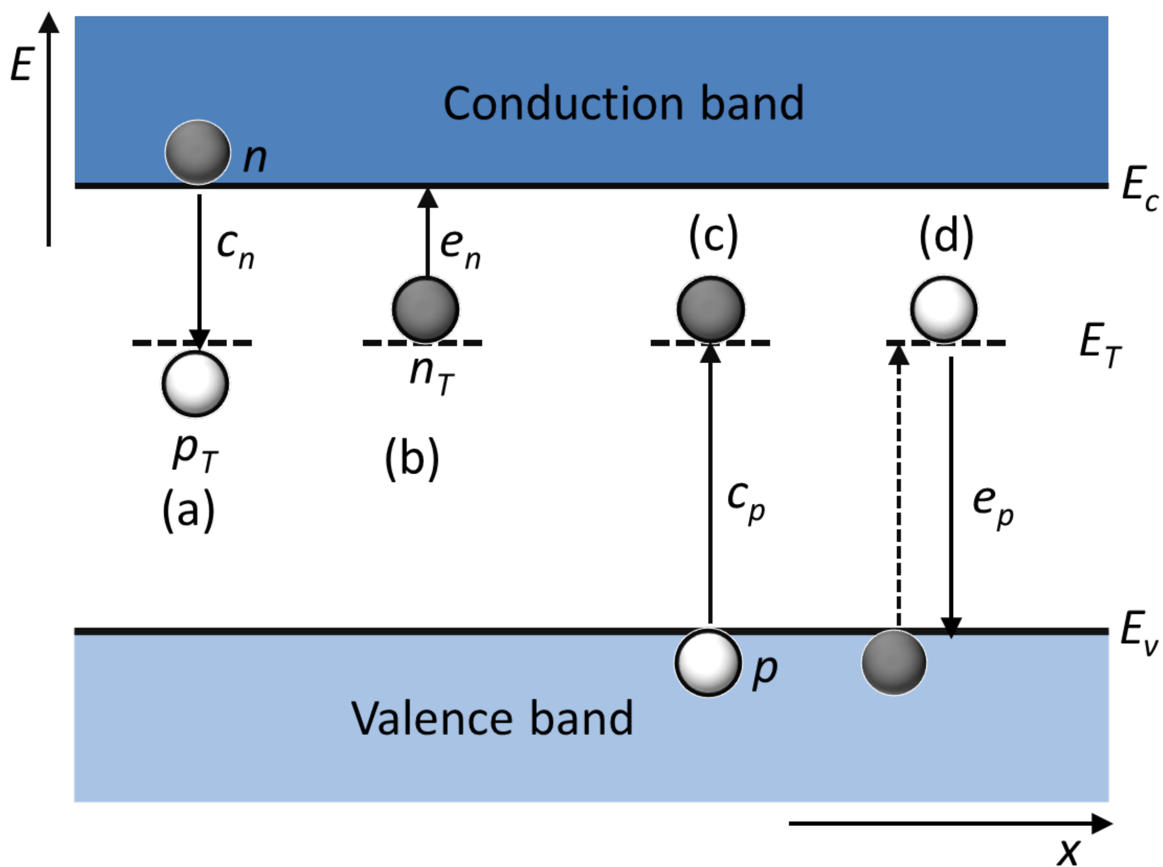


Figure 2.12: Electron energy band diagram for a semiconductor with deep-level impurities. Redrawn from ref [55].

Figure 2.12 shows the following process of the capture and emission. The center captures an electron from the conduction band (Figure 2.12 (a)), characterized by the capture coefficient $c_n$. After that, one of two events occurs. The center can either emit the electron back to the conduction band, called electron emission $e_n$ (Figure 2.12 (b)), or it can capture a hole from the valence band, shown in Figure 2.12 (c) as $c_p$. After either of these events, the generation-

recombination center is occupied by a hole and again has two choices. Either it emits the hole back to the valence band $e_p$ in Figure 2.12 (d) or captures an electron (Figure 2.12 (a)). These are the only four possible events between the conduction band, the impurity energy level, and the valence band. Process (d) is sometimes viewed as electron emission from the valence band to the impurity level shown by the dashed arrow. However, we will use the hole emission process in (d) because it lends itself more readily to mathematical analysis. A recombination event in Figure 2.12 (a) is followed by (c) and a generation event (b) is followed by (d). The impurity trap is a generation-recombination center and both the conduction and valence bands participate in recombination and generation [55]. The probability that the deep electron trap captures an electron is given by [85]

$$C_n = n \langle v_n \rangle \sigma_n, \tag{2.22}$$

where $n$ is the electron concentration in the conduction band, $\sigma_n$ is the electron capture cross section and $\langle v_n \rangle$ is the mean thermal velocity of free electrons given as

$$\langle v_n \rangle = \sqrt{\frac{3kT}{m_e^*}}, \tag{2.23}$$

where $k$ is the Boltzmann constant, $T$ is the temperature in Kelvin and $m_e^*$ is the electron's effective mass.
As a function of temperature, the electron emission rate is given by

$$e_n(T) = \sigma_n \langle v_n \rangle \frac{g_0}{g_1} N_c exp(-\frac{E_c - E_t}{kT}), \tag{2.24}$$

where $E_c - E_t$ is the energy separation of the deep state from the conduction band, $g_0$ and $g_1$ are the degeneracy terms referring to the state before and after electron emission, respectively and $N_c$ is the effective density of states in the conduction band given as

$$N_c = 2M_c(\frac{2\pi m_e^* kT}{h^2})^{3/2}, \tag{2.25}$$

$M_c$ is the number of conduction band minima and $h$ is Planck's constant.

From Equation 2.25, the obtained $N_c$ and $\langle v_n \rangle$ have a $T^2$ dependence. If $e_n$ is measured as a function of temperature, an Arrhenius plot of $log(e_n/T^2)$ against $1/T$ must give a straight line whose slope will give the energy difference $E_c - E_t$ while the intercept at (1/T = 0) gives the apparent capture cross-section $\sigma_{na}$.

If we allow the capture cross-section to vary with temperature, it will take the form

$$\sigma(T) = \sigma_\infty exp(-\frac{\Delta E_\sigma}{kT}), \tag{2.26}$$

where $\sigma_\infty$ is the capture cross-section at $T = \infty$ and $\Delta E_\sigma$ is the thermal activation energy of the capture cross-section (called the thermal barrier for carrier capture). The possible causes of the temperature dependence of the capture cross-section are the multiphonon capture into deep levels. The temperature dependence of the capture cross-section can be determined from the plot of $log\sigma(T)$ versus $(1/T)$ where $\Delta E_\sigma$ can be obtained from the slope and $\sigma_\infty$ can be obtained after extrapolation to $T = \infty$. The activation energy $\Delta E_a$ of a deep level defect whose capture cross-section is temperature dependent is given as

$$\Delta E_a = (E_c - E_t) + \Delta E_\sigma. \tag{2.27}$$

Thus for a trap whose capture cross-section is temperature dependent, the thermal emission rate is given by

$$e_n(T) = \sigma_n \langle v_n \rangle \frac{g_0}{g_1} N_c exp(-\frac{E_c - E_t + \Delta E_\sigma}{kT}). \tag{2.28}$$

The commonly used parameter for characterizing deep levels is the activation energy for thermal emission. The parameter $E_T = E_c - E_t$ is the Gibbs free energy, which is defined as the energy required to excite an electron from the trap level to the conduction band and is given as

$$E_T = \Delta H + T\Delta S, \tag{2.29}$$

where $\Delta H$ and $\Delta S$ are the changes in enthalpy and entropy due to the change in charge state of the level. Substituting Equation (2.29) into (2.28) yields

$$e_n(T) = \sigma_n \langle v_n \rangle \frac{g_0}{g_1} N_c exp(\frac{\Delta S}{k}) exp(-\frac{\Delta H}{kT}). \tag{2.30}$$

This implies that, the slope of the Arrhenius plot gives the enthalpy of the deep level and not the free energy, which can only be determined from optical measurements. Hence, one must be careful when comparing energies derived from thermal emission measurements with other methods.

## 2.10 Deep-level transient spectroscopy (DLTS)

Deep level transient spectroscopy (DLTS) was introduced by Lang 1974. This technique is based on the transient capacitance change associated with the thermal emission of charge carriers from a trap level to thermal equilibrium after an initial non-equilibrium condition

in the space-charge region [84, 86]. DLTS measures the capacitance of a reverse biased p-n junction, Schottky barrier diode or MOS device due to the emission of carriers by defects in the depletion region. DLTS is one of the most sensitive techniques, as it has the ability to detecting defects at such low concentrations and measures their electronic properties [85, 87]. Many defect parameters can be obtained from DLTS such as the thermal activation energy $E_T$, electron and hole capture cross-sections $\sigma_n$ and $\sigma_p$, respectively, and defect concentration $N_T$. The sign of each peak indicates whether it is due to a majority or minority carrier trap and positions of the peaks are simply and uniquely determined by the instrument rate-window and the thermal emission properties of the respective trap.

The relationship between the width of the depletion region for a Schottky barrier diode or p-n junction and the applied voltage is given as [85]

$$w = \sqrt{\frac{2\varepsilon(V_{bi}+V)}{qN}}, \tag{2.31}$$

where $\varepsilon$ is the dielectric constant of the depleted semiconductor, $V_{bi}$ is the built-in potential of the junction, $V$ is the externally applied voltage, $q$ is the charge of an electron, and $N$ is the density of the ionized impurities due to dopants and other defects with levels in the band gap. The junction capacitance due to the depletion layer is given as

$$C = \frac{\varepsilon A}{w} = A\sqrt{\frac{q\varepsilon N}{2(V_{bi}+V)}}, \tag{2.32}$$

where $A$ is the cross sectional area of the junction. From Equations 2.31 and 2.32, if the concentration of electrons or holes trapped at deep levels is changed (e.g., by the thermally or optically stimulated emission of carriers to the conduction or valance bands), this change can be monitored by measuring the variation in the junction capacitance. The variation in junction capacitance at a constant applied voltage as a result of the temperature-dependent variation of $N$ forms the basis of capacitance-based DLTS.

The variation of the depletion region width and trap occupancy after applied reverse bias and a filling pulse sequence for an electron trap in an n-type semiconductor is shown in Figure 2.13. Part (A), applied reverse bias, leads to an increase in the width of the depletion region $w$. This alters the occupancy of traps in the space charge region. In part (B), the filling pulse is applied and reverse bias is reduced, decreasing the width of the depletion region. This results in majority carriers becoming available for capture by the empty deep level traps. In part (C), the filling pulse is removed immediately and the original reverse bias is restored. Since the trapped electrons do not respond immediately, the space charge density is reduced. This instantaneously

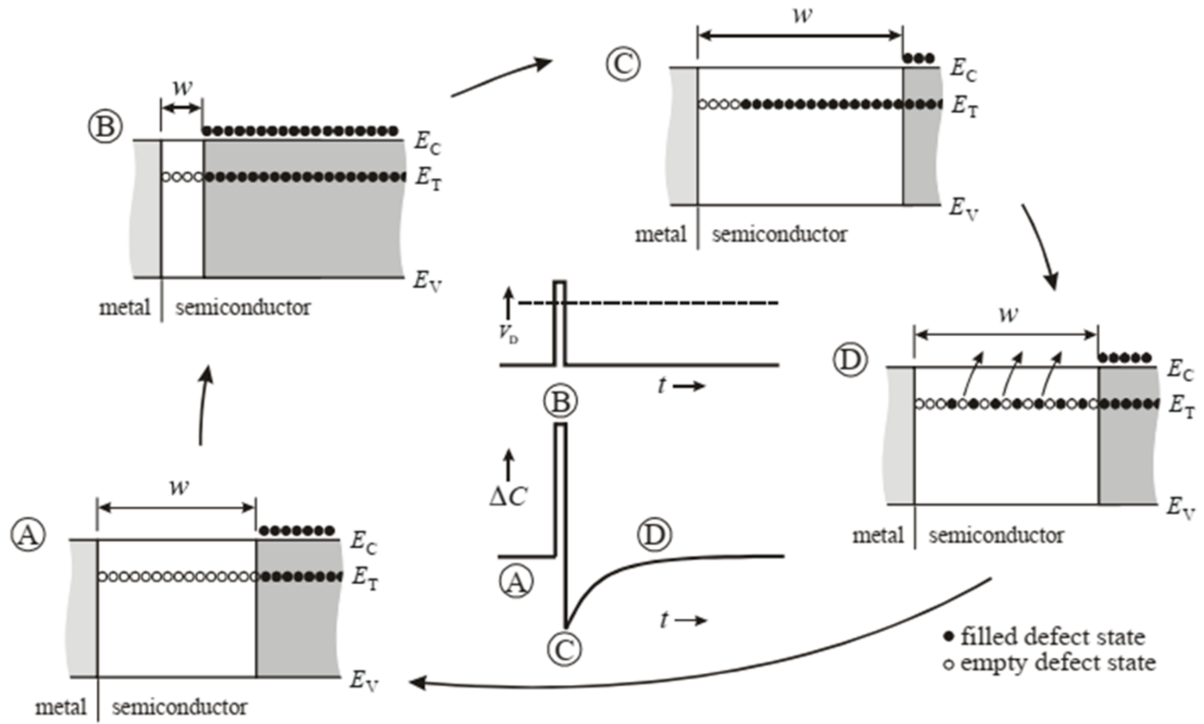


Figure 2.13: Variation of depletion region width and trap population of an electron trap in n-type semiconductor for a DLTS bias and filling pulse cycle. (A) and (B) are during reverse bias and the filling pulse, respectively, whereas (C) is directly after removing the filling pulse and (D) at a time $t$ after (C). The resultant capacitance transient is qualitatively shown in the center of the figure [85].

leads to a wider depletion region and a decreased capacitance to below the original value. From part (C) and (D), the capacitance relaxes by the thermal emission of the trapped carriers, giving an increase to a capacitance transient [85, 88]. The emission rate can be determined from the time dependence of the capacitance transient. The density of occupied defect levels at time $t$ after removing the filling pulse is given as [85]

$$N(t) = N_T exp(-e_n t), \tag{2.33}$$

where $e_n$ is the thermal emission rate and $N_T$ is the trap concentration assuming all the traps were initially filled. For $N_T >> N_D$, the junction capacitance can be expressed as a time-dependent function given by

$$C(t) = C_0 - \Delta C_0 exp(-e_n t), \tag{2.34}$$

where $C_0$ is the equilibrium reverse bias voltage capacitance and $\Delta C_0$ is a change in capacitance observed immediately after removing the pulse.

In order to determined the defect concentration, we assume that if the peak height is directly

proportional to the defect concentration $N_T$, then concentration can be obtained from [89]

$$N_T(w_m - \lambda) = \frac{2\Delta C(0)}{C} N_D \times [(\frac{w-\lambda}{w})^2 - (\frac{w_p - \lambda}{w})^2]^{-1}. \quad (2.35)$$

where $C$ is the junction capacitance, $\Delta C(0)$ is the capacitance change due to pulse at t = 0 just after pulsing, $N_D$ is the concentration of shallow impurities. w and $w_p$ are the depletion widths during application of the reverse and filling pulse, respectively, and $w_m - \lambda$ is the mean distance from the interface to the region from which traps emit carriers, and $\lambda$ is the width of the transition region and given by [85]

$$\lambda = \sqrt{\frac{2\varepsilon(E_F - E_T)}{q^2 N_D}}, \quad (2.36)$$

where $\varepsilon$ is the dielectric constant of the semiconductor, $E_F$ is the Fermi level, $E_T$ is the trap level and $q$ is the electronic charge.

### 2.10.1 Rate window scan

The basic technique used to analyze the DLTS transient was the dual-gated (double boxcar) technique [86]. According to this technique, the DLTS signal is obtained by subtracting the capacitances measured at preset times $t_1$ and $t_2$. The emission rate depends on temperature. At low temperatures, the emission rate is low. At high temperatures, the emission rate will be much faster, so that the time constant varies with temperature [86]. When the signal (or difference in capacitance $C(t_1) - C(t_2)$) is plotted as a function of temperature, the peak is observed (see Figure 2.14 on the bottom) which is characteristic of the defect. As shown in Figure 2.14, the difference in capacitance changes as a function of temperature. It increases until $C(t_1) - C(t_2)$ reaches a maximum and then it starts decrease. The value of the time constant, $\tau$, at the maximum of the difference in capacitance ($C(t_1) - C(t_2)$) against temperature $T$ for the defect can be related to the gate positions $t_1$ and $t_2$. This is obtained by normalizing the DLTS signal *S(T)* shown in Figure 2.14 (bottom) which is defined as [86]

$$S(T) = [C(t_1) - C(t_2)]/\Delta C(0), \quad (2.37)$$

where $\Delta C(0)$ is the capacitance due to the pulse change at $t = 0$. For exponential transients,

$$S(T) = [exp(-t_1/\tau)] - [exp(-t_2/\tau)], \quad (2.38)$$

which can also be written as

$$S(T) = exp(-t_1/\tau)[1 - exp(-\Delta t/\tau)], \quad (2.39)$$

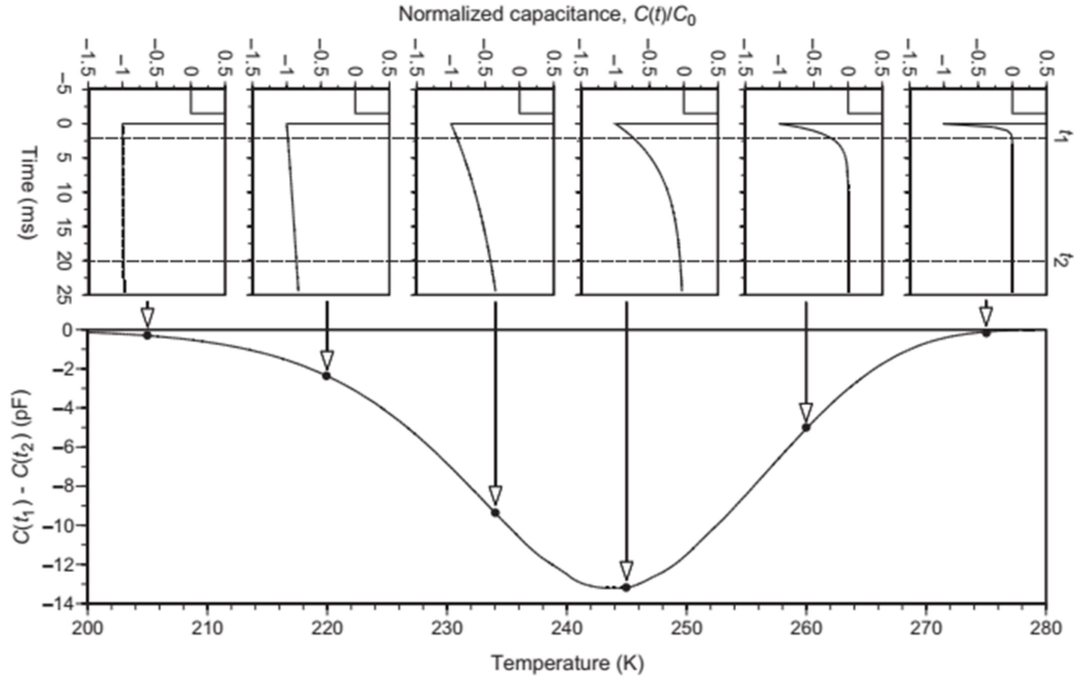


Figure 2.14: Temperature dependence of time constant of capacitance transient (top), and the DLTS signal obtained from the transient as a function of sample temperature (bottom) [84].

where $\Delta t = t_2 - t_1$. Thus, the relationship between $\tau_{max}$, $t_1$ and $t_2$ can be obtained by differentiating S(T) with respect to $\tau$ and equating the result to zero:

$$\tau_{max} = \frac{t_1 - t_2}{ln(\frac{t_1}{t_2})}. \tag{2.40}$$

When the thermal scanning is repeated for different rate windows the results can be used to obtain an Arrhenius plot ($ln(e_n/T^2)$ versus (*1/T*), where $e_n$ is the thermal emission rate), which is shown in Figure 2.15. The defect parameters such as activation energy can be obtained from the slope and the capture cross section from the y-intercept of this plot.

### 2.10.2 Laplace-transform deep-level transient spectroscopy (L-DLTS)

The standard DLTS which uses boxcar or lock-in techniques, exhibits excellent sensitivity. However, the time constant resolution is poor resulting in conventional DLTS not being able to separate closely spaced transients or different traps with similar emission rates. There are many efforts applied to improve DLTS resolution by developing different weighting functions. These higher-order filters showed an improvement of resolution by up to a factor 3 but at the expense of noise performance. Dobaczewski *et al.* [90] in 1994 developed an improved high-resolution version of DLTS, called Laplace DLTS. Laplace-DLTS has high sensitivity and a

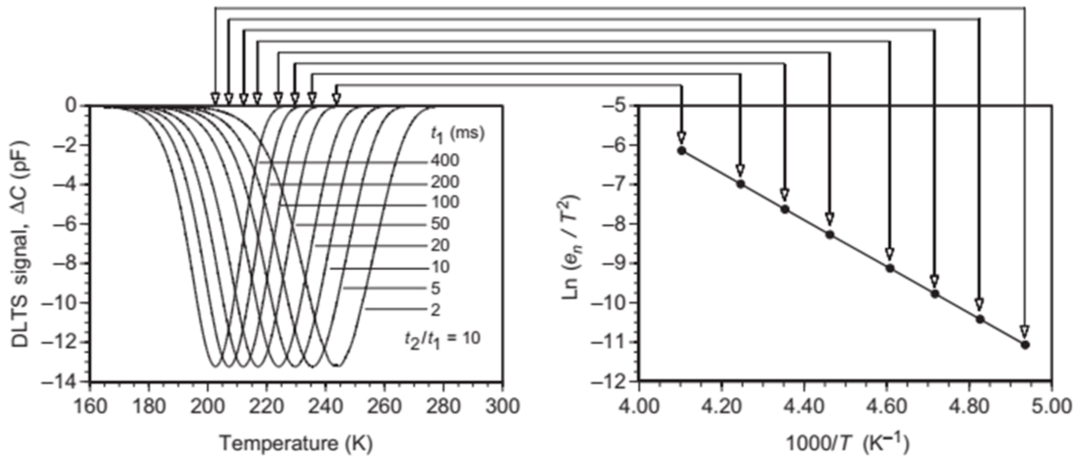


Figure 2.15: Deriving an Arrhenius plot from DLTS signals. The DLTS signals are measured at different values of $t_1$ with $t_2/t_1 = 10$ [84].

sufficiently high energy resolution to reveal information on the impurity's local environment. This technique is based on the assumption that a spectrum of emission rate characterizes the capacitance transient. It makes use of Tikhonov's regularization to separate the constituent exponentials by imposing a constraint on the second derivative. Then, using Laplace transforms [90]

$$f(t) = \int_0^\infty F(s) e^{-st} dt, \tag{2.41}$$

where *f(t)* is the recorded transient and *F(s)* is the spectral density function. *F(s)* is a delta function. Therefore, a plot of spectral density function *F(s)* versus emission rate produces a spectral function which can be used as a defect signature. The area under each peak is directly related to the trap concentration and is a function of the emission rate. Up to 32000 transients can be captured at a fixed temperature and averaged. Fixing the temperature improves the time constant resolution. A good signal to noise ratio provides an order of magnitude better resolution than conventional DLTS.

# Chapter 3

# Experimental and characterization techniques

## 3.1 Introduction

The experimental section describes the processing and characterization techniques used in this study. This includes ZnO solution preparation, cleaning processes of substrates, deposition of ZnO thin films, Schottky and ohmic contacts fabrication, as well as characterization techniques such as scanning electron microscopy (SEM), X-ray diffraction (XRD), Raman spectroscopy, UV-Vis spectroscopy and photoluminescence spectroscopy (PL). The electrical and defect characterization using current-voltage ($I$-$V$), capacitance-voltage ($C$-$V$), deep level transient spectroscopy (DLTS) and Laplace-deep level transient spectroscopy (LDLTS) are also described.

## 3.2 Samples preparation

This section describes sample preparation steps, including undoped and doped ZnO solution, cleaning of the substrates and thin films deposition, which were used in the different studies.

### 3.2.1 Substrate cleaning procedures

Before deposition, ITO/glass (with dimension of 20 mm $\times$ 10 mm $\times$ 2mm and sheet resistance of 12 $\Omega$/sq) and microscope slides were cleaned in a three-step procedure, using acetone, ethanol and deionized water in an ultrasonic bath and dried in flowing $N_2$.

The n-Si substrate (13 - 17 $\mu$m thick with a resistivity of 1.4 - 1.8 $\Omega$cm) was cleaned using

trichloroethylene followed by isopropanol, then methanol and rinsed in deionized water. Each step was carried out for 5 min in an ultrasonic bath. Thereafter, the n-Si substrate was etched using hydrofluoric acid to remove the native oxide and dried in flowing $N_2$.

### 3.2.2 Sol-gel spin coating technique

Spin coating is a simple procedure for fast depositing thin films on flat substrates. A small amount of the coating solution is dropped on the center of the substrate. The substrate is then rotated at high speed in order to spread the coating solution and leave behind a very uniform coating of the chosen material on the surface of the substrate.

The sol-gel spin coating deposition technique is preferred in the preparation of high-quality ZnO thin films due to the low cost equipment required, the resulting homogeneous and relatively smooth thin films, the simplicity and ability to deposit large area films, and easily controlled film thickness by controlling the number of spin coating layers and pre-annealing cycles [40, 41]. There are three types of materials used in synthesizing ZnO using the sol-gel method. These materials are precursor, solvent and stabilizer. The precursor materials consist of metal ions. A solvent such as isopropanol is used. Stabilizer such as monoethanolamine. The concentrations used are given in the results section.

### 3.2.3 Materials

The following materials were used for the preparation of the ZnO thin films were purchased and used as received without any further purification. Zinc acetate dihydrate (ACE, 98%), isopropanol (ACE, 99.5%), monoethanolamine (MEA) (ACE, 99.5%), erbium(III) nitrate pentahydrate ($Er(NO_3)_3.5H_2O$) (Sigma Aldrich, 99.9%) and ytterbium(III) nitrate pentahydrate ($Yb(NO_3)_3.5H_2O$) (Sigma Aldrich, 99.9%).

### 3.2.4 Undoped ZnO thin films

Undoped ZnO solution prepared using the sol-gel method. Zinc acetate dihydrate was dissolved in isopropanol, and the solution was continuously stirred at 60 °C until everything was dissolved. Monoethanolamine (MEA) was then added to the solution, maintaining a molar ratio of MEA to zinc acetate dihydrate of 1.0 and the concentration of zinc acetate was kept at 0.5 M. The solution was continuously stirred for 2 hours at 60 °C to obtain a homogeneous, clear solution. The solutions were aged for 48 hours.

To form ZnO thin films, the ZnO sol was spin-coated onto the ITO/glass and n-Si substrates. The substrates were rotated at 4 000 rpm. The sol was dropped onto the substrates and spun for 40 s. The film was then dried at 200 °C for 5 min. The coating and drying steps were repeated several times to obtain the desired thickness. The final films were annealed at 600 °C in air for 1 h. The ITO/glass substrate was used for structure, surface and optical characterizations, whilst the n-Si substrate was used for electrical and defect characterizations. Figure 3.1 shows a schematic diagram of the synthesis of the ZnO thin films using the sol-gel spin coating method.

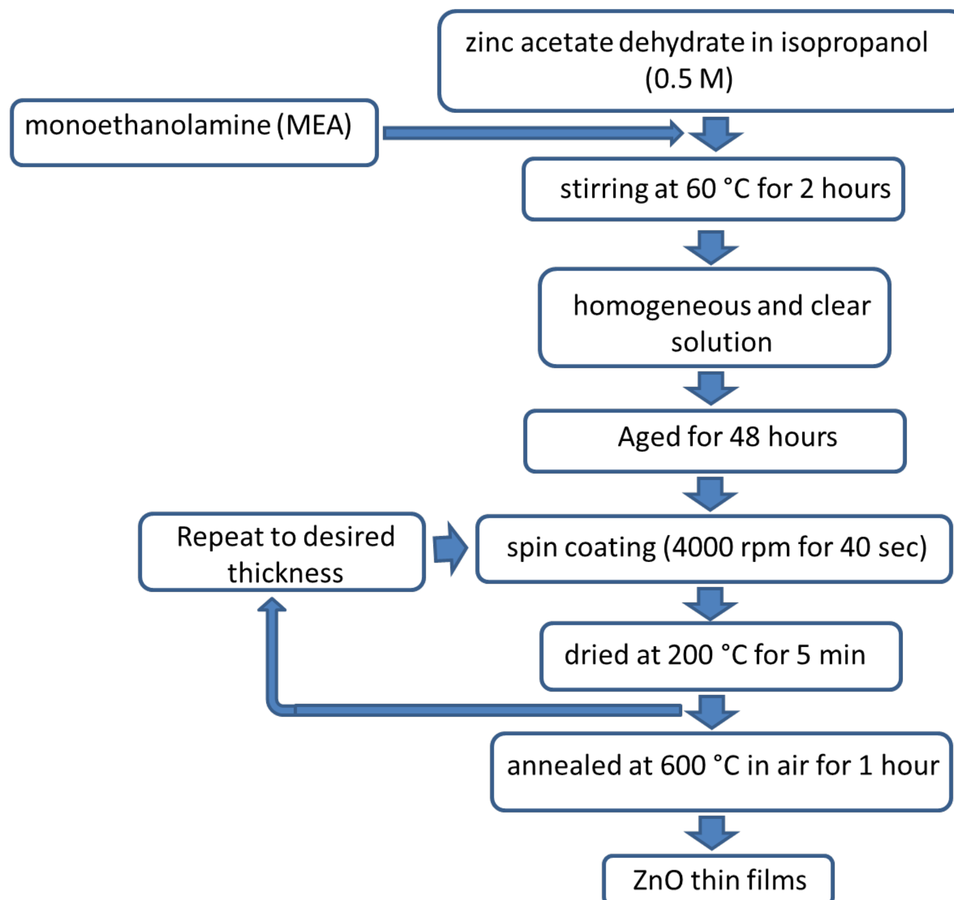


Figure 3.1: A schematic diagram of the preparation of ZnO thin films using the sol-gel spin coating method.

### 3.2.5 Er-doped and Yb-doped ZnO thin films

The 3 at.% Er-doped and 3 at.% Yb-doped ZnO solutions were prepared using the following dopant sources: erbium(III) nitrate pentahydrate ($Er(NO_3)_3.5H_2O$) and ytterbium(III) nitrate pentahydrate ($Yb(NO_3)_3.5H_2O$). As with the undoped zinc oxide thin films, the zinc acetate dihydrate and dopants precursors were dissolved in isopropanol. The solutions were stirred continuously for 2 hours at 60 °C together with monoethanolamine (MEA) to obtain a homogeneous, clear solution. The molar ratio of MEA to zinc acetate dihydrate was maintained at

1.0 and the concentration of zinc acetate was 0.5 M. The solution was kept at room temperature for 48 hours before being used.

The ZnO solution was deposited on clean microscope slides and n-Si substrates by spin coating. Before deposition, the microscope slides and n-Si (525 $\mu$m thick with a resistivity of 2 - 30 $\Omega$cm and the carrier concentrations of $\sim \times 10^{14}$ cm$^{-3}$) were cleaned as described in Section 3.2.1. The aged ZnO sol was spin-coated at 4 000 rpm for 40 sec on the substrates. The film was then dried at 200 °C in air for 5 min. The coating and drying steps were repeated several times to obtain the desired thickness. The final films were annealed at 600 °C in air for 1 hour.

### 3.2.6 Er-doped ZnO thin films at varying concentrations

Er 0, 2, 4 and 6 at.% doped ZnO solution were prepared using the method described previously in Section 3.2.4. Zinc acetate dihydrate and the appropriate amount of dopant precursor were dissolved in isopropanol. The solutions were stirred at 60 °C for 2 hours after the addition of monoethanolamine (MEA) to obtain a homogeneous, clear solution. The molar ratio of MEA to zinc acetate dihydrate was fixed to 1.0 and the concentration of zinc acetate was 0.5 M. The solution was aged at room temperature for 48 hours.

The pure and Er-doped ZnO sol-gel were deposited on microscope slides and n-Si substrates. The aged ZnO sol was spin-coated at 4 000 rpm for 40 sec on the substrates. The film was then dried at 200 °C for 5 min in air. The coating and drying steps were repeated several times to obtain the desired thickness. The final films were annealed at 500 °C in air for 1 hour compared to 600 °C in the previous experiments.

### 3.2.7 (Er, Yb) co-doped ZnO thin films at varying concentrations

ZnO co-doped with (Er, Yb) 0, 2, 4 and 6 at.% solution were prepared using the following dopant sources: erbium(III) nitrate pentahydrate ($Er(NO_3)_3.5H_2O$) and ytterbium(III) nitrate pentahydrate ($Yb(NO_3)_3.5H_2O$). Zinc acetate dihydrate and the appropriate amount of dopants precursor were dissolved in isopropanol. The solutions were stirred at 60 °C together with monoethanolamine (MEA). The same steps as in section 3.2.5 have been followed to prepare the sol-gel and thin films deposition of undoped and (Er, Yb) co-doped ZnO thin films at different concentrations. The Er and Yb in a 1 : 1 ratio to a total of 2 at.%, 4 at.% and 6 at.% doping. The final films were annealed at 500 °C in air for 1 hour.

### 3.2.8 Thin films annealing

After spin-coating each layer on the substrate, it was dried at 200 °C for 5 min in the air using EcoTherm oven. When the required number of layers had been deposited, the final thin film structure was post-annealed in a quartz tube using a Lindberg Hevi-duty furnace. Post-annealing temperatures and times for each sample are given in the results and discussion. The thermocouple was placed just below the sample holder to measure the sample's annealing temperature.

### 3.2.9 Ohmic and Schottky contact formation

Figure 3.2 shows a schematic of the resistive evaporation system that was used to fabricate ohmic and Schottky contacts. Pd Schottky contacts and Au-Sb (94% : 6%) ohmic contacts were deposited and the thickness was determined using a crystal monitor.

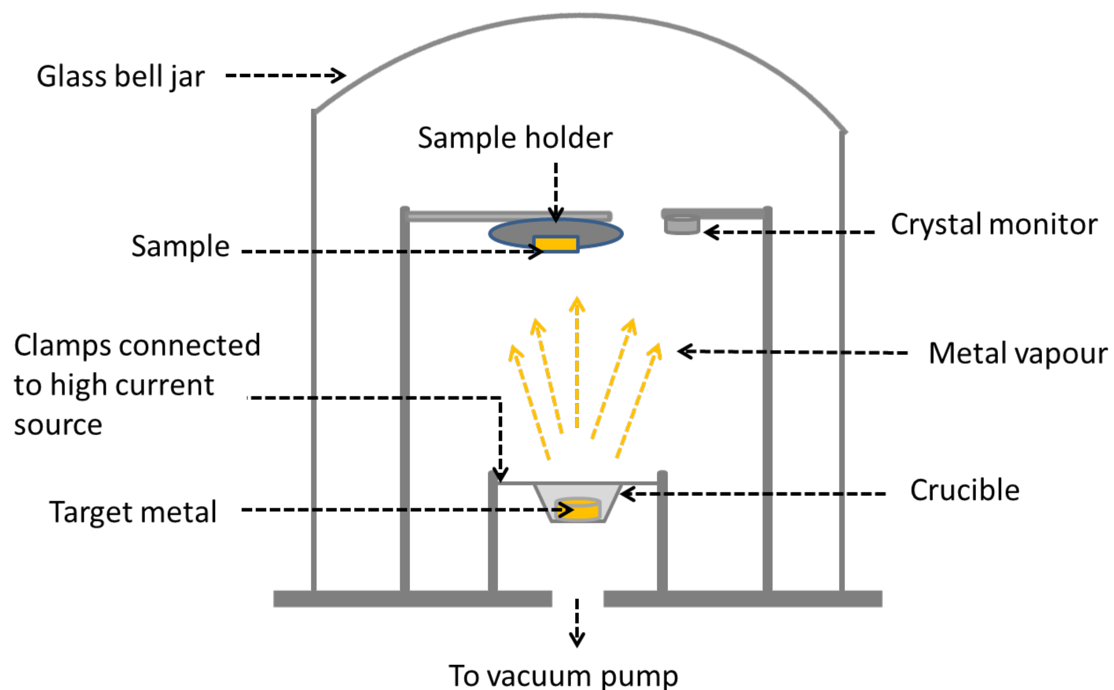


Figure 3.2: A schematic diagram of the resistive evaporation technique.

Placing the undoped and doped ZnO thin films deposited on n-Si substrates on the holder, the 150 nm thick ohmic contact (a continuous layer) was resistively deposited under an initial vacuum of $\sim 10^{-6}$ mbar at a deposition rate of 0.1 nm/s. The ohmic contacts were annealed at 350 °C in Ar to reduce the series resistance. The sample was then placed on a mask with 0.60 mm holes and attached to the holder. The 100 nm thick Pd Schottky contacts were deposited with an initial vacuum of $\sim 10^{-6}$ mbar at a rate of 0.1 nm/s. The final form of the fabricated Schottky diode is illustrated in Figure 3.3.

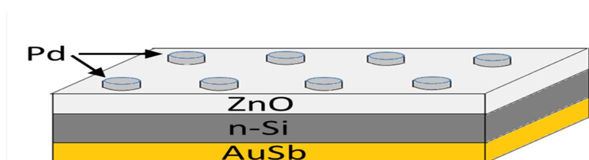


Figure 3.3: Schematic representation of the devices used for electrical measurements consisting of the Au-Sb ohmic contact, Si substrate, the ZnO thin film, and the Pd Schottky contacts.

### 3.2.10 ZnO thin film Schottky diode irradiation

Undoped ZnO thin films were irradiated at room temperature with 5.4 MeV alpha particles from an Am- 241 radionuclide for 21 hours at a flux of $7.1 \times 10^{6}$ cm$^{-2}$s$^{-1}$, with the total fluence of $5.4 \times 10^{11}$ cm$^{-2}$ through the Schottky contact. We have to mentioned that after 6 hours of irradiation (with the total fluence of $1.5 \times 10^{11}$ cm$^{-2}$) there was no change in the electrical properties of the Schottky diodes, thus confirming that ZnO thin films also have a high resistance to irradiation by high energy particles, similar to bulk ZnO [91].

## 3.3 ZnO thin film characterization

The ZnO thin films were characterized by scanning electron microscopy (SEM) to study the morphology of the thin films. XRD was used to identify the crystalline structure of the thin films. The optical properties of ZnO thin films were characterized using Raman spectroscopy, UV-Vis spectroscopy and photoluminescence spectroscopy (PL). Before and after irradiating the Schottky diode with alpha particle irradiation, the electrical properties were characterized using current-voltage ($I$-$V$) and capacitance-voltage ($C$-$V$) measurements. The defects in ZnO thin films were characterized using deep-level transient spectroscopy (DLTS) and Laplace-transform deep-level transient spectroscopy (L-DLTS) techniques. The characteristic of diodes on Er-doped ZnO thin films at varying concentrations were studied under light and dark conditions at room temperature using a solar simulator with 1 000 mW/cm$^{2}$.

### 3.3.1 Scanning electron microscopy (SEM)

The scanning electron microscopy (SEM) is a microscope that uses a focused electron beam to creates magnified images for the samples surfaces (topography and morphology) by scanning it with a high-energy beam of electrons [92, 93]. The electron beam energy is about 10 - 30 keV for most samples, but only several hundred eV are used for insulating samples [55]. Figure 3.4 illustrated the schematic diagram of a typical SEM, which is consists of an electron gun (electron source and accelerating anode), a lens system, a vacuum chamber contain the sample stage, a selection of detectors to collect the signals emitted from the sample and cathode ray display tube (CRT) viewing screen. The electron gun generates and accelerates electrons to between 0.1 - 30 keV. The electron lenses are used to adjust the spot size of an

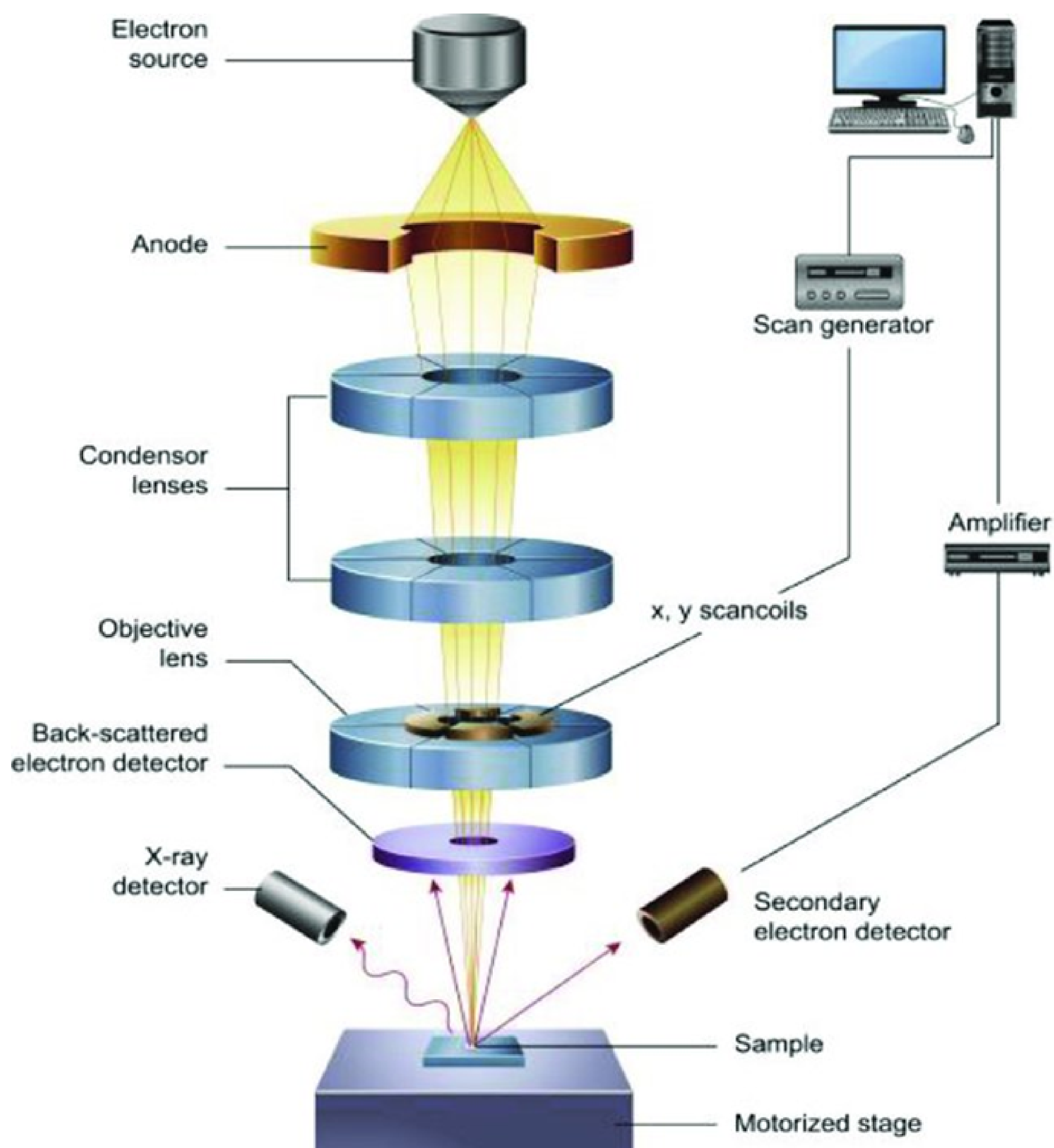


Figure 3.4: Scanning electron microscopy system [94].

electron beam and focused a narrow electron spot on the sample to produce a sharp image. In general, scanning electron microscopes can produce an electron beam at the sample with a spot size less than 10 nm that contains sufficient probe current to create an acceptable image. After interaction with the sample, different signals are produced, such as secondary electrons, backscattered electrons, characteristic and continuum X-rays, Auger electrons, diffracted backscattered electrons and heat [92]. Secondary electrons and backscattered electrons are collected by the detectors and used to form an image. Secondary electrons are used to obtain information on the morphology and topography of the samples. Backscattered electrons are used to provide contrasts in compositions in multiphase samples.

Energy dispersive X-ray spectrometry (EDS) is attachments to the SEM. EDS is used to determine the chemical and elemental composition of the specimens. The results obtained by EDS measurements consist of spectra showing peaks corresponding to the elements making up the true composition of the sample being analyzed [95].

SEM images of ZnO thin films were collected using Zeiss Gemini Ultra Plus FEG SEM at an accelerating voltage of 1 KeV. The SEM samples were coated with a thin carbon layer using carbon coater to minimize charging on the film surface. EDS was used to confirm the elemental composition of the thin films.

### 3.3.2 X-ray diffraction (XRD)

In X-ray diffraction (XRD), the X-rays are diffracted from the periodic array of atoms in the crystal, allowing a detailed study of the crystalline phases. The diffraction patterns obtained contain additional information from contributions from several micro-and macro-structural features of a sample. We can investigate the lattice parameters, chemical composition, space group, macro-stresses, or qualitative phase analysis from the peak position. The peak intensity provides information about crystal structure, such as atomic positions and temperature factors, as well as texture and quantitative phase analyses. Also, from the peak shape, one can extract information regarding microstrain and crystallite size [96].

The X-ray diffractometer consists of three essential elements (see Figure 3.5 (a)), the X-ray tube (X-ray source), a sample holder and a detector. To produce the X-rays, the metal cathode (usually a tungsten filament) is heated up to generated electrons, and these electrons are accelerated to the anode by applying a voltage (kV). When the accelerated electrons strike the anode (usually Cu or Co), characteristic X-ray spectra are produced. Obtained spectra consist of the superposition of a continuous spectrum and characteristic radiations. The most common is the $K_\alpha$ and $K_\beta$ radiation. The $K_\alpha$ radiation is used, while the other wavelengths are removed when

passing through a filter consisting of foils or a crystal monochromator. The resultant X-ray beam is focused on the sample at an incident angle $\theta$. The detector measures the intensity of the X-rays diffracted from the sample at an angle of $2\theta$ with respect to the incident ray.

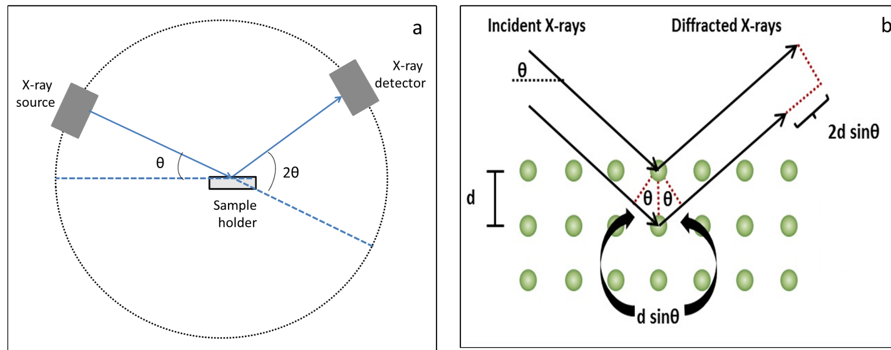


Figure 3.5: A schematic diagram of (a) a typical arrangement of XRD diffractometer components (b) Bragg analysis for X-ray diffraction by crystal planes [97].

Figure 3.5 (b) shows the geometrical condition for diffraction and the determination of Bragg's law. From Figure 3.5 (b), the incident X-ray beam is diffracted from different planes of the sample, producing the diffracted X-rays. The various diffracting crystal planes will result in different optical path lengths, and the magnitude of the path length is dependent on the distance between the crystal planes and the incident angle of the x-ray beam. The relationship between the spacing between the crystal lattice planes, angle of incidence and wavelength of the incident X-rays is known as Bragg's Law, and is expressed as [98]:

$$\lambda n = 2d \sin\theta, \tag{3.1}$$

where $n$, an integer, is the order of diffraction, $\lambda$ is the wavelength of the incident X-rays, $d$ is the interplanar spacing of the crystal and $\theta$ is the angle of incidence.

The crystallite sizes can be calculated from the XRD pattern by using an equation formulated by Paul Scherrer who studied the effect of limited particle size on X-ray diffraction patterns. This is known as Scherrer's equation [98],

$$D = \frac{k\lambda}{\beta \cos\theta}, \tag{3.2}$$

where $D$ is the crystallite size, $K$ is the shape factor, $\lambda$ is the wavelength of the incident X-ray, $\beta$ is the peak broadening at half the maximum intensity (FWHM) in radians and $\theta$ is the Bragg angle.

In this study, the XRD system used is XPERT-PRO diffractometer, PAN analytical BV, Netherlands, using a Cu $K_\alpha$ radiation with a wavelength, $\lambda$ = 0.154 nm. A Bruker D2 Phaser was also used in this study using a Cu $K_\alpha$ radiation with a wavelength, $\lambda$ = 0.15418 nm.

### 3.3.3 Raman spectroscopy

Raman spectroscopy is a vibrational spectroscopic technique that uses Raman scattering or inelastic scattering of monochromatic light. It is used to study vibrational, rotational and other low-frequency modes in a system. Usually, monochromatic light from a laser is employed as a light source. Laser power is generally held under 5 mW to reduce sample heating and decomposition [55]. When a laser beam has illuminated the sample, the photon of laser light interacts with the molecules on the sample. It can induce a short-lived transition of the molecule to an upper energy state. If the molecule relaxes to the ground state in a single step by releasing the same amount of energy as that of the incoming photon (Figure 3.6), the process is known as Rayleigh (elastic) scattering [99]. Rayleigh scattering is the most intense and needs

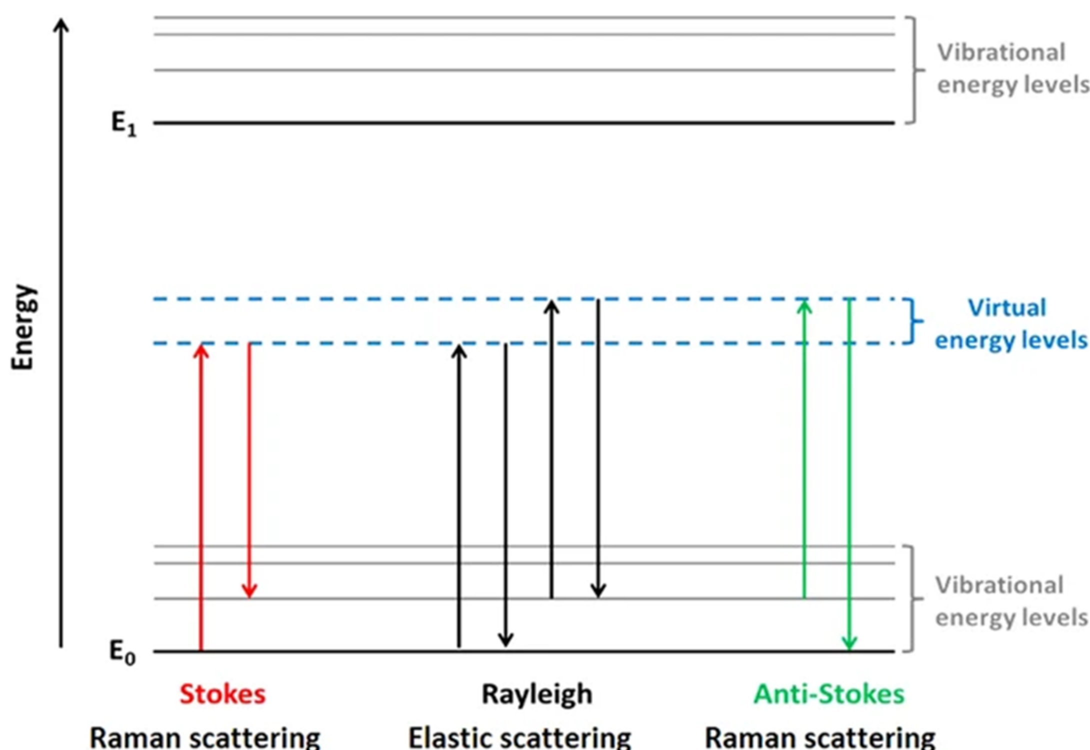


Figure 3.6: Jablonski style diagram of energetic transitions involved in Raman scattering [99].

to be rejected from the optical beam path. It can be rejected by passing the beam through a double monochromator. If not removed, it can lead to saturation of the detector and can result in unknown Raman signals from Stokes scattering [100]. Relaxation can also occur in an inelastic manner, when a molecule releases a different amount of energy compared to the incid-

ent photon. This phenomenon is called Raman scattering (also called Stokes and anti-Stokes scattering). In Stokes scattering, the energy is transferred from the incident photon to the molecule. The scattered photon has less energy than the incident photon, and the molecule is in an excited state. Conversely, if the scattered photon has more energy than the incident photon, the molecule has relaxed from an excited vibrational state to its ground state, which is called an anti-Stokes scattered process. The energy difference between the incident and scattered photons in the scattering event is called the Raman shift and is defined in energy as

$$\Delta E_R = E_L - E_S, \tag{3.3}$$

where $E_L$ is the incident photon energy and $E_S$ is the scattered photon energy. Raman shift ($\Delta E_R$) is positive for a Stokes and negative for an anti-Stokes process. Raman shifts are generally expressed in wave-numbers and will then be denoted $\Delta\bar{v}_R$, usually in units of $cm^{-1}$ [101].

Raman data of this study were collected using Jobin Yvon, Horiba TX64000 with excitation wavelength $\lambda$ = 514.5 nm. A WITec alpha 300 R focus innovations Raman spectrometer was also used in this study excited by the 532 nm line of an argon laser.

### 3.3.4 UV-Vis spectroscopy

UV-Vis spectroscopy is based on the absorption of the electromagnetic radiation in wavelength ranges of 200 - 400 nm (ultraviolet region) and 400 - 800 nm (visible region). The radiation in these wavelengths is of sufficiently high energy to induce electronic transitions in molecules or atoms [102].

Figure 3.7 shows the schematic diagram of a UV-Vis instrument. The essential components of UV-Vis spectroscopy are a light source (usually used deuterium for UV measurement and a tungsten lamp for visible measurement), a monochromator, a sample holder, and a detector. The monochromator consists of an entrance slit to narrow the beam to a usable size, a dispersion device (usually either a diffraction grating or prism that separates white light to monochromatic light of a single wavelength) and an exit slit to select the desired monochromatic wavelength.

In the UV-Vis spectroscopy technique, the light of known wavelength and intensity is focused on the sample, after passing through the sample, the final intensity is measured by a detector. The light absorbed by the sample at that particular wavelength can be easily calculated by comparing the incident radiation ($I_0$) and the transmitted radiation ($I$) [103]. Using the Beer-

Lambert law, the absorbance ($A$) is defined as [104]:

$$A = log\frac{I_0}{I} = \varepsilon lc = \alpha c. \tag{3.4}$$

the transmittance $T$ can be given as

$$T = \frac{I_0}{I} \times 100\%, \tag{3.5}$$

where $\varepsilon$ is the molar absorptivity, $c$ is the sample concentration (it can be expressed in terms of thickness of the sample), $l$ is the path length through the sample and $\alpha$ is the absorption coefficient. Both incident radiation ($I_0$) and the transmitted radiation ($I$) can be measured experimentally, and thus $A$ can be determined. The absorption coefficient $\alpha$ is dependent on the wavelength. A plot of the absorption coefficient $\alpha$ as a function of the wavelength ($\lambda$) is known as the spectrum intensity [104].

Tauc's method can be used to calculate the optical band gap using the following equation [105],

$$(\alpha h\nu)^{1/n} = A(h\nu - E_g), \tag{3.6}$$

where $\alpha$ is the absorption coefficient, $h$ is the Planck's constant, $\nu$ is the photon frequency, $E_g$ is the optical band gap, and $n$ is the nature of electronic transition with the value of $1/2$ for allowed direct band gap and for an indirect band gap $n$ equals 2.

The UV-Vis spectroscopy can be employed to measure the light reflected from the sample $I$ and compare it with the light reflected from a reference material $I_0$, and the ratio $I/I_0$ is known as the reflectance.

Before the transmittance and absorbance of the sample are measured, a pre-cleaned blank ITO or slide microscope substrate was placed with coated side facing the light source to measure the baseline correction. Then, the deposited thin films on the same substrates were placed on the one of the sample holders keeping the coated side facing the light source, and the blank substrate was placed in reference sample holder, as seen in Figure 3.7.

In this study the the optical properties (transmittance and absorbance) were studied using Varian CARY 100 BIO UV-Vis spectrophotometer in the wavelength range 300 - 800 nm.

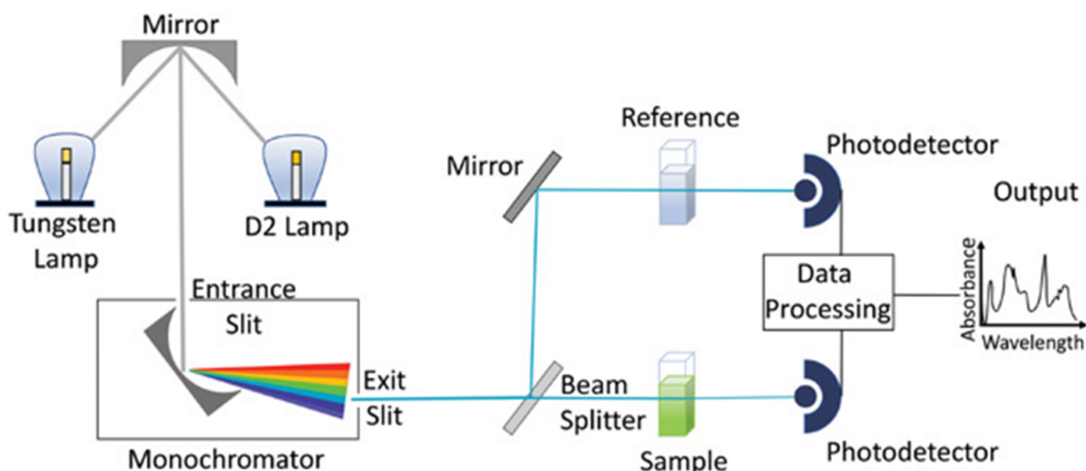


Figure 3.7: A Schematic diagram of a dual-beam UV-Vis spectrometer [106].

### 3.3.5 Photoluminescence spectroscopy (PL)

Photoluminescence (PL) is a technique in which a material absorbs photons and then re-emits photons (usually at lower energies with a smaller number of photons). PL spectroscopy analyses the distribution of energies involved in the photoabsorption and photoemission processes.

Figure 3.8 shows a schematic diagram of photoluminescence spectroscopy. In a typical PL measurement, a particular wavelength of light is selected from a light source after passing through a monochromator, then focused on the sample. Thus, it is absorbed and imparts excess energy into the material (this process is called photo-excitation). This excess energy is released through the emission of light, or luminescence (photoluminescence). The light emitted from the sample is collected through lenses, dispersed by another monochromator, and detected by a detector. An analog electrical signal generated by the photodetector is converted into a digital signal by an A/D (analog to digital) convertor and processed by software on a computer. The spectrum is displayed in terms of intensity of emitted Photoluminescence light (proportional to the electrical signal generated) as a function of the emitted light wavelength [104].

In this study, PL spectra were recorded at room temperature using two systems a Cary Eclipse fluorescence spectrophotometer (supplied with PMT detector and a xenon lamp used a wide excitation spectrum range of 200 - 1100 nm), and a He-Cd laser PL system (325 nm).

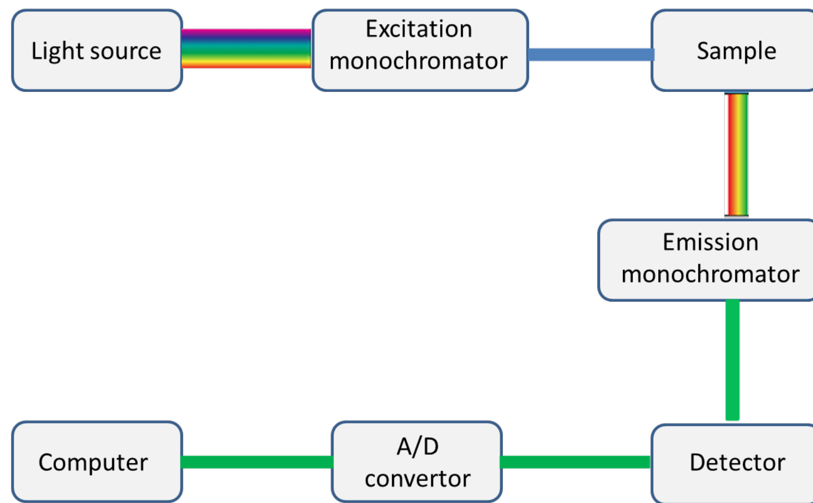


Figure 3.8: A schematic diagram of photoluminescence spectroscopy.

### 3.3.6 Current-voltage (*I*-*V*) and capacitance-voltage (*C*-*V*) measurements

After the deposition of the Pd contacts to form the Schottky diode on ZnO thin films, *I*-*V* and *C*-*V* techniques were used to evaluate the quality and electrical properties of the diode. These electrical properties including Schottky barrier height, ideality factor, saturation current and series resistance, leakage currents $I_r$ and free carrier density profiles $N_D$. Figure 3.9 shows a schematic diagram of *I*-*V* and *C*-*V* measurements.

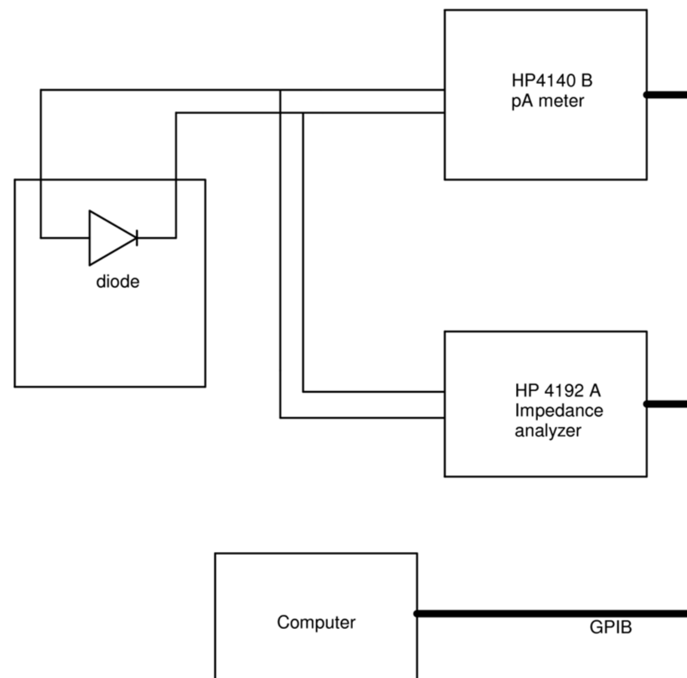


Figure 3.9: A block diagram of *I*-*V* and *C*-*V* measurements system [82].

In this study, the *I-V* characteristics were measured using an HP 4140B pA meter/ DC voltage source with a current as low as $10^{-14}$ A. The *C-V* characteristics were determined using an HP 4192A LF impedance analyzer at a bias voltage range from -2 V to 2 V at a frequency of 1 MHz. The *I-V* and *C-V* measurements were performed in the dark at room temperature.

The effect of dark and illuminated conditions on the Schottky diode properties on Er-doped ZnO thin films of different doping concentrations were studied using a Model 91150V solar simulator with solar output conditions of 1000 $W/m^2$ at room temperature and AM 1.0 G reference spectral filtering.

### 3.3.7 Deep level transient spectroscopy (DLTS) and Laplace-DLTS systems

The DLTS and Laplace-DLTS system were used to characterize the defects in ZnO thin films in the temperature range of 20 - 350 K. Figure 3.10 shows a schematic diagram of the DLTS and Laplace-DLTS system that was used in this study. The system consists of a closed cycle helium cryostat, in which the sample is mounted. A Lake Shore 332 temperature controller was used for temperature control. A fast response Boonton 7200 capacitance meter with 100 mV and 1 MHz ac voltage monitors the thermal emission of carriers after excitation by a pulse generator. Laplace card with an internal pulse generator provides the desired quiescent bias voltage and pulses. An external pulse generator, HP 33120A 15 MHz Function waveform used to provide the shorter filling pulse to the diode, which is not provided by the Laplace card [62]. All measurement parameters for DLTS and Laplace DLTS, such as bias condition, temperature measurement and capacitance transient acquisition condition, were set programmatically. The DLTS spectra are produced using different rate windows for multi-rate window scan or two rate windows for trap view scan.

In Laplace DLTS, the sample was kept at a fixed temperature and multiple capacitance transients were recorded and averaged by the Laplace DLTS card to improve the signal to noise ratio and implement the inverse Laplace transforms to calculate the emission rates and magnitude of the signal using three different software routines CONTIN, FTIKREG and FLOG [107] before displaying the Laplace spectrum.

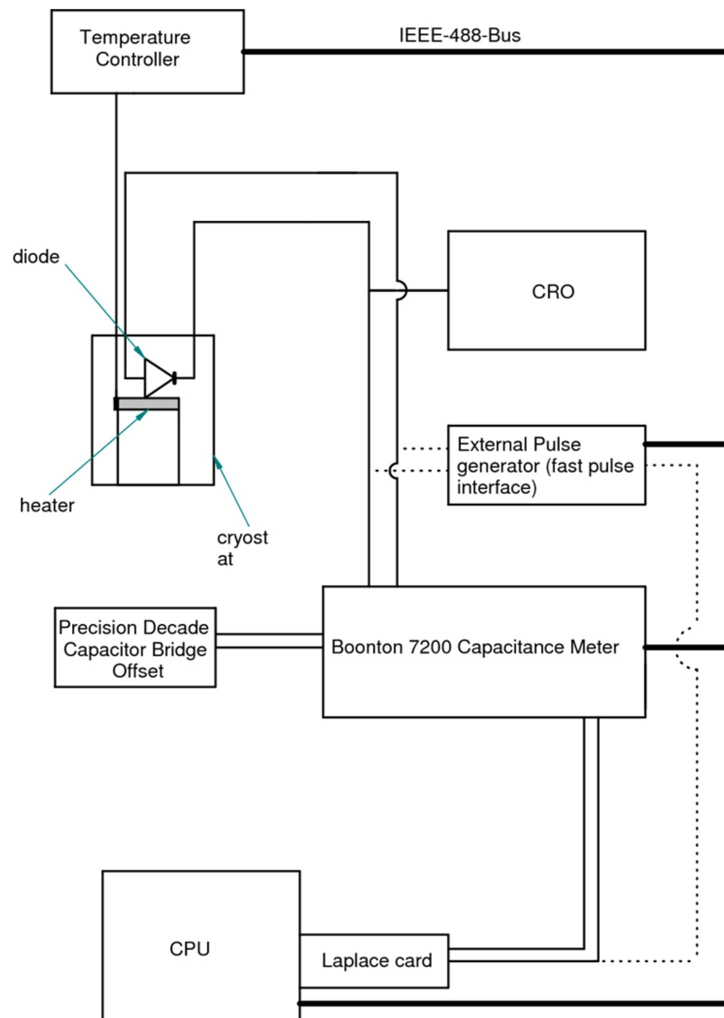


Figure 3.10: Schematic diagram of the DLTS and Laplace DLTS system. The dotted lines show the necessary connections when an external pulse generator is used [82].

# Chapter 4

# Results and discussion

## 4.1 Structural and optical characterization and the effect of alpha particle irradiation on the electrical properties of ZnO thin films prepared by sol-gel spin coating

### 4.1.1 Introduction

ZnO is a semiconductor material with a direct band gap of approximately 3.4 eV and large exciton binding energy (60 meV) at room temperature. It can thus be used in a wide range of applications such as photodiodes, single electron transistors, UV detectors and sensing applications [2, 14]. It has also been found to be highly resistant to radiation, making device applications for use in space possible [108]. ZnO thin films can be synthesized by different techniques such as pulsed laser deposition, chemical vapour deposition, spray pyrolysis and sol-gel techniques [109]. From the many techniques, sol-gel deposition is preferred in this study for the preparation of high-quality ZnO thin films due to its low cost, simplicity and ability to deposit large area films [110]. The quality, structure and properties of ZnO thin films and devices are influenced by fabrication parameters and techniques used [36].

Defects in semiconductors may be impurities or crystalline defects. Impurities can be introduced either intentionally or unintentionally during crystal growth and device processing [55]. The performance of ZnO-based devices is affected by the presence of impurity atoms and point defects such as oxygen vacancies $V_o$ and zinc interstitials $Zn_i$ because these defects create electronic states in the band gap of ZnO [111].

For space-based applications, especially those in near earth orbit, the devices need to operate

in harsh radiation conditions and information on the effect of radiation on device performance is required. In particular, the Van Allen belt contains high fluxes of electrons up to 10 MeV, and protons $>$ 10 MeV [108]. In recent years there has been a shift from bulk semiconductors to thin film semiconductor devices and there is a need to determine the radiation resistance of these devices.

This section contains the results that have been obtained from ZnO thin films prepared by sol-gel spin coating, and sheds more light on the effect of alpha particle irradiation on the electrical properties of and defects in sol-gel ZnO thin films. The structure, surface morphology and optical properties are also discussed.

### 4.1.2 Surface and structure of ZnO thin films

Scanning electron microscope (SEM) studies of the ZnO thin films after annealing at 600 °C showed large grains as seen in Figure 4.1 (a) with diameters of $\sim$100 nm. The crystallite grew and packed closely. The crystallite size was calculated from the XRD data and found to be 48 nm (see Table 4.1). Figure 4.1 (b) shows the cross-sectional view of a deposited ZnO thin film with a thickness of approximately 800 nm. Stacking layers and some voids are visible in the film. The crystallite size, thickness and number of voids depend on the annealing temperature and duration [112].

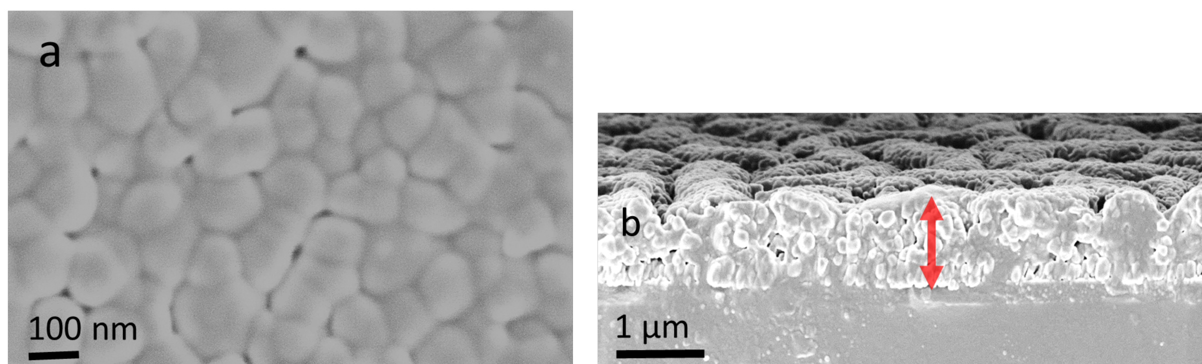


Figure 4.1: SEM images of the (a) surface and (b) cross-section of ZnO thin films deposited on ITO/glass substrate.

Figure 4.2 shows the X-ray diffraction patterns of ZnO thin films deposited onto a ITO/glass substrate. In the XRD patterns there are strong peaks corresponding to the (100), (002) and (101) planes. Small peaks corresponding to the (102) and (110) planes were also observed. These peaks indicate that the films have the hexagonal wurtzite structure. It is clear from this pattern that the film consists of randomly orientated polycrystalline particles with a slight preferred orientation along the (002) plane. The peaks marked with an asterisk (*) are related

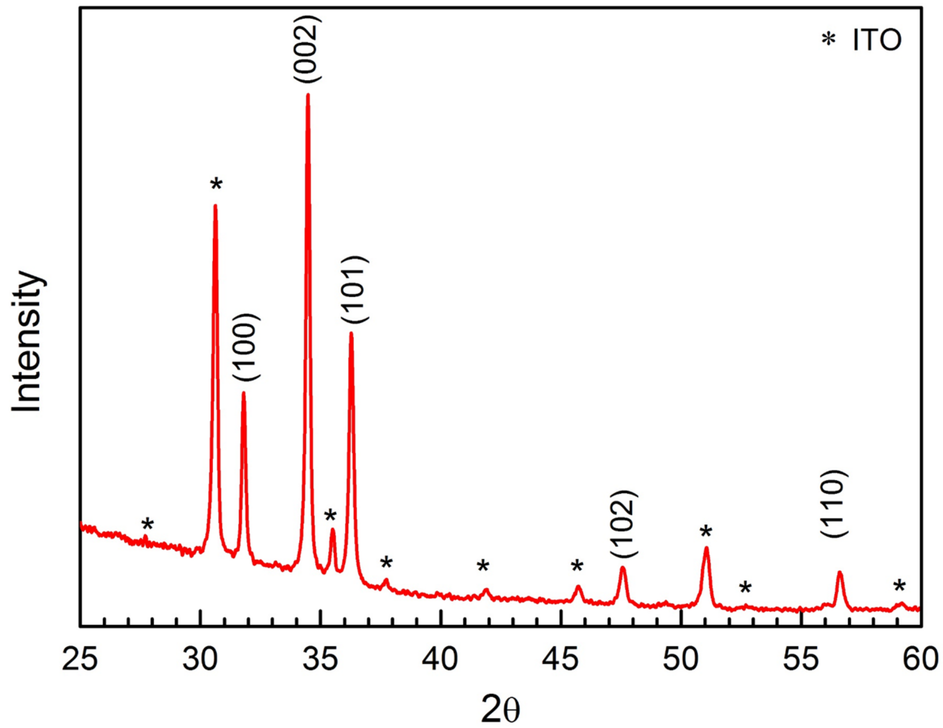


Figure 4.2: The X-ray diffraction (XRD) patterns of ZnO thin films deposited onto ITO/glass substrate after annealing at 600 °C.

to the ITO substrate. The values of the lattice constants obtained are in good agreement with the values from the JCPDS data with card number (76-0704) and are shown in Table 4.1. The crystallite size $D$ of the ZnO thin films was calculated from Equation (3.2).

Table 4.1: Structural and lattice parameters of ZnO thin films

| FWHM | $2\theta$ | | $D$ (nm) | $\delta$ (nm)$^{-2}$ | Lattice constants (Å) | | Lattice constants (Å) from (JCPDS) | | Band gap (eV) |
|---|---|---|---|---|---|---|---|---|---|
| (002) | (100) | (002) | (002) | (002) | $a$ (100) | $c$ (002) | $a$ | $c$ | |
| 0.181 | 31.805 | 34.477 | 48 | 0.0004 | 3.246 | 5.198 | 3.253 | 5.213 | 3.23 |

### 4.1.3 Raman and UV-Vis spectroscopy

Figure 4.3 shows the Raman spectra of a ZnO thin film deposited onto a ITO/glass substrate and excited by the 523 nm line of an argon laser at room temperature. The sharp peak located at 438 cm$^{-1}$ corresponds to the $E_2$(high) mode of the wurtzite ZnO structure, the peaks located at 332 and 381 cm$^{-1}$ correspond to the $E_2$(high)-$E_2$(low) and $A_1$(TO), respectively. The broad peak (marked by an arrow) corresponds to the $A_1$(LO) and is attributed to the presence of

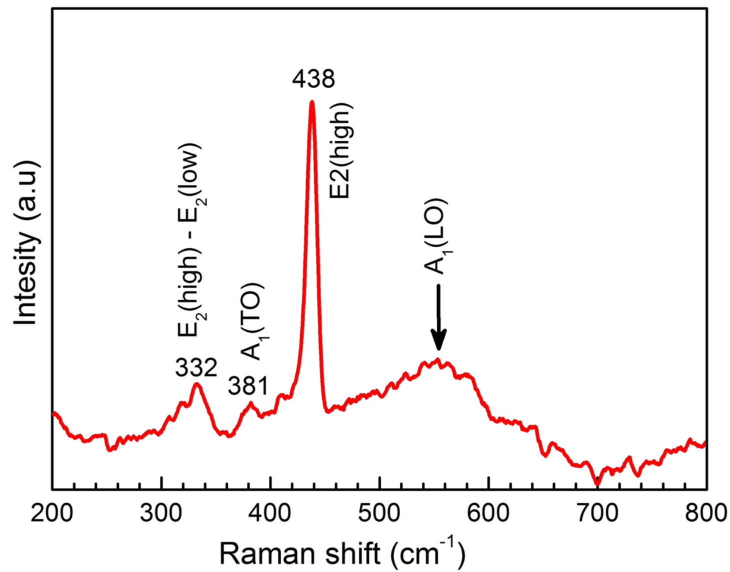


Figure 4.3: The Raman spectra of a ZnO thin film deposited onto ITO/glass substrate after annealing at 600âŮęC.

defects [113].

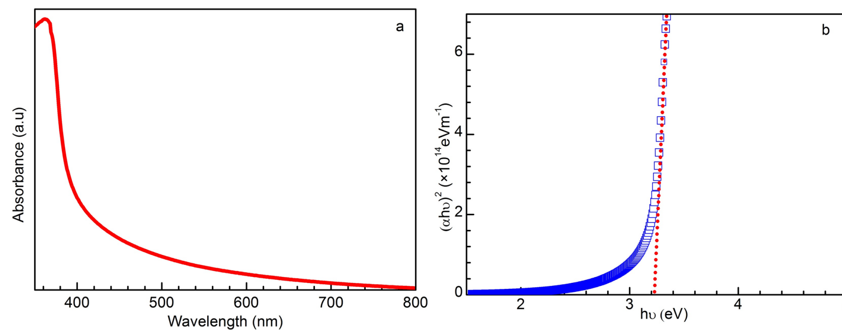


Figure 4.4: UV-Vis spectra of ZnO thin films deposited on ITO substrate (a) Absorbance (b) Tauc plot.

The UV-Vis spectrum of the deposited film is shown in Figure 4.4. From Figure 4.4 (a), the thin films exhibited a high absorption peak at 362 nm in the UV region. This absorption decreased gradually in the visible and IR region because ZnO has high transmittance in the visible spectra due to its band gap of $\sim$ 3.40 eV. Figure 4.4 (b) shows Tauc method which was used to calculate optical band gap using the Equation (3.6).

The optical band gap was obtained at the $h\nu$ axis intercept of an extrapolated linear fit of the graph as 3.23 eV. The lower value of the band gap energy may be due to the presence of defects which were introduced during sample preparation. M. Saleem *et al.* [109] observed a decrease in the band gap of ZnO thin films after annealing at different temperatures, and attributed this to the increase of ZnO grain size during annealing.

### 4.1.4 *I-V* and *C-V* measurements

Figure 4.5 shows the characteristic room temperature *I-V* plot of the Pd/ZnO/n-Si/AuSb Schottky barrier diodes before and after alpha particle irradiation. The rectification before and after irradiation were 3 and 2.5 orders of magnitude, respectively. After irradiation, the barrier height of the diodes decreased, causing an increase in the thermionic emission current. Although the generation-recombination current also increased, the voltage at which the dominant charge transport mechanism changed from generation-recombination to thermionic emission changed from 0.5 V to 0.2 V after irradiation. In both cases, series resistance dominated at higher currents, with the series resistance after irradiation being slightly lower. The diode parameters shown in Table 4.2 were calculated by performing a linear fit in forward bias region using thermionic emission Equation 2.5.

Irradiation caused an increase in leakage current and a slight increase in the ideality factor as well as a decrease in series resistance and the Schottky barrier height (SBH). The increase in leakage current and ideality factor are attributed to irradiation induced defects and interface states in ZnO thin films [111].

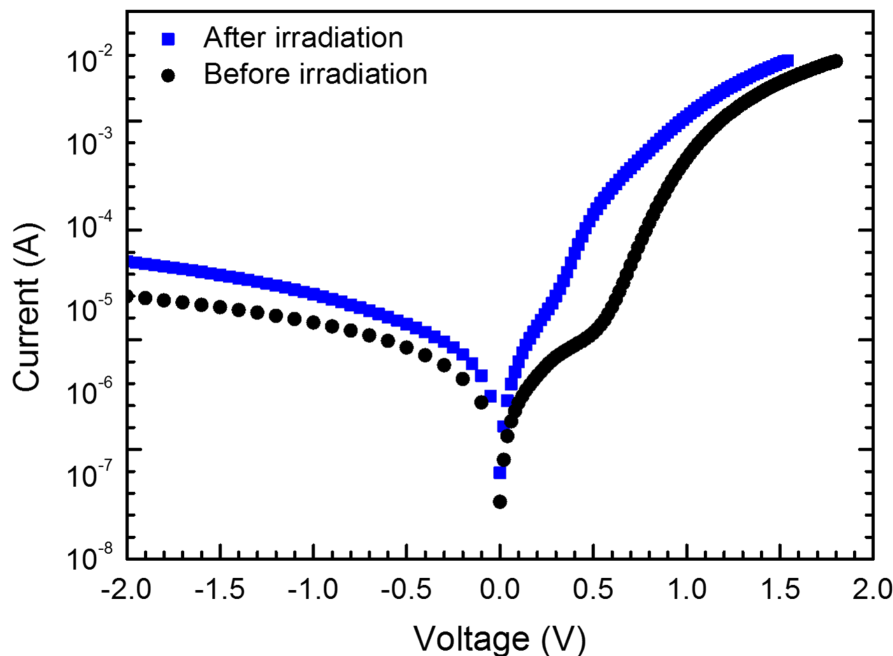


Figure 4.5: Room temperature semi-logarithmic plot of *I-V* measurements of Pd/ZnO/n-Si/AuSb Schottky diode before and after irradiation with alpha-particles.

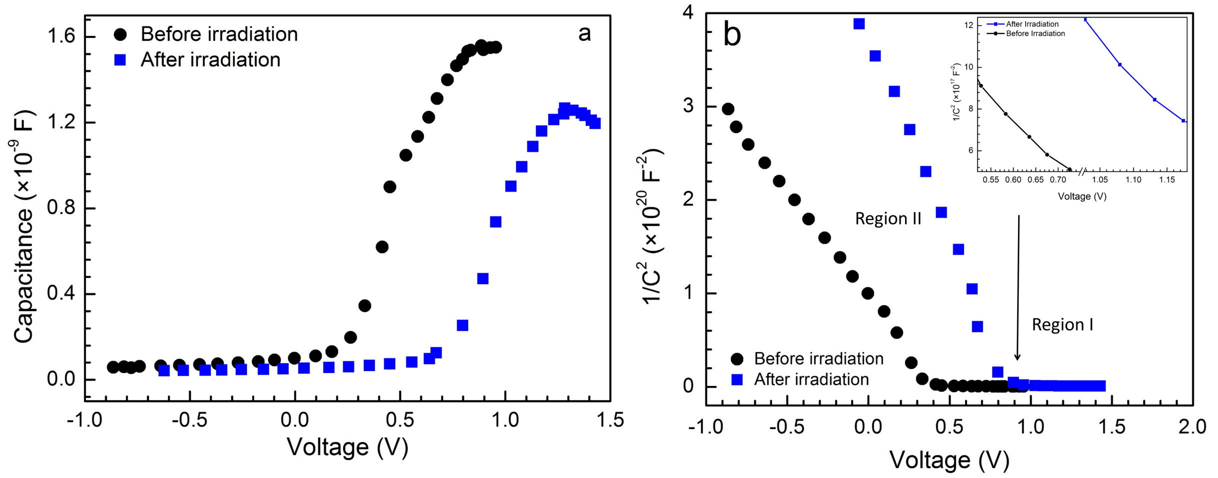


Figure 4.6: $C$-$V$ measurements before and after irradiation at room temperature at 1 MHz.

Table 4.2: The Schottky diode parameters from $I$-$V$ and $C$-$V$ measurements before and after irradiation.

| Events | SBH (eV) | | Ideality | Saturation current, $I_s$ | Series | $N_D$ (cm$^{-3}$) |
|---|---|---|---|---|---|---|
| | $I$-$V$ | $C$-$V$ | Factor $(n)$ | (A)$\times 10^{-9}$ | Resistance ($\Omega$) | $\times 10^{17}$ |
| Before irradiation | 0.635 | 1.24 | 3.41 | 11.2 | 53 | 12 |
| After irradiation | 0.536 | 1.18 | 3.48 | 519 | 43 | 4.0 |

The $C$-$V$ characteristics before and after irradiation at room temperature are shown in Figure 4.6 (a). Figure 4.6 (b) shows the $1/C^2$ vs $V$ curves which are split into two regions: Region I and region II. The free carrier concentration calculated from the region I of $\sim 10^{15}$ cm$^{-3}$, and is related to n-Si. On the other hand, the free carrier concentration calculated from region II (see Figure 4.6 (b) inset) was $\sim 10^{17}$ cm$^{-3}$, this being the free carrier concentration of the ZnO. The capacitance and free carrier concentration ($N_D$) decreased after irradiation. E. Gür *et al.* [114] observe the decrease of the capacitance and free carrier concentration after studying the effects of high energy electron irradiation on electrical properties of Au/n-ZnO Schottky diodes and attributed the decrease in the carrier concentration to the trapping effect of the deep defect states produced by high energy electron irradiation. The Schottky barrier height obtained from $C$-$V$ measurements is greater than that obtained from $I$-$V$ measurements, this due to inhomogeneity in SBH and image force effects [115].

### 4.1.5 Energy band diagram of Pd/ZnO/n-Si heterojunction

Figure 4.7 shows the energy band diagram of the Pd/ZnO/n-Si heterojunction at thermal equilibrium and after applying a reverse bias, constructed based on Anderson's model [116].

Both the ZnO thin film and the Si are n-type semiconductors with carrier concentrations $N_D$ of $12 \times 10^{17} \text{cm}^{-3}$ and $\sim 10^{15}$ $\text{cm}^{-3}$, respectively calculated from *C*-*V* measurements. Thus, the Fermi level in n-ZnO and n-Si should be close to the conduction band edge at equilibrium (see Figure 4.7 (a)). For n-type semiconductors the Schottky barrier height is predicted by [56]:

$$\phi_{B,eff} = \Phi_m - \chi_{ZnO}, \tag{4.1}$$

where $\Phi_m$ is the work function of Pd metal = 5.12 eV and $\chi_{ZnO}$ is the electron affinity of ZnO = 4.35 eV [117]. Thus, the $\phi_{B,eff}$ calculated is as 0.77 eV. The experimental SBH before and after irradiation was 0.635 eV and 0.536 from *I*-*V* measurements and 1.24 eV and 1.18 eV from *C*-*V* measurements. The $\phi_{B,eff}$ obtained from simple theory is slightly greater than $\phi_{B,eff}$ obtained from *I*-*V* measurements and smaller than $\phi_{B,eff}$ from *C*-*V* measurements. The difference in simple theory compared to experimental results of SBH calculated from *C*-*V* measurements is due to the presence of surface states while the lower barrier height obtained during *I*-*V* measurements is a combination of surface inhomogeneity and image force barrier lowering.

According to Anderson's model, the conduction band offset and valence band offset is given by:

$$\Delta E_C = \chi_{ZnO} - \chi_{Si}, \tag{4.2}$$

$$\Delta E_v = (E_{gZnO} - E_{gSi}) + \Delta E_C, \tag{4.3}$$

where $\chi_{Si}$ is the electron affinity of Si = 4.05 eV [118], thus $\Delta E_C$ calculated of 0.3 eV.
From Equation 4.3, $E_{gZnO}$ is the band gap of ZnO of 3.23 eV calculated from Tauc's plot shown in Figure 4.4 (b), $E_{gSi}$ is the band gap of n-Si of 1.20 eV, so the valance band offset $\Delta E_v$ is calculated as 2.33 eV.

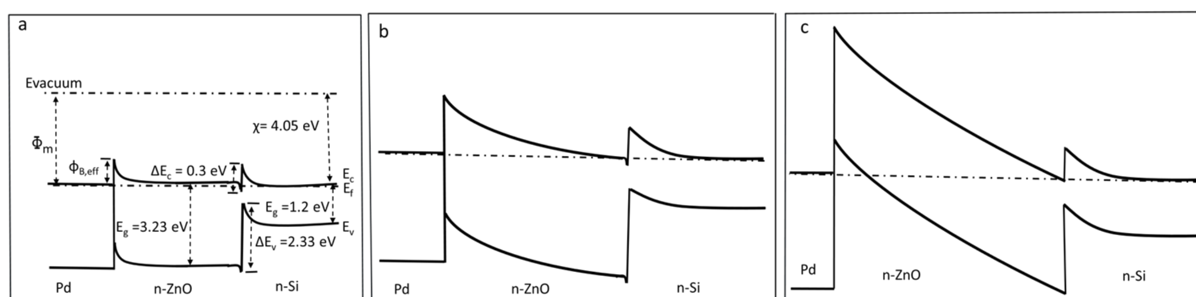


Figure 4.7: Energy band diagram of Pd/ZnO/n-Si heterojunction (a) Under thermal equilibrium (b) After applying a small reverse bias (c) After increasing the reverse bias.

### 4.1.6 DLTS and Laplace DLTS measurements

The DLTS spectrum exhibited one peak before irradiation labelled $E_4$, Figure 4.8 (a). When investigated by Laplace DLTS, the $E_4$ exhibited only one energy leve. This defect has been observed by Auret *et al.* [119] in vapor-phase-grown single-crystal ZnO. Mtangi *et al.* [120] also observed this peak in bulk ZnO and they attributed it to the oxygen vacancy.

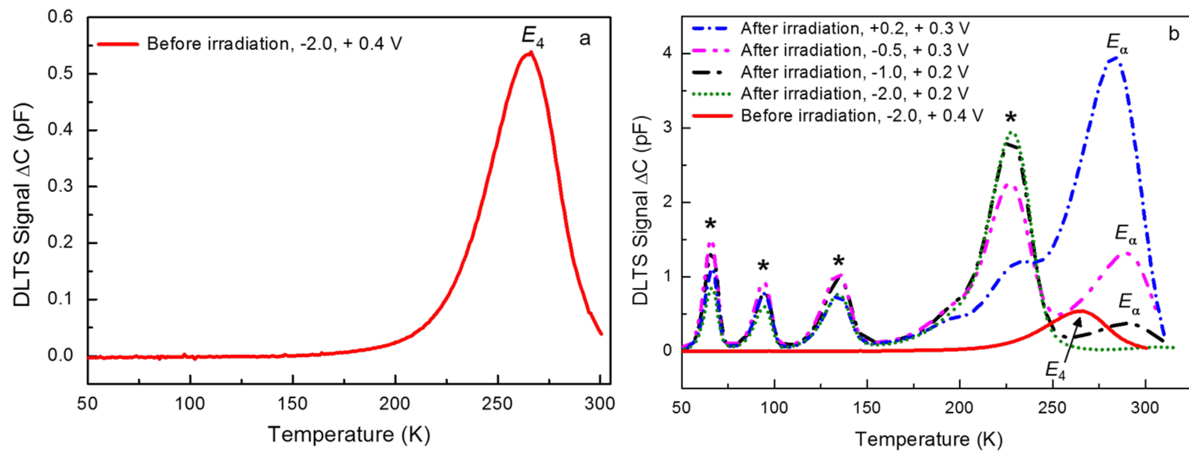


Figure 4.8: DLTS spectra obtained from Pd/ZnO/n-Si/AuSb Schottky diode (a) before and (b) after irradiation, recorded at different a quiescent reverse bias, different filling pulse amplitude, filling pulse width of 1 ms and rate window of 80.2 Hz in the temperature range 50 - 350 K.

Figure 4.8 (b) shows the presence of a new peak labelled $E_\alpha$, introduced by alpha particle irradiation. Using Laplace DLTS under reduced bias (see Figure 4.9), the $E_\alpha$ was found to be made up of two defects at energy levels $E_{\alpha 1}$ = 0.53 eV and $E_{\alpha 2}$ = 0.36 eV below the conduction band. The shift in Laplace DLTS spectra of $E_{\alpha 1}$ and $E_{\alpha 2}$ defects measured at three temperatures are displayed in Figure 4.9. The apparent capture cross sections of $E_{\alpha 1}$ and $E_{\alpha 2}$ were calculated from Arrhenius plots shown in Figure 4.10, and found to be $7.7 \times 10^{-14}$ cm$^2$ and $2.3 \times 10^{-16}$ cm$^2$, respectively. The electronic properties are summarized in Table 4.3.

There are four peaks observed in all curves (see Figure 4.8 (b)) after irradiation located below 250 K and labelled by (*), their signatures are attributed to defects in the n-Si substrate. Under a quiescent reverse bias of -2.0 V and filling pulse amplitude $V_p$ = 2.2 V, only defects in the n-Si were observed, as shown by the dotted curve (green) in Figure 4.8 (b).

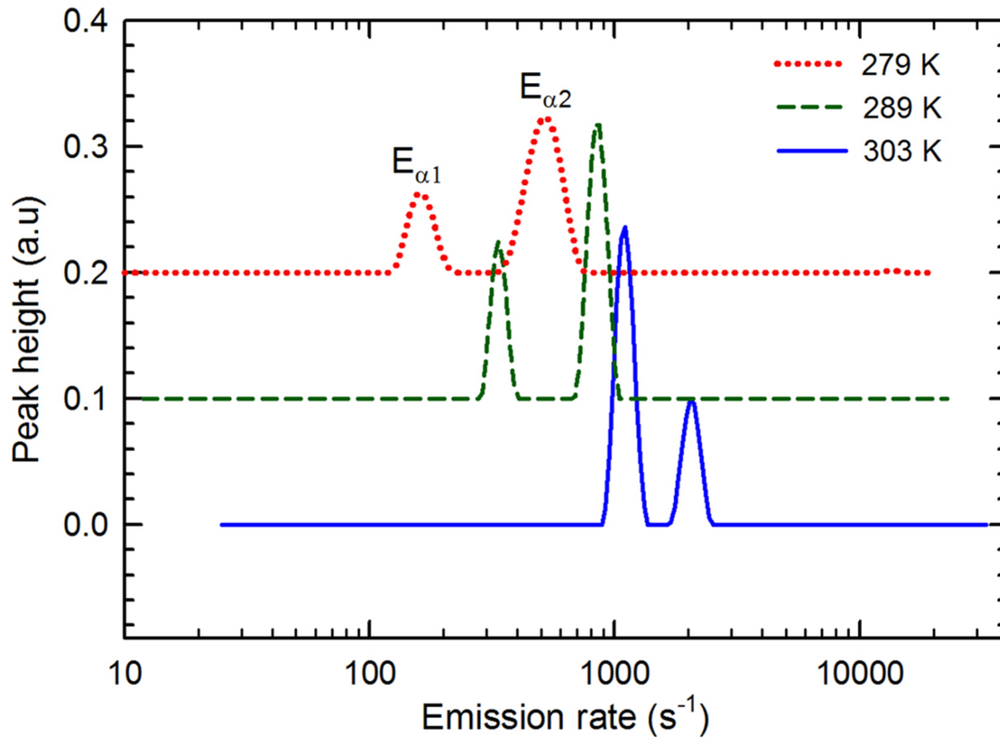


Figure 4.9: Laplace DLTS spectra showing the shift of $E_{\alpha 1}$ and $E_{\alpha 2}$ defects at three temperatures in ZnO thin films after irradiation.

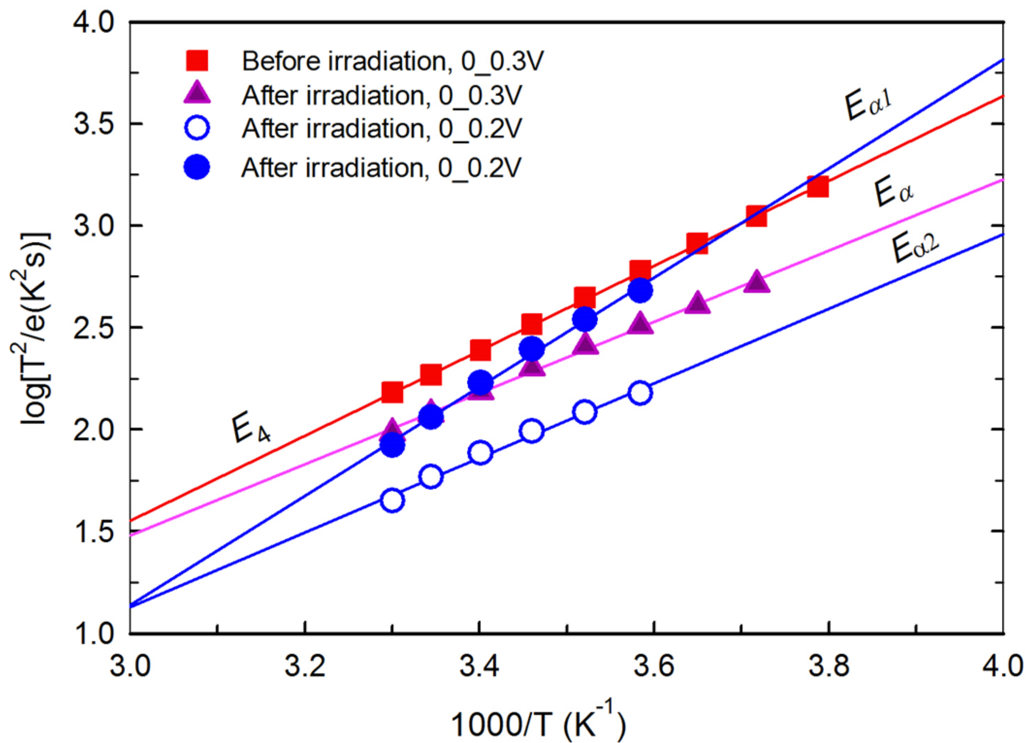


Figure 4.10: Arrhenius plots of the defects in ZnO thin films, obtained at a quiescent reverse bias of 0 V with a filling pulse amplitude of 0.3 V for $E_4$, $E_\alpha$ and 0.2 V for $E_{\alpha 1}$ and $E_{\alpha 2}$. The filling pulse width was 1 ms.

Table 4.3: The defect energy $E_T$ below conduction band and the apparent capture cross-section $\sigma_{ap}$ of defects in ZnO thin films deposited on the n-Si substrate.

| Defect label | $E_T$ (eV) | $\sigma_{ap}$ ($cm^2$) |
|---|---|---|
| $E_4$ | 0.41 | $4.8 \times 10^{-16}$ |
| $E_\alpha$ | 0.35 | $5.7 \times 10^{-17}$ |
| $E_{\alpha 1}$ | 0.53 | $7.7 \times 10^{-14}$ |
| $E_{\alpha 2}$ | 0.36 | $2.3 \times 10^{-16}$ |

### 4.1.7 Summary

The surface morphology and structure of ZnO thin films deposited by the sol-gel spin coating showed the films to have hexagonal wurtzite structure, which was confirmed by Raman spectra. The optical band gap of the ZnO thin films was calculated to be 3.23 eV.

From *I-V* and *C-V* characteristics, the SBH decreased after alpha particle irradiation and ideality factor and leakage current increased. The DLTS technique was used to identify the defects in the ZnO thin films before and after irradiation. It revealed a single defect before irradiation with an activation enthalpy of 0.41 eV. The defect with energy level 0.35 eV below the conduction band was observed after alpha particle irradiation. The 0.35 eV level was split using Laplace DLTS and found to consist of two defects at 0.53 eV and 0.36 eV. The relative heights of the peaks changed with biasing conditions, showing that the depletion region could be manipulated to profile through the ZnO-Si heterojunction.

### 4.1.8 Publication: The effect of alpha particle irradiation on electrical properties and defects of ZnO thin films prepared by sol-gel spin coating

https://doi.org/10.1016/j.mssp.2019.05.029

## 4.2 Effect of Er and Yb doping and temperature on electrical properties of ZnO thin films Schottky diode prepared by sol-gel spin coating

### 4.2.1 Introduction

ZnO is one of the II-VI semiconductor materials with a wide direct band gap of approximately 3.4 eV and a large exciton binding energy of 60 meV at room temperature [46]. ZnO has interesting electrical properties, such as high electron mobility, high electron saturation velocity and good thermal stability [121], as well as having high resistance to radiation damage, making it an excellent candidate for optoelectronic devices and space applications [108]. ZnO is a very attractive host lattice for doping with different elements to tailor the optical, electrical and magnetic properties due to its excellent physical and chemical stability [9]. Rare-earth elements have been used as dopants for many applications, for example, optoelectronic devices such as visible and infra-red luminescent devices, based on their optical emission occurring within intra 4f-4f shell transitions [10, 11].

In order to understand the electrical properties of semiconductor materials, there are many semiconductor-based devices such as metal-semiconductor interfaces, p-n junctions, heterojunction interfaces, and metal-oxide-semiconductor devices that can be used [12]. Among these devices, metal-semiconductor contacts (M-S) have been used to produce devices such as Schottky barrier diodes. High performance of ZnO-based devices require fabricating high-quality Schottky barrier diodes, which is not easy because the quality of Schottky barrier diode depends on the quality of the interface between the ZnO surface and the metal, as well as residual surface contamination and defects in the semiconductor [13]. A study of the electrical properties of Schottky barrier diodes at different temperatures is necessary since these properties are temperature dependent and the current transport mechanisms change under different temperature conditions and the quality of the rectifying contacts at different temperatures must be monitored.

Recently, there have been extensive studies on rare-earth doped ZnO using different physical and chemical techniques. Among these, the sol-gel method is preferred due to advantages such as low cost, simplicity, easy adjustment of composition, and deposition on large areas [122]. These studies show that dopants influence structural, optical, electrical and magnetic properties [123–127], and many attempts have been reported to improve ZnO-based Schottky diode properties and study the diode parameters at different temperatures [128–130]. Relatively few studies have reported on rare earth doped-ZnO thin film Schottky diodes [53, 54], and to the

authors knowledge, there have been no reports on the temperature dependence of electrical properties and defects in Er-doped and Yb-doped ZnO thin films Schottky diodes using *I-V*, *C-V*, DLTS and L-DLTS techniques.

This section reports on the effect of Er and Yb (both in 3 at.%) doping on surface morphology, optical and electrical properties of ZnO thin films. The temperature-dependence of electrical properties of Er-doped and Yb-doped ZnO Schottky diodes in the temperature range of 50 - 290 K using current-voltage (*I-V*) and capacitance-voltage (*C-V*) measurements will be discussed. The defects in Er-doped and Yb-doped ZnO thin films were studied using DLTS and L-DLTS techniques.

### 4.2.2 Surface and structure of ZnO thin films

Figure 4.11 shows the SEM images of the undoped, 3 at.% Er-doped and 3 at.% Yb-doped ZnO thin films. These images clearly show that the grain size of ZnO thin films varied with different dopant ions. The undoped ZnO thin films form small grains which were uniformly distributed (Figure 4.11 (a)). Using the same processing conditions, the Er-doped ZnO (Figure 4.11 (b)) grain shape was found to be rod-shaped. The Yb-doped ZnO film, Figure 4.11 (c), also showed rod-shaped grains, similar to the Er-doped ZnO sample, but larger in size. There were also smaller particles observed on the surface of the Yb-doped ZnO sample which could be related to $Yb_2O_3$, which was observed in the XRD study. The small particles were also observed by Heng *et al.* [131] in (Ce, Yb) co-doped ZnO thin films deposited by magnetron sputtering. Nan Jiang *et al.* [132] observed these particles in Yb and Li co-doped ZnO using the solid state reaction method. The cross section of the films was showed in Figure 4.11 (d), and the average thickness of the films was found to be $\sim$ 600 nm.

In order to confirm the presence of Er and Yb in the samples, their chemical composition was determined using EDS analysis (see Figure 4.11). The EDS results confirmed the presence of O, Zn, Er and Yb in the final products. The other peaks such as Si and Ca peaks are originated from the glass substrate. Since the glass substrate made with silica and contains the Ca [133].

The X-ray diffraction (XRD) patterns of the undoped, Er-doped and Yb-doped ZnO thin films deposited onto a glass substrate are shown in Figure 4.12. The peaks corresponding to the ZnO wurtzite structure were observed. The Yb-doped ZnO thin films showed evidence of the presence of $Yb_2O_3$ with the (222) peak of the cubic phase of $Yb_2O_3$ being identified at $2\theta = 29.5^{\circ}$ (JCPDS data card number 006-0371). Lluscá *et al.* [48] observed a similar peak in Er and Yb-doped ZnO thin films deposited using RF magnetron sputtering.

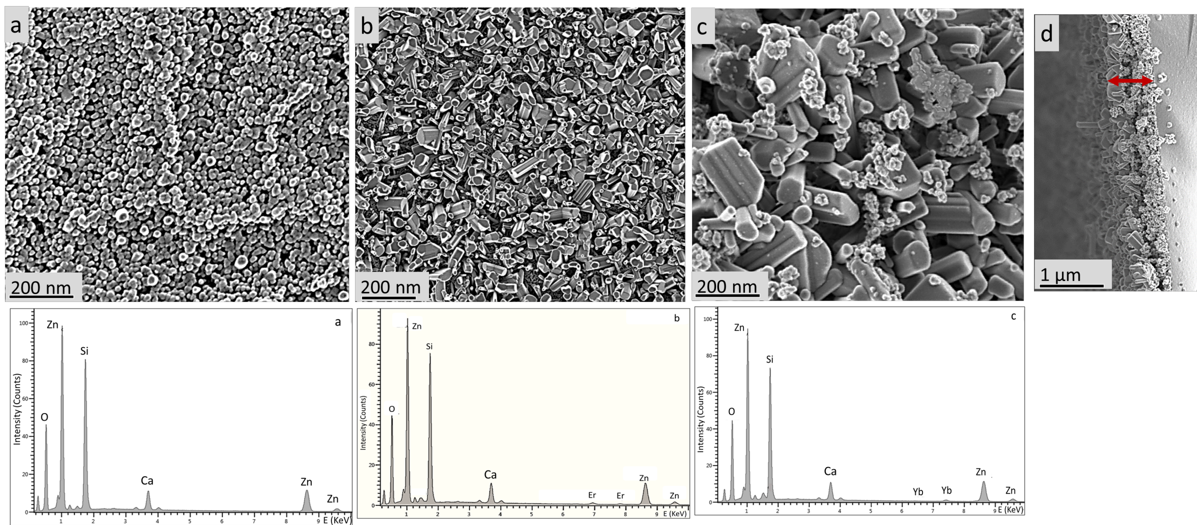


Figure 4.11: SEM images and EDS plot of (a) undoped ZnO (b) Er-doped ZnO (c) Yb-doped ZnO and (d) cross section of Yb-doped ZnO thin films deposited on microscope slide substrates, dried at 200 °C and annealed at 600 °C in air for 1 hour.

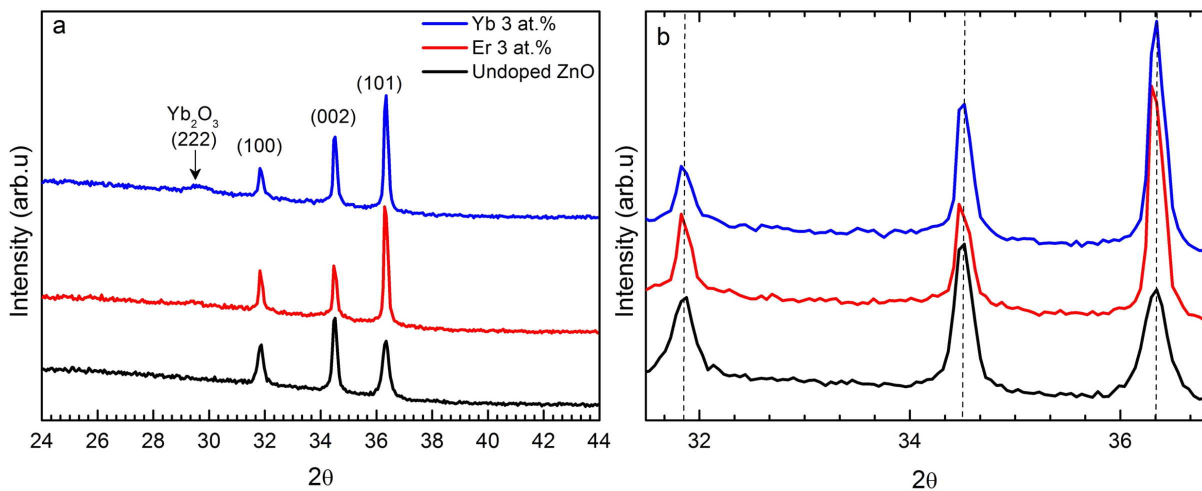


Figure 4.12: (Color online) (a) The X-ray diffraction (XRD) patterns of undoped, Er-doped and Yb-doped ZnO thin films deposited on microscope slide substrates, (b) enlargement showing the shift in the (100), (002) and (101) diffraction peaks of the doped films to lower angles compared to the undoped ZnO peak positions.

Otal *et al*. [126] also observed this peak in Yb-doped ZnO prepared by wet chemistry. There was no secondary phase observed in the Er-doped ZnO sample, which indicates that $Er^{3+}$ ions have been incorporated into the ZnO lattice. The intensity of the (101) peak increased indicating some preferred orientation, while the intensity of the (002) peak decreased after doping comparing to the undoped ZnO peaks. The full-width at half-maximum (FWHM) of the (002) plane decreased as a result of doping (see Table 4.4), and can be attributed to improved crystallinity. The doped ZnO peak positions shifted to lower diffraction angles (see Figure 4.12 (b)) compared to the undoped ZnO film and this is due to the difference in ionic

Table 4.4: Structural and lattice parameters of undoped and doped ZnO thin films.

| Plane | FWHM | $2\theta$ | | $D$ (nm) | $\delta \times 10^{-4}$ (nm)$^{-2}$ | Lattice constants (Å) | | c/a |
|---|---|---|---|---|---|---|---|---|
| | (002) | (100) | (002) | (002) | (002) | $a$(100) | $c$ (002) | |
| Undoped ZnO | 0.196 | 31.874 | 34.514 | 42 | 5.6 | 3.242 | 5.197 | 1.603 |
| Er | 0.161 | 31.831 | 34.472 | 51 | 3.8 | 3.246 | 5.203 | 1.603 |
| Yb | 0.152 | 31.831 | 34.485 | 54 | 3.4 | 3.246 | 5.201 | 1.602 |
| JCPDS 76-0704 | | 31.762 | 34.406 | | | 3.253 | 5.213 | 1.603 |

radius between $Zn^{2+}$ and dopants (the ionic radius of $Er^{3+}$ (0.89 Å) and $Yb^{3+}$ (0.87 Å) is greater than the ionic radius of $Zn^{2+}$ (0.74 Å)), and this explains the increase in values of the lattice constants. The values of the lattice constants from the JCPDS data with card number 76-0704 are a = 3.253 Å, and c = 5.213 Å. The values obtained from the undoped and doped ZnO thin films (see Table 4.4) are slightly different compared to the JCPDS data values. The crystallite size $D$ of undoped and doped ZnO thin films was calculated from Equation 3.2, and was found to increase with doping, while the dislocation density $\delta$ was found to decrease with doping.

### 4.2.3 Raman spectroscopy and photoluminescence spectroscopy

The room temperature Raman spectra of the undoped, Er-doped and Yb-doped ZnO thin films excited by the 523 nm line of an argon laser are shown in Figure 4.13. The strong peaks observed correspond to $E_2$ (low) phonon mode at about 99 cm$^{-1}$ and the $E_2$ (high) phonon mode at about 438 cm$^{-1}$ indicative of the ZnO hexagonal wurtzite crystal structure. The $E_2$ (low) mode is related to the Zn sublattice, whereas the $E_2$ (high) mode is associated with the motion of oxygen atoms and sensitive to internal stress [30, 134]. The broad peak located at 575 cm$^{-1}$ corresponding to the $A_1$ (LO) phonon mode, is related to lattice defects such as oxygen vacancies and Zn interstitials [11]. The peaks at 480 cm$^{-1}$, 383 cm$^{-1}$ and 333 cm$^{-1}$ correspond to the 2LA phonon mode, the $A_1$ (TO) phonon mode and the $E_2$ (high) - $E_2$ (low) phonon mode, respectively. The 2LA and $E_2$ (high) - $E_2$ (low) are second order features due to multi-phonon processes [135]. Three additional peaks at 120 cm$^{-1}$, 160 cm$^{-1}$ and 520 cm$^{-1}$ have been observed in the Er-doped ZnO sample, and may be related to local vibration modes due to the Er substitution in the ZnO host and defect concentration in the host, as reported by Zamiri *et al.* [136]. The peak at 204 cm$^{-1}$ observed in undoped and Yb-doped ZnO thin films samples and correspond to the $2E_2$ (low) second order phonon mode [136]. Same peak has been observed by Youjin Zheng *et al.* [137] in the $Yb_2O_3$ nanoparticles. Thus this peak could be related to the $Yb_2O_3$ and confirmed by XRD results.

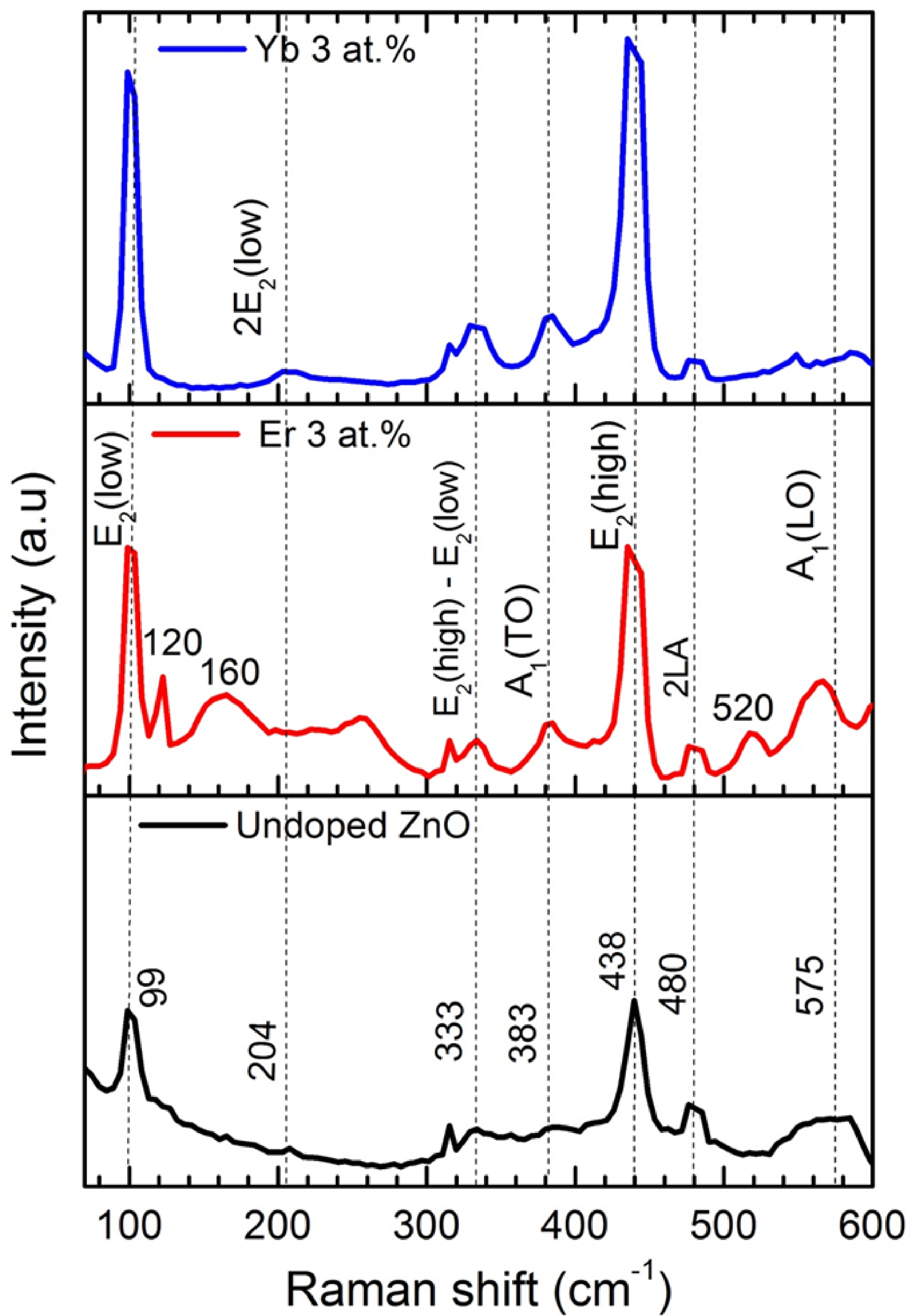


Figure 4.13: (Color online) Raman spectra of undoped, Er-doped and Yb-doped ZnO thin films deposited onto microscope slide substrates.

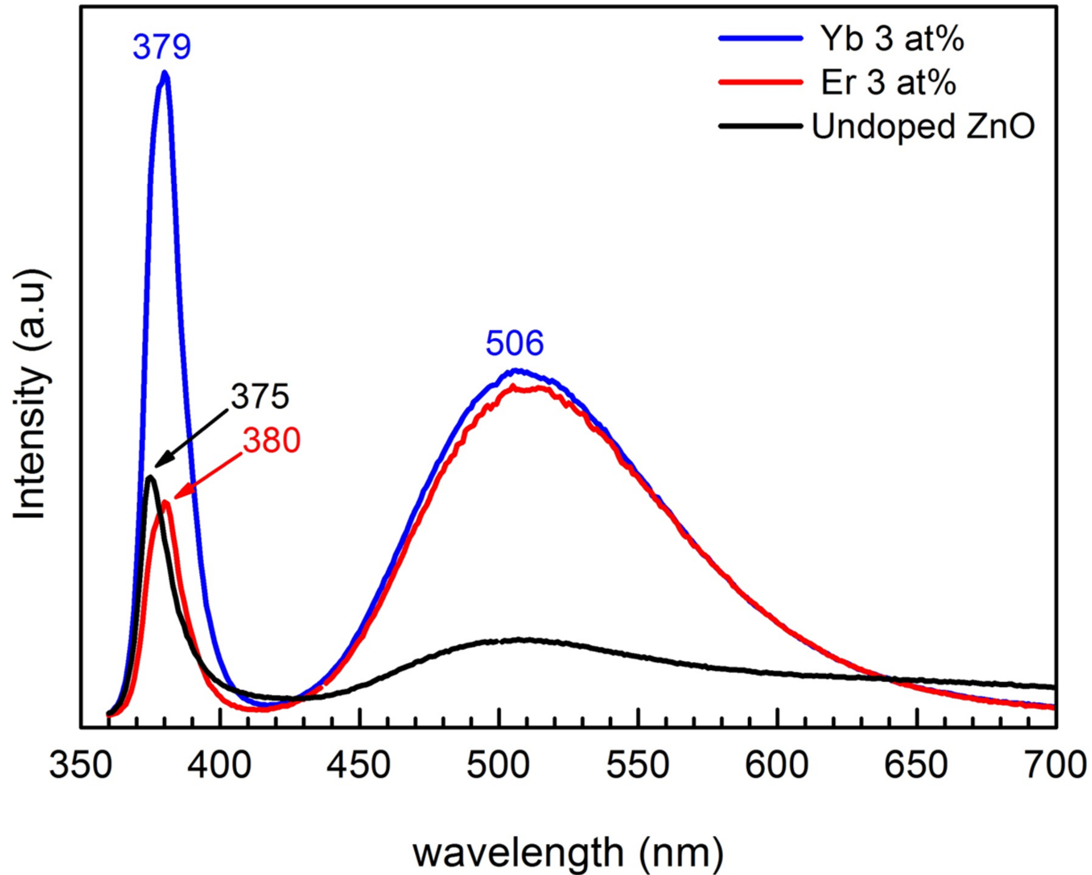


Figure 4.14: (Color online) The PL spectra of undoped, Er-doped and Yb-doped ZnO thin films deposited onto microscope slide substrates.

The PL spectra of the undoped, Er-doped and Yb-doped ZnO thin films excited by a 325 nm laser at room temperature are shown in Figure 4.14. A strong UV emission band centered at 375 nm and a broad green emission band centered at 506 nm were observed in all samples, with the undoped ZnO sample showing weaker green emission. It is clear that the Yb-doped ZnO sample exhibited the highest intensity of ultraviolet emission compared to the undoped and Er doped ZnO samples. The PL spectra provide information about defects in ZnO, UV emission bands are generally attributed to exciton recombination near the band edge, while visible emission bands are assigned to various combinations of deep-level or trap-state emission, due to oxygen vacancies, Zn vacancies and Zn interstitials [122].

### 4.2.4 Temperature dependent *I-V* and *C-V* measurements on Er-doped and Yb-doped ZnO thin film Schottky diodes

Figure 4.15 shows the room temperature *I-V* characteristics of Schottky barrier diodes fabricated on undoped, Er-doped and Yb-doped ZnO thin films. Schottky diodes parameters shown in Tables 4.5 and 4.6 were obtained by performing a linear fit in the forward bias region using thermionic emission Equation 2.5. From Figure 4.15, the rectification increased when the films were doped with the Er and Yb. The Schottky barrier height obtained from the SBD on undoped ZnO thin films of 0.730 eV with a high ideality factor and leakage current compared to the diodes on Er-doped and Yb-doped ZnO thin films at room temperature (see Table 4.5). The diodes on Er-doped and Yb-doped ZnO exhibited a generation-recombination current transport mechanism at low voltages (0 - 0.5 V) causing a kink in the forward bias curve [58]. Above this voltage thermionic emission was the dominant current transport mechanism across the Schottky barrier. At higher voltages, all diodes deviated from the ideal linearity due to high series resistance [12].

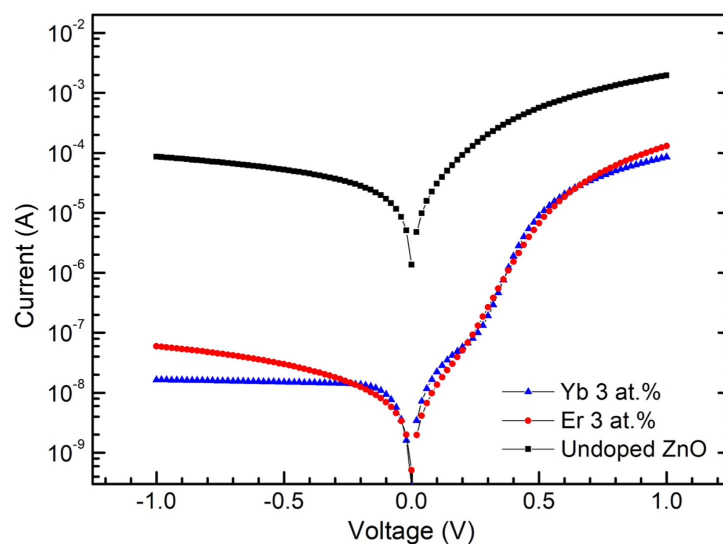


Figure 4.15: (Color online) Room temperature semi-logarithmic plot of *I-V* measurements of Shottky diodes fabricated on undoped, Er-doped and Yb-doped ZnO thin films Schottky diodes.

Figure 4.16 shows the semi-logarithmic plot of *I-V* measurements of Schottky diodes fabricated on Er-doped and Yb-doped ZnO thin films obtained in the temperature range of 50 - 290 K with steps of 40 K.

As shown in Figure 4.16, we can observe a strong dependence of (*I-V*) characteristics on temperature. The rectification was increased with decreasing temperature. The diodes exhibited good rectifying behaviour, especially at 50 K. From Figure 4.16 (a), it can be observed that the diode on Er-doped ZnO thin films deviate from ideality, and thermionic

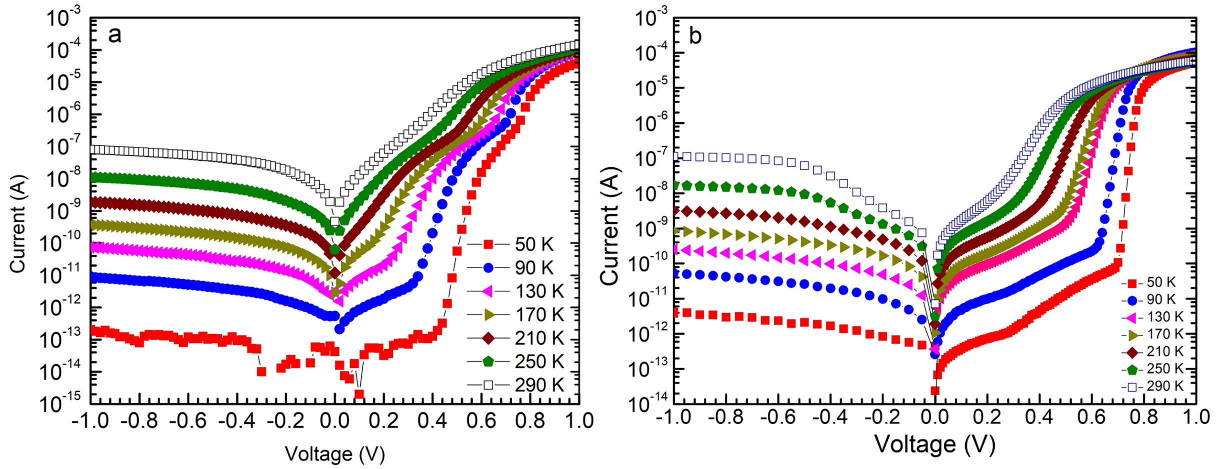


Figure 4.16: (Color online) Semi-logarithmic plot of *I-V* measurements for (a) Pd/Er-doped ZnO/n-Si/AuSb (b) Pd/Yb-doped ZnO/n-Si/AuSb Schottky diodes in the temperature range of 50 - 290 K with steps of 40 K.

Table 4.5: Schottky diodes parameters from *I-V* measurements at room temperature.

| Sample | SBH (eV) | Ideality Factor | Saturation current, $I_s$ (A) | Leakage current (A) at -1 V | Series Resistance(KΩ) |
|---|---|---|---|---|---|
| Undoped ZnO | 0.730 | 2.69 | $5.0\times10^{-6}$ | $9.0\times10^{-5}$ | 0.20 |
| Er | 0.688 | 2.24 | $1.41\times10^{-9}$ | $6.0\times10^{-8}$ | 2.0 |
| Yb | 0.977 | 1.82 | $333\times10^{-12}$ | $1.5\times10^{-8}$ | 3.0 |

emission was not dominant and other current transport mechanisms were found to occur such as generation-recombination current in forward bias at low temperatures (50-170 K) under low voltage (V $<$ 0.4 V). Above 170 K, the thermionic emission was dominant. From Figure 4.16 (b), the diode on Yb-doped ZnO thin films exhibited generation-recombination current at all temperatures under low voltage (V $<$ 0.25 V). In the middle region of the voltage, the thermionic emission was the dominant current transport mechanism at all temperatures. At voltage (0.6 - 0.8 V), the diode on Er-doped ZnO thin films revealed generation-recombination again at temperatures (50 - 210 K), this is not observed in the diode on Yb-doped ZnO thin films. The presence of generation-recombination in both diodes is due to defects from impurities in the ZnO band gap. At high voltage, the diodes deviate from linearity and series resistance was dominant at all temperatures. The leakage current increased with increasing temperature from $10^{-12}$ A at 50 K to $10^{-7}$ A at 290 K at a bias of -1.0 V in both diodes. The reverse bias *I-V* curve at 50 K in a diode on Er-doped ZnO thin films was not a smooth line. This is due to the current being lower than the noise in the system.

Figure 4.17 shows the variations in the Schottky barrier height and ideality factor (from *I-V* data) in the temperature range of 50 - 290 K. SBH increased with increasing temperature

from 0.28 and 0.51 eV at 50 K to 0.66 eV and 0.80 eV at 290 K for Pd/Er-doped ZnO and Pd/Yb-doped ZnO Schottky diodes, respectively. The ideality factor decreased with increasing temperature for both Pd/Er-doped ZnO and Pd/Yb-doped ZnO Schottky diodes. In the diode on Er-doped ZnO thin films (see Figure 4.17 (a)), the ideality factor decreased with increasing temperature but increased again at 290 K. Whereas in the diode on Yb-doped ZnO diode (see Figure 4.17 (b)), the ideality factor decreased sharply from 50 K to 90 K. After that, it decreased gradually up to 170 K. Above 170 K, the ideality factor increased again. The ideal-

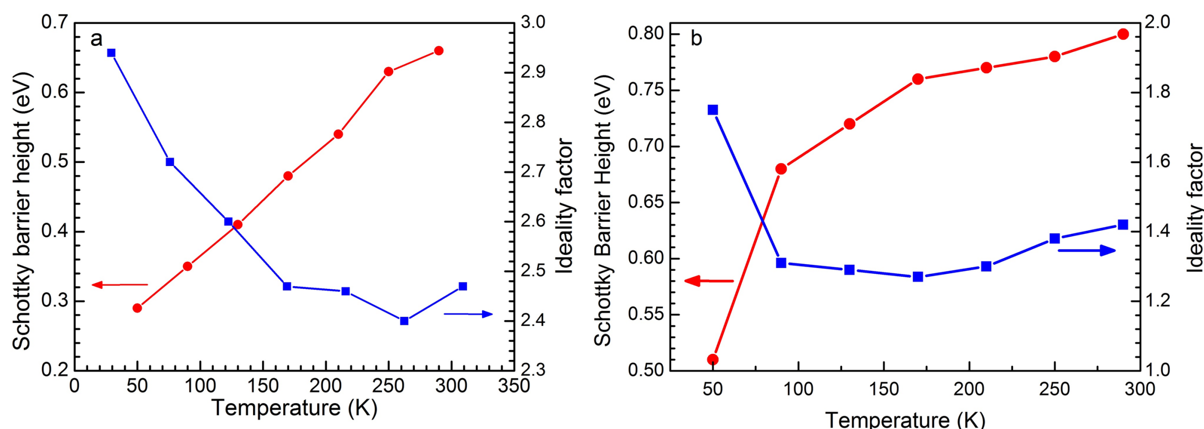


Figure 4.17: (Color online) SBH and ideality factor vs temperature plot from the forward bias $I$-$V$ measurements for (a) Pd/Er-doped ZnO/n-Si/AuSb (b) Pd/Yb-doped ZnO/n-Si/AuSb Schottky diodes in the temperature range of 50 - 290 K in steps of 40 K.

ity factor is greater than unity at all temperatures in both diodes, indicating that the diodes deviated from ideal thermionic emission, this behaviour is attributed to inhomogeneities in the SBH, thermionic field emission current, image force lowering, generation-recombination, effect of the series resistance and interface states caused by contamination and mixture of different phases [138, 139]. The increasing of Schottky barrier height and decreasing of ideality factor with increasing temperature can be explained by SBH inhomogeneity, that SBH consists of inhomogeneous spots with different barrier height. As the current transport across the barrier is a temperature activated process, at low temperatures, the carriers encounter low barriers, so only the low barriers are overcome. At high temperatures, the carriers have sufficient energy to overcome the higher barriers. Consequently, the dominant barrier height will increase with increasing temperature [140]. The diode on Er-doped ZnO thin films exhibited higher ideality factor and lower barrier height at all temperatures compared to the diode on Yb-doped ZnO thin films.

To determine the behaviour of the diodes characteristics such as the Schottky barrier height and carrier concentration ($N_D$) from the $C$-$V$ measurements of Pd/Er-doped ZnO and Pd/Yb-doped ZnO Schottky diodes at different temperatures, the $C$-$V$ measurements in the temperature range of 50 - 290 K at 1 MHz are shown in Figure 4.18. From Figure 4.18 (a) and (c) the

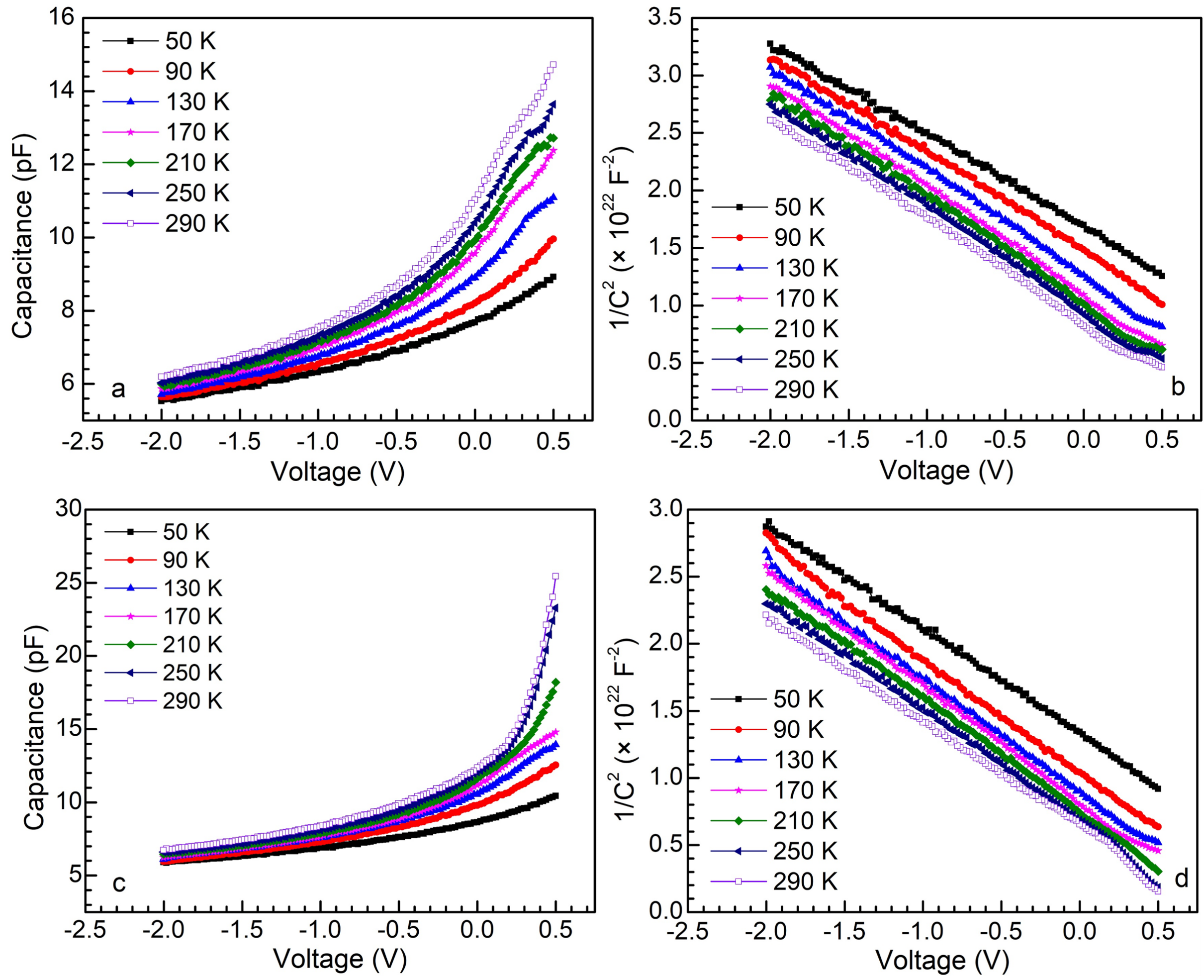


Figure 4.18: (Color online) *C-V* measurements of (a) and (b) Pd/Er-doped ZnO/n-Si/AuSb (c) and (d) Pd/Yb-doped ZnO/n-Si/AuSb Schottky diodes in the temperature range of 50 - 290 K at 1 MHz

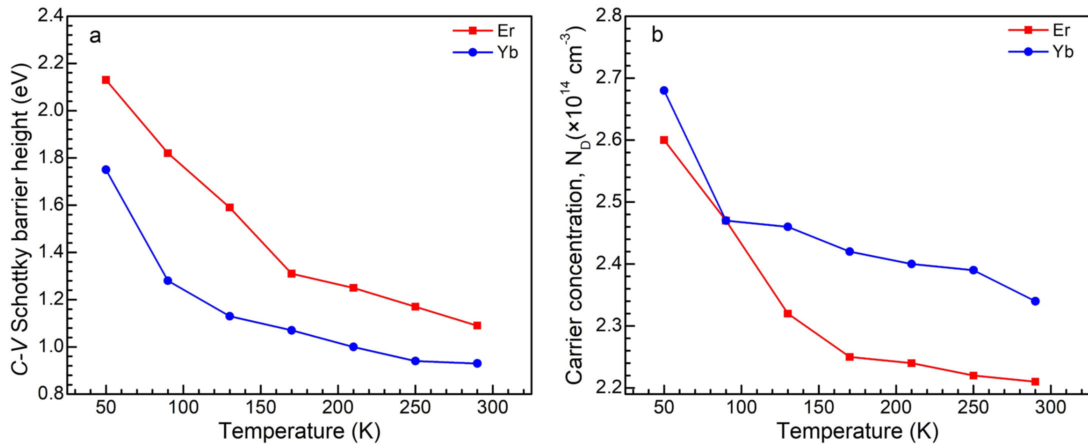


Figure 4.19: (Color online) SBH and carrier concentration vs temperature obtained from *C-V* measurements of (a) Pd/Er-doped ZnO/n-Si/AuSb (b) Pd/Yb-doped ZnO/n-Si/AuSb Schottky diodes in the temperature range of 50 - 290 K.

Table 4.6: The Schottky diodes parameters from *I-V* and *C-V* measurements in the temperature range of 50 - 290 K.

| T (K) | Pd/Er-doped ZnO thin films | | | | Pd/Yb-doped ZnO thin films | | | |
|---|---|---|---|---|---|---|---|---|
| | SBH (eV) | | Ideality | $N_D$ (cm$^{-3}$)($C$-$V$) | SBH (eV) | | Ideality | $N_D$ (cm$^{-3}$)($C$-$V$) |
| | $I$-$V$ | $C$-$V$ | Factor, $n$ | $\times 10^{14}$ | $I$-$V$ | $C$-$V$ | Factor, $n$ | $\times 10^{14}$ |
| 50 | 0.286 | 2.13 | 2.935 | 2.60 | 0.511 | 1.75 | 1.746 | 2.68 |
| 90 | 0.353 | 1.82 | 2.716 | 2.47 | 0.684 | 1.28 | 1.307 | 2.47 |
| 130 | 0.414 | 1.59 | 2.596 | 2.32 | 0.721 | 1.13 | 1.288 | 2.46 |
| 170 | 0.479 | 1.31 | 2.467 | 2.25 | 0.756 | 1.07 | 1.272 | 2.42 |
| 210 | 0.541 | 1.25 | 2.463 | 2.24 | 0.772 | 1.0 | 1.30 | 2.40 |
| 250 | 0.631 | 1.17 | 2.401 | 2.22 | 0.779 | 0.94 | 1.382 | 2.39 |
| 290 | 0.664 | 1.09 | 2.465 | 2.21 | 0.80 | 0.93 | 1.418 | 2.34 |

capacitance increased with increasing temperature from 7.7 pF and 8.5 pF at 50 K to 11 pF and 12 pF at 290 K at a bias of 0 V in diodes on Er-doped and Yb-doped ZnO, respectively. Increasing capacitance can be attributed to either charged defects emitting electrons and thereby contributing to the charge in the depletion region or due to a lowering of the barrier height [141]. The $1/C^2$ vs $V$ depending temperature are shown in Figure 4.18 (b) and (d). The $1/C^2$ - $V$ curves in Figure 4.18 (b) and (d) exhibited straight lines parallel to each other, indicating uniform dopant concentration [141]. The carrier concentration calculated after fitting the straight line in $1/C^2$ - $V$ plots in both diodes, ($N_D$) was $\sim 10^{14}$ cm$^{-3}$. The temperature dependence of SBH and carrier concentration obtained from *C-V* measurements using Equation 2.9 are plotted in Figure 4.19 and summarized in Table 4.6. It could be observed from Figure 4.19 that the SBH and carrier concentration obtained from *C-V* measurements decreased with increasing temperature for both diodes. It is seen in Table 4.6 that the SBH calculated from *C-V* measurements is greater than that obtained from *I-V* measurements in both diodes, this observation is commonly reported in literature and attributed mainly to presence of an interface layer, the effect of the image force, deep impurity levels and inhomogeneity in SBH [66, 142, 143].

### 4.2.5 *DLTS* measurements

The DLTS spectra for Er-doped and Yb-doped ZnO thin films are shown in Figure 4.20. The DLTS spectrum revealed one peak with a level labelled as $E_{0.41}$ in the diodes on Er-doped ZnO thin films, and another peak with a level labelled as $E_{0.54}$ in the diodes on Yb-doped ZnO thin films. The labelling of defects by (E) refers to an electron trap and subscript number is refers to

an activation enthalpy level below the conduction band. The Er-doped ZnO thin films exhibited a high intensity peak, whilst the Yb-doped ZnO thin films showed a broader and low intensity peak. After using Laplace-transform deep-level transient spectroscopy (L-DLTS), both peaks were revealed to consist of only one energy level. Figure 4.21 shows the shift in L-DLTS spectra of the defect in Er-doped and Yb-doped ZnO thin films measured at three temperatures.

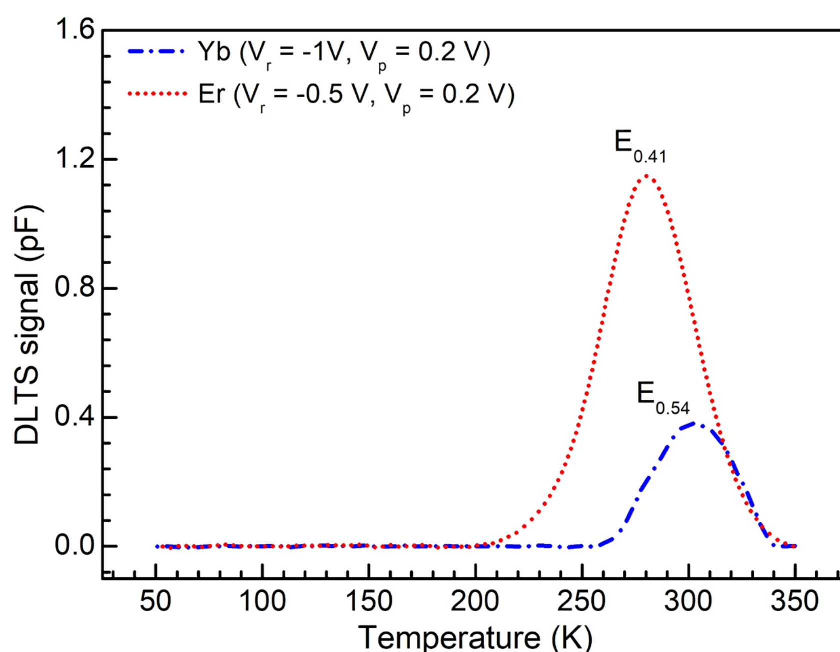


Figure 4.20: (Color online) DLTS spectra obtained from Pd/Er-doped ZnO/n-Si/AuSb and Pd/Yb-doped ZnO/n-Si/AuSb Schottky diodes, recorded at a quiescent reverse bias of $V_r$ = -0.5 and -1 V for the Er-doped and Yb-doped ZnO thin films, respectively. The filling pulse voltage $V_p$ = 0.2 V, filling pulse width of 1 ms and rate window of 80 Hz in the temperature range of 50 - 350 K.

The activation enthalpies and the apparent cross sections of the $E_{0.41}$ and $E_{0.54}$ defects have been extracted from the Arrhenius plots shown in Figure 4.22. The results are shown in Table 4.7. After analysis of the Arrhenius plot, the Er-doped ZnO defect yielded an activation enthalpy of 0.41 eV and apparent capture cross section of $4 \times 10^{-16}$ cm$^2$. The Yb-doped ZnO defect had an activation enthalpy of 0.54 eV and apparent capture cross section of $4 \times 10^{-15}$ cm$^2$. The electronic parameters such as the value of activation enthalpy, locations and apparent cross section for both peaks are different. Thus, it could be concluded that the defects are not the same. Both defects could correspond to the green emission in the PL measurements. The defect $E_{0.41}$ in Er-doped ZnO thin films has been observed in undoped ZnO thin films reported in our previous work in Section 4.1.6 [144]. This defect has been attributed to the oxygen vacancy [119, 120, 145]. The peak in Yb-doped ZnO thin films, Scheffler *et al.* [146] observed the peak with an activation enthalpy of 0.610 eV in n-type ZnO single crystals and Tsiarapas *et al.* [147] observed the peak with the same activation enthalpy

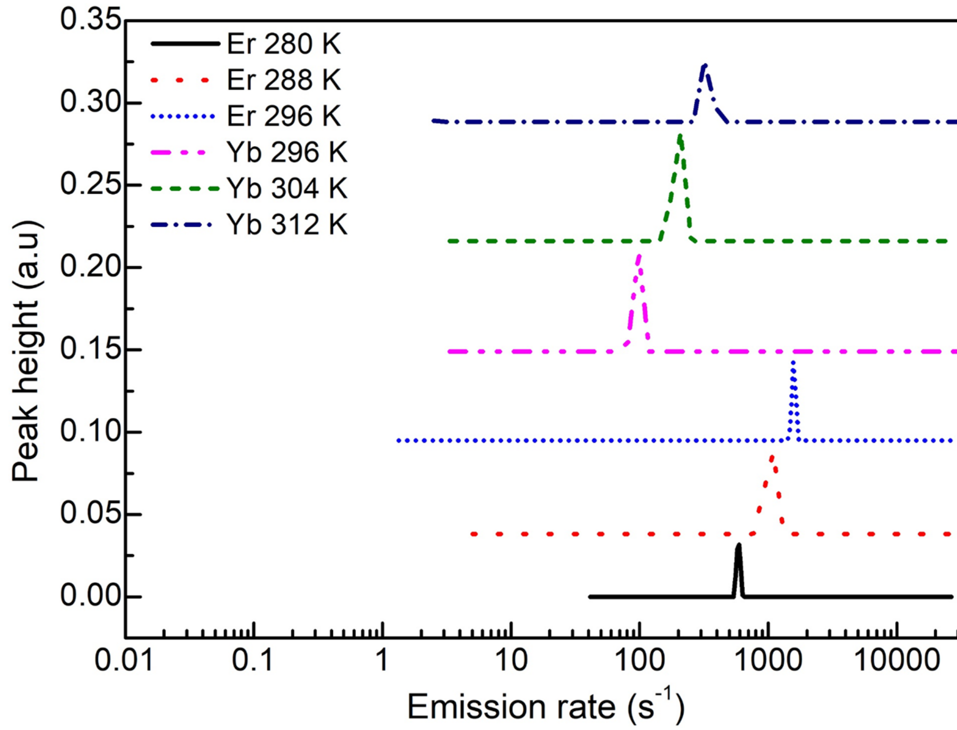


Figure 4.21: (Color online) Laplace DLTS spectra showing the shift of the defect in Er-doped and Yb-doped ZnO thin films at different temperatures.

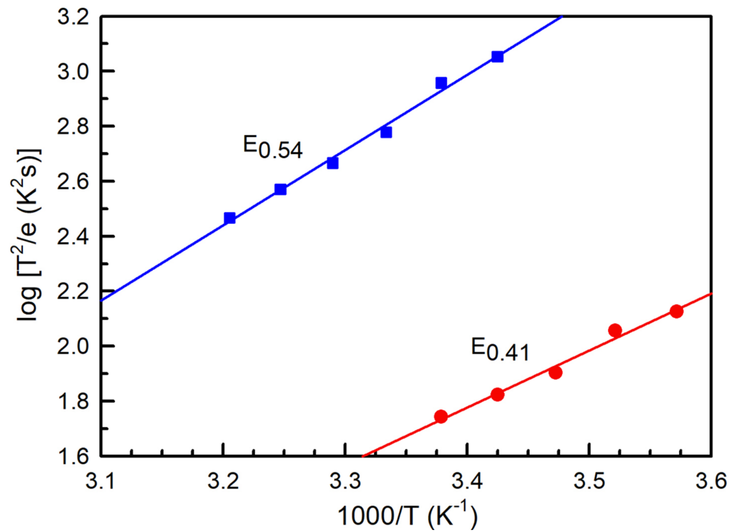


Figure 4.22: (Color online) Arrhenius plots of the defects in Er-doped and Yb-doped ZnO thin films.

in 50 % and 66.6 % $H_2$ incorporated in polycrystalline ZnO thin films and they proposed that this defect is correlated with extended defect.

Table 4.7: The electronic properties of defects in Er-doped and Yb-doped ZnO thin films deposited on the n-Si substrate.

| Sample | Defect label | $E_T(eV)$ | $\sigma_{ap}$ ($cm^2$) |
|---|---|---|---|
| Er-doped ZnO | $E_{0.41}$ | 0.41 | $4 \times 10^{-16}$ |
| Yb-doped ZnO | $E_{0.54}$ | 0.54 | $4 \times 10^{-15}$ |

### 4.2.6 Summary

The surface morphology and structure of undoped, Er-doped and Yb-doped ZnO thin films deposited by the sol-gel technique were investigated. XRD results confirmed that the films had hexagonal wurtzite structure, and this was confirmed by the definite hexagonal shaped grains observed in the SEM images. The crystallite and particle size increased when doping with Er and Yb, Yb-doped ZnO having the largest and undoped ZnO the smallest estimated particle size. The 3 at.% of Yb resulted in $Yb_2O_3$ being present in ZnO films. No evidence of $Er_2O_3$ was found. The electrical properties of Schottky diodes fabricated on Er-doped and Yb-doped ZnO thin films deposited by the sol-gel spin coating technique were investigated using *I-V* and *C-V* techniques in the temperature range of 50 - 290 K. From *I-V* results, the rectification, the leakage current and Schottky barrier height were increased with increasing temperature, and the ideality factor decreased. From *C-V* measurements, the carrier concentration and Schottky barrier height both decreased with increasing temperature. SBH obtained from *C-V* measurements is significant higher than that SBH calculated from *I-V* measurements. The doping of ZnO by Er and Yb caused an increase in the series resistance, but a decrease in the ideality factor of the thin films Shottky barrier diodes. The DLTS and L-DLTS techniques were used to identify the defects in Er-doped ZnO and Yb-doped ZnO thin films. It revealed defect with activation enthalpy of 0.41 eV in the Er-doped ZnO thin films, and another defect with activation enthalpy of 0.54 eV in the Yb-doped ZnO thin films below the minimum of the conduction band.

## 4.3 Structure and optical properties of Er-doped ZnO thin films prepared by sol-gel spin coating, and electrical properties of Schottky diodes prepared thereon

### 4.3.1 Introduction

Semiconductors doped with rare-earth elements have been used for many applications, for example, optoelectronic devices such as visible and infra-red luminescent devices, UV-light emitting diodes and laser diodes [44]. Zinc oxide as semiconductor material is a very promising candidate for electronic devices applications due to its wide band gap (3.4 eV), low cost, low temperature growth, easy formation of nanostructures, resistance to radiation damage and non-toxicity. Further, ZnO has a large exciton binding energy of 60 meV at room temperature which enhances light emission [1].

There are many reports on rare-earth doped ZnO with the aim of improving the structure, optical and electrical properties of ZnO using dopants such as Nd [122], Sm [53], Yb [125] and Eu [148]. Among the rare-earth elements, Er-doped ZnO has attracted much interest and is expected to be one of the most promising materials for ZnO-based optoelectronic devices due to the 1.54 $\mu$m photoemission caused by the Er intra-4f shell transition [149, 150]. Much research has been focused on improving the optical properties of Er-doped ZnO thin films [14, 48, 151, 152].

Photodetectors based on ZnO thin films can be used in various applications such as environmental monitoring, optical communications and flame detection [153]. In our work we study the electrical characteristics of Schottky diodes based on Er-doped ZnO thin films under dark and light conditions.

The electrical and optical properties of ZnO-based devices is affected by the presence of defects, such as oxygen vacancies ($V_o$), zinc vacancies ($V_{Zn}$) and zinc interstitials ($Zn_i$) because these defects form electronic states in the band gap of ZnO [111, 154]. Deep-level transient spectroscopy (DLTS), is an ideal technique for characterizing deep-level defects, as it is very sensitive, easy to analyze and rapid [86]. The technique makes use of the thermal emission properties of the defect, and can be used to determine the activation enthalpy and the apparent cross section of the defect. Several techniques have been used to fabricate high-quality metal-semiconductor contacts such as Schottky and ohmic contacts on ZnO thin films. The quality of these contacts influences the performance of the devices. Schottky diodes fabricated on ZnO thin films have been reported by many researchers in the last years. All these studies

have explored possibilities of developing and fabricating high performance of Schottky diodes based on ZnO thin films for different purposes [53, 65, 66, 129, 155–157] but there is no research available have been studied the defects in Er-doped ZnO thin films grown by sol-gel spin coating using DLTS and L-DLTS techniques.

In this section, we study the effect of the Er-doping at different concentrations on morphology, structure and optical properties of ZnO thin films. We fabricated Schottky diodes on material prepared by this technique. The electrical properties of Schottky diodes based on Er-doped ZnO thin films were studied using *I-V* and *C-V* measurements. The effect of the dark and illumination conditions on Schottky properties based on Er-doped ZnO thin film was investigated. The defects in the Er-doped ZnO thin films Schottky diodes were characterized using DLTS and L-DLTS techniques.

### 4.3.2 Surface and structure of undoped and Er-ZnO thin films

Figure 4.23 shows SEM images of undoped and Er-doped ZnO thin films grown using different concentrations of 0, 2, 4 and 6 at.%. The SEM images show that the grain size of ZnO thin films decreased and the crystallization quality became poor with increasing the Er concentration. This supports the finding of Asikuzun *et al.* [123] who proposed that $Er^{3+}$ ions play a role in inhibiting the growth of the crystallites in the ZnO lattice.

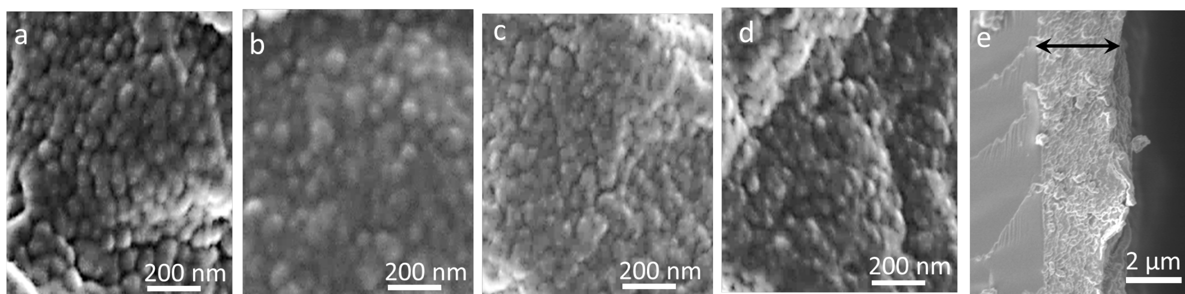


Figure 4.23: SEM images of ZnO thin films with (a) Er 0 at.% (b) Er 2 at.% (c) Er 4 at.% and (d) Er 6 at.% as well as (e) cross-section of Er 6 at.% deposited on microscope slides, dried at 200 °C and annealed at 500 °C in air for 1 hour.

XRD patterns of undoped and Er-doped ZnO thin films (Figure 4.24) revealed that all the diffraction peaks corresponding to the hexagonal wurtzite structure of ZnO with JCPDS card number (76-0704) were present. There was no secondary phase observed related to $Er_2O_3$ or other impurities in any of the Er-doped ZnO samples, which indicates that all the Er ions have successfully incorporated into the ZnO lattice. As can be seen from Figure 4.24, the

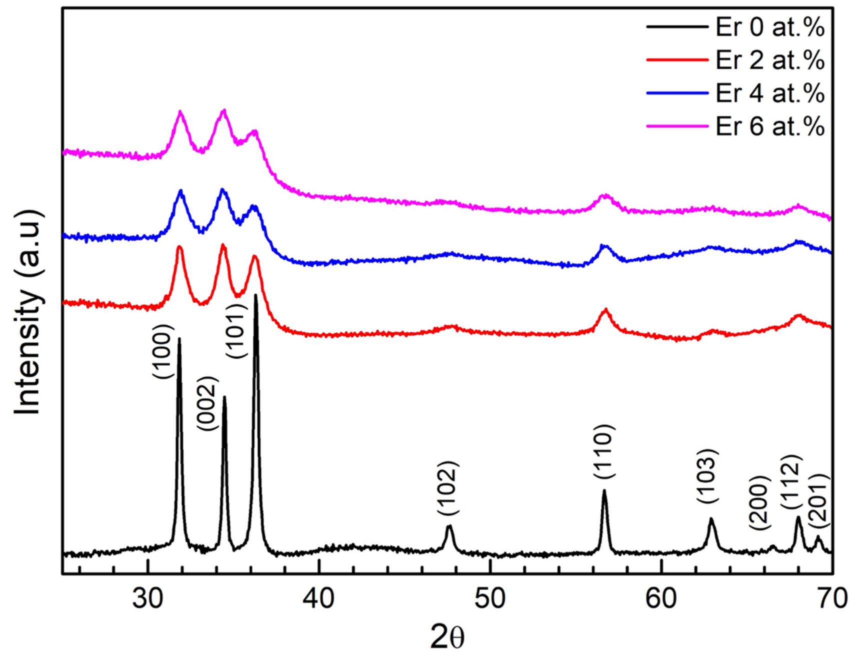


Figure 4.24: (Color online) X-ray diffraction (XRD) patterns of Er-doped ZnO thin films deposited onto microscope slides, dried at 200 °C and annealed at 500 °C in air for 1 hour.

intensity of the peaks decreased significantly with increasing Er concentration. The full-width at half-maximum (FWHM) corresponding to the (002) plane increased with increasing Er concentration and the positions of diffraction peaks at (002) of the Er-doped ZnO shifted slightly to low diffraction angles (see Table 4.8) compared to undoped ZnO. This can be attributed to the large ionic radii mismatch between $Er^{3+}$ (0.89 Å) and $Zn^{2+}$ (0.74 Å). The average crystallite size $D$ of Er-doped ZnO thin films was calculated from Equation 3.2. The plot of calculated crystallite size versus the Er concentration is shown in Figure 4.25. It can be seen that the calculated crystallite size $D$ decreased from 32 nm to 8 nm as the Er concentration increased from 0 at.% to 6 at.%, respectively. The decreasing crystallite size can be attributed to the incorporation of larger $Er^{3+}$ ions (0.89 Å) in the Zn (0.74 Å) sites in the ZnO lattice. The influence of this incorporation can create tensile stress and as a result, restrict the growth of crystals [134]. Jayachandraiah *et al.* [158] reported that the crystallite size decreased with increasing Er concentration. Mao *et al.* [14] also observed a decrease in the crystallite size with increasing Er concentration. Similar results were obtained by other groups [123, 159]. The dislocation density $\delta$ increased with increasing Er concentration and indicates that Er doping leads to more lattice defects [14]. The lattice constants obtained from undoped and Er-doped ZnO thin films are in good agreement with only a slight difference compared to the JCPDS data (a = 3.253 Å, and c = 5.213 Å). The variation in the lattice constants can be attributed to the incorporation of larger $Er^{3+}$ ions in the Zn sites.

Table 4.8: Structural and lattice parameters of undoped and Er-doped ZnO thin films

| Sample Er at.% | FWHM (002) | $2\theta$ (002) | $D$ (nm) (002) | $\delta \times 10^{-4}$ (nm)$^{-2}$ (002) | Lattice constants (Å) $a$(100) | $c$ (002) | c/a | Band gap (eV) |
|---|---|---|---|---|---|---|---|---|
| 0 | 0.254 | 34.469 | 32 | 9.8 | 3.245 | 5.204 | 1.604 | 3.024 |
| 2 | 0.686 | 34.397 | 12 | 69.4 | 3.242 | 5.214 | 1.608 | 3.073 |
| 4 | 0.903 | 34.395 | 09 | 123.5 | 3.238 | 5.215 | 1.610 | 3.091 |
| 6 | 1.016 | 34.377 | 08 | 156.3 | 3.238 | 5.218 | 1.611 | 3.157 |

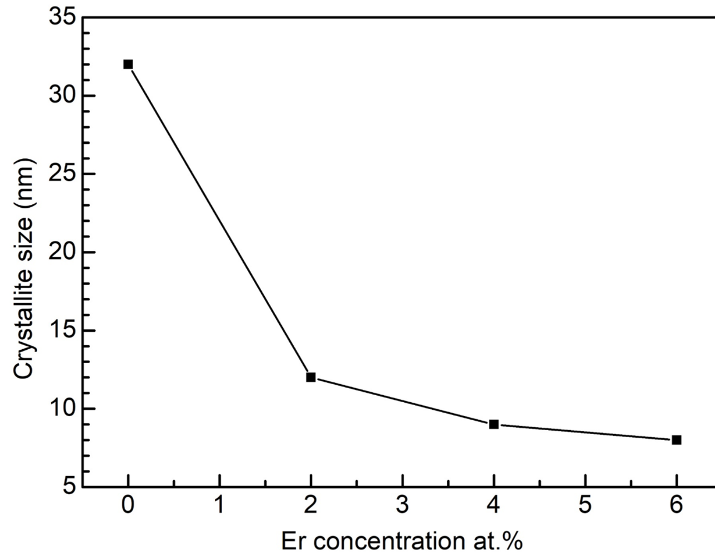


Figure 4.25: The crystallite size versus Er concentrations.

### 4.3.3 Raman spectroscopy and UV-Vis spectroscopy

Raman spectroscopy was employed to study the effect of the Er doping on vibrational properties of ZnO thin films. Figure 4.26 shows Raman spectra of undoped and Er-doped ZnO thin films deposited on the glass substrate at room temperature, excited by the 514.15 nm line of an argon laser. The same peaks were observed in undoped and Er-doped ZnO samples. One high intensity peak located at 436 cm$^{-1}$ corresponds to the $E_2$ (high) mode and confirmed the ZnO wurtzite structure. The $E_2$ (high) mode is associated with the motion of oxygen atoms [30]. The peaks located at 396 cm$^{-1}$ and 408 cm$^{-1}$ correspond to the $A_1$(TO) and $E_1$(TO), respectively. The peaks at 483 cm$^{-1}$ correspond to the 2LA second order feature due to multi-phonon processes [135]. The intensity of the $E_2$ (high) mode decreased and shifted to the high frequency (see Figure 4.26 (b)) after doping by the Er. The shift in the $E_2$ (high) mode can be attributed to incorporation of mismatched $Er^{3+}$ in to Zn antisite, phonon confinement, strain and defects [53, 160].

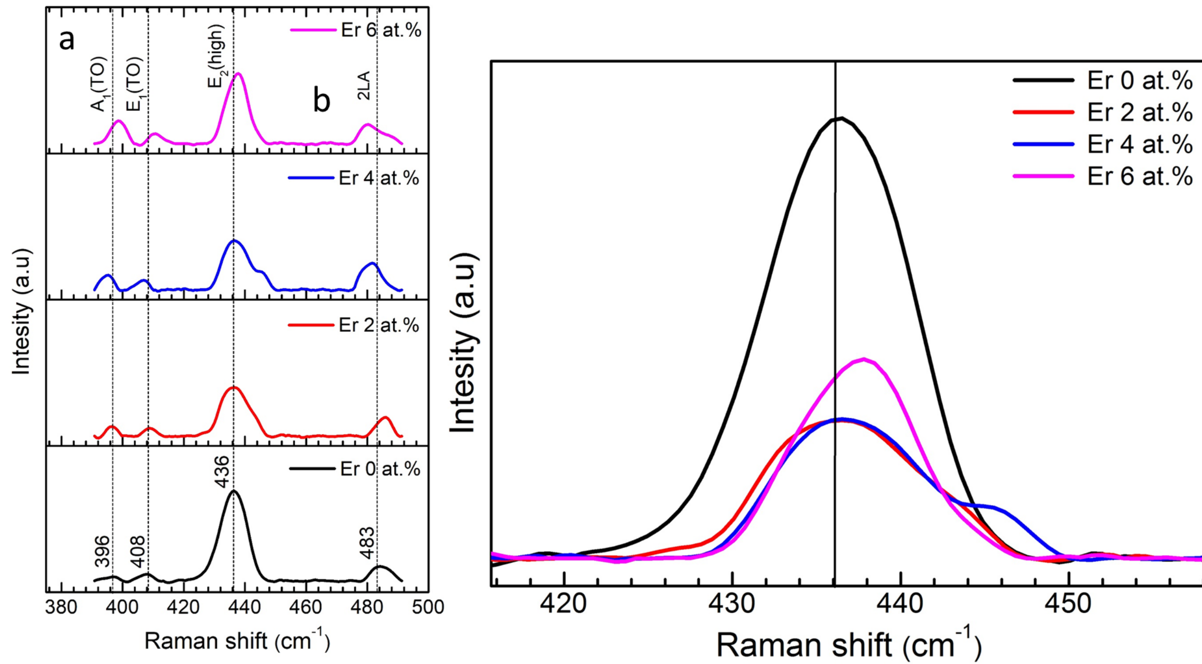


Figure 4.26: (Color online) (a) Raman spectra of the Er-doped ZnO thin films deposited onto microscope slides. dried at 200 °C and annealed at 500 °C in air for 1 hour (b) The shift of the $E_2$ (high) mode.

Figure 4.27 shows the transmittance and absorbance spectra in the wavelength region from 350 - 800 nm of the Er-doped ZnO films at different concentrations. All the films exhibited a good transmittance in the visible region. From Figure 4.27 (a), The transmittance increased after doped by Er 2 at%. Then, decreased in Er 4 at.% and increased again after increasing Er concentration at Er 6 at.%. For example, the transmittance calculated at 550 nm was found to be 65 %, 66 %, 62 % and 69 % for Er 0 at.%, Er 2 at.%, Er 4 at.% and Er 6 at.%, respectively. The decreasing of transmittance at Er 4 at.% may be attributed to existence of defects in the sample. In general, the transmittance of ZnO based thin films can be affected by different conditions such as defects, film thickness, surface roughness, grain size and nano pores [161]. Moreover, all films presented sharp absorption peaks in the ultraviolet region and a shift of the absorption edge occurred to lower wavelengths (blue-shift) with increasing Er concentration. The absorption decreased gradually in the visible and IR region because ZnO has a high transmittance in these wavelengths. This is probably due to the Er in the ZnO. The UV absorbance of Er-doped ZnO thin films is significantly higher than that of undoped ZnO thin films. Inset plot in Figure 4.27 (b) shows Tauc plot used to determine the optical band gap using Equation 3.6. The band gap was obtained at the $h\nu$ axis intercept of an extrapolated linear fit of the graph as 3.024 eV, 3.073 eV, 3.091 eV and 3.157 eV for Er 0 at.%, Er 2 at.%, Er 4 at.% and Er 6 at.%, respectively. The calculated optical band gap are shown in Table 4.8. The plot of optical band gap versus Er concentration is shown in Figure 4.28, and it can be

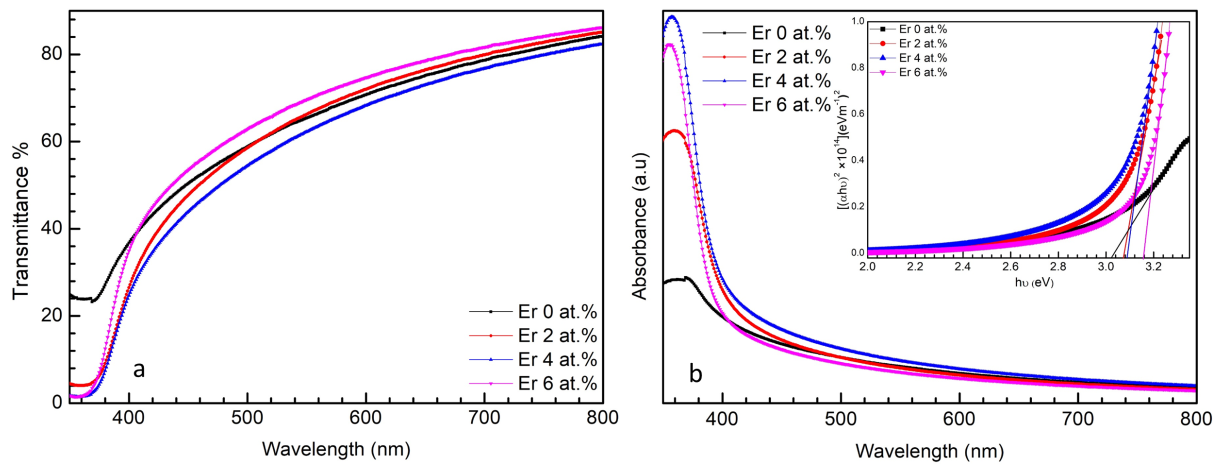


Figure 4.27: (Color online) UV-Vis spectra of (a) transmittance (b) absorbance and corresponding Tauc plot (inset) of the Er-doped ZnO thin films deposited on microscope slides, dried at 200 °C and annealed at 500 °C in air for 1 hour.

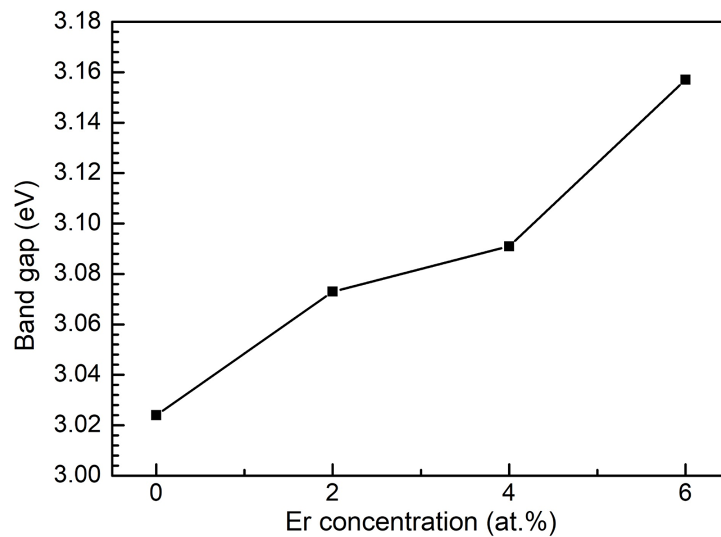


Figure 4.28: Band gap versus Er concentrations.

seen that the optical band gap increased with increasing Er concentration. Similar observation have been reported by the literature for Er-doped ZnO films [124]. The increasing of the band gap could be attributed to the decreases in the particle size of the films (due to quantum confinement effect) as the Er concentration increased [162, 163]. Comparing with the band gap of bulk ZnO (3.4 eV), the obtained optical band gap showed that the band gap of ZnO can be tuned by doping with Er at different concentrations [40].

### 4.3.4 *I-V* measurements

Figure 4.29 shows the room temperature semi-logarithmic plot of typical *I-V* measurements of Schottky barrier diodes fabricated on undoped and Er-doped ZnO thin films. All the diodes

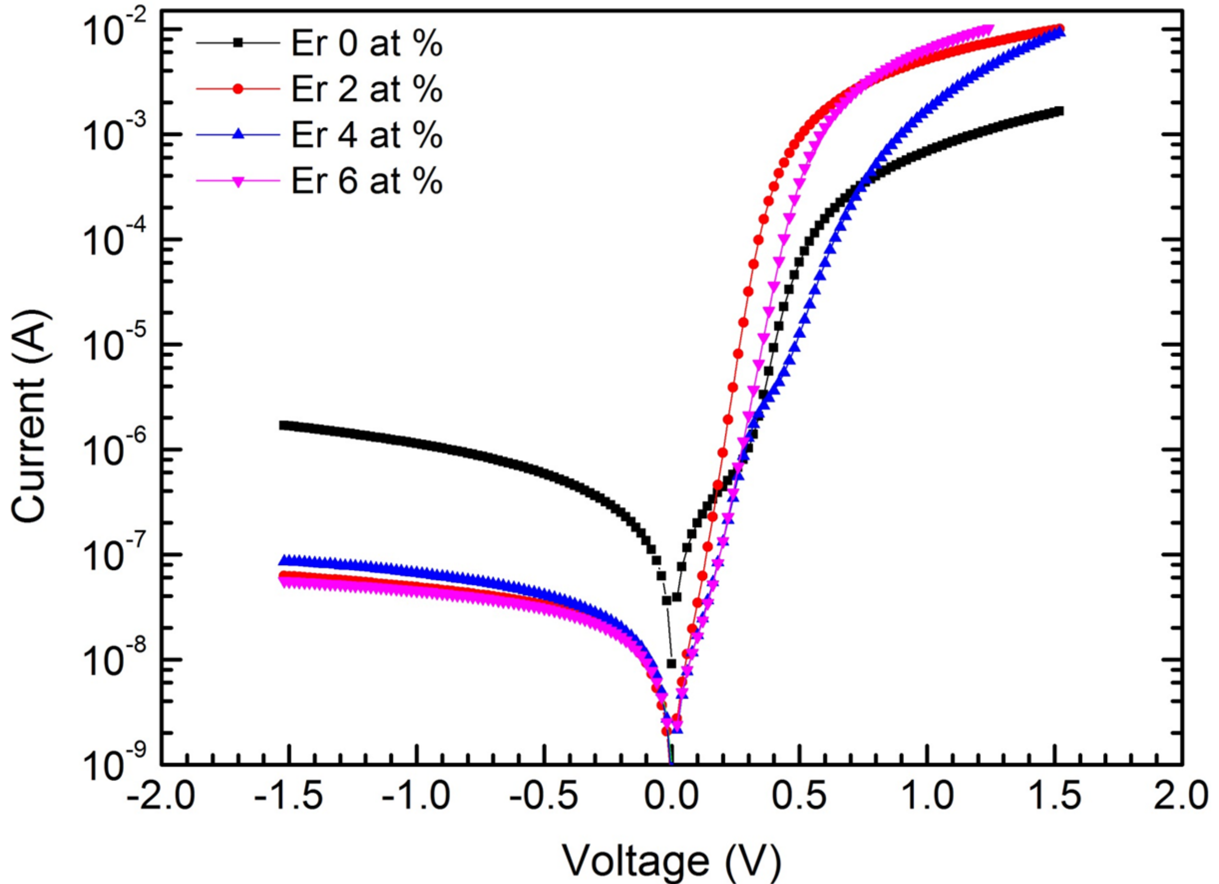


Figure 4.29: (Color online) Room temperature semi-logarithmic *I-V* plot of Pd/Er-doped ZnO/n-Si/AuSb Schottky diodes.

exhibited good rectification, especially the Er-doped ZnO thin films samples. Schottky diodes parameters shown in Tables 4.9 were obtained by performing a linear fit in the forward bias region using the thermionic emission Equation 2.5. From Figure 4.29, the diodes on the Er 0 at.% and Er 4 at.% exhibited generation-recombination current transport mechanism at low voltages (lower than 0.4 V) in the forward bias curve. At a voltage greater than 0.4 V thermionic emission was the dominant current transport mechanism. The generation-recombination was not observed in the diodes on Er 2 at.% and Er 6 at.%, and the pure thermionic emission was the dominant current transport mechanism. As shown in Figure 4.29, at high voltage, the diode's characteristics deviated from linearity due to series resistance [12]. The diodes on the Er-doped ZnO thin film samples exhibited small reverse currents in the same order of magnitude, while that for Er 0 at.% revealed a higher reverse current compared to the diodes on Er-doped ZnO thin films samples.

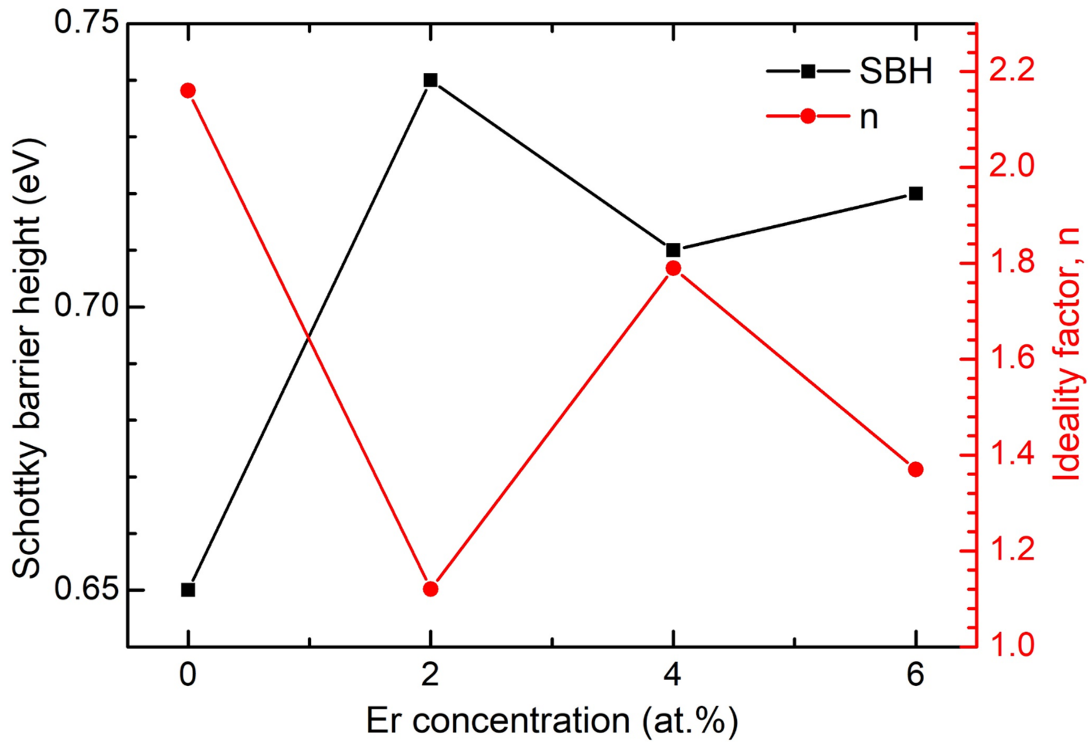


Figure 4.30: (Color online) SBH and ideality factor vs the Er concentration plot from the forward bias *I-V* measurements for Pd/Er-doped ZnO/n-Si/AuSb Schottky diodes.

The variation of SBH and ideality factor values with Er doping level is shown in Figure 4.30. All the diodes on the Er-doped samples had high Schottky barrier heights of 0.74 eV, 0.71 eV and 0.72 eV for the diodes on Er 2 at.%, 4 at.% and Er 6 at.%, respectively. Whereas the diode on the Er 0 at.% revealed lower Schottky barrier height of 0.65 eV. All diodes exhibited an ideality factor significantly higher than unity. Mainly, diode on the Er 0 at.% revealed high ideality factor of 2.16. The ideality factor values greater than unity can be attributed to several factors such as the generation-recombination of electron-hole pairs, inhomogeneities of Schottky barrier height and series resistance [58, 164]. From Figure 4.30 that the value of SBH increased and the ideality factor decreased after doping with the Er.

Figure 4.31 shows the room temperature *I-V* characteristics of Schottky barrier diodes fabricated on undoped and Er-doped ZnO thin films under dark and illuminated. All the diodes exhibited good rectifying behavior in the dark. It is observed from Figure 4.31 that the diodes have strong light sensitivity and photoresponse properties under reverse bias. So the diodes have Schottky photodiode behavior. The behavior of Schottky diodes under illumination condition is explained as follows: When the rectifying Schottky diode is illuminated, the photons with sufficient energy (having a higher energy than the forbidden energy gap) are

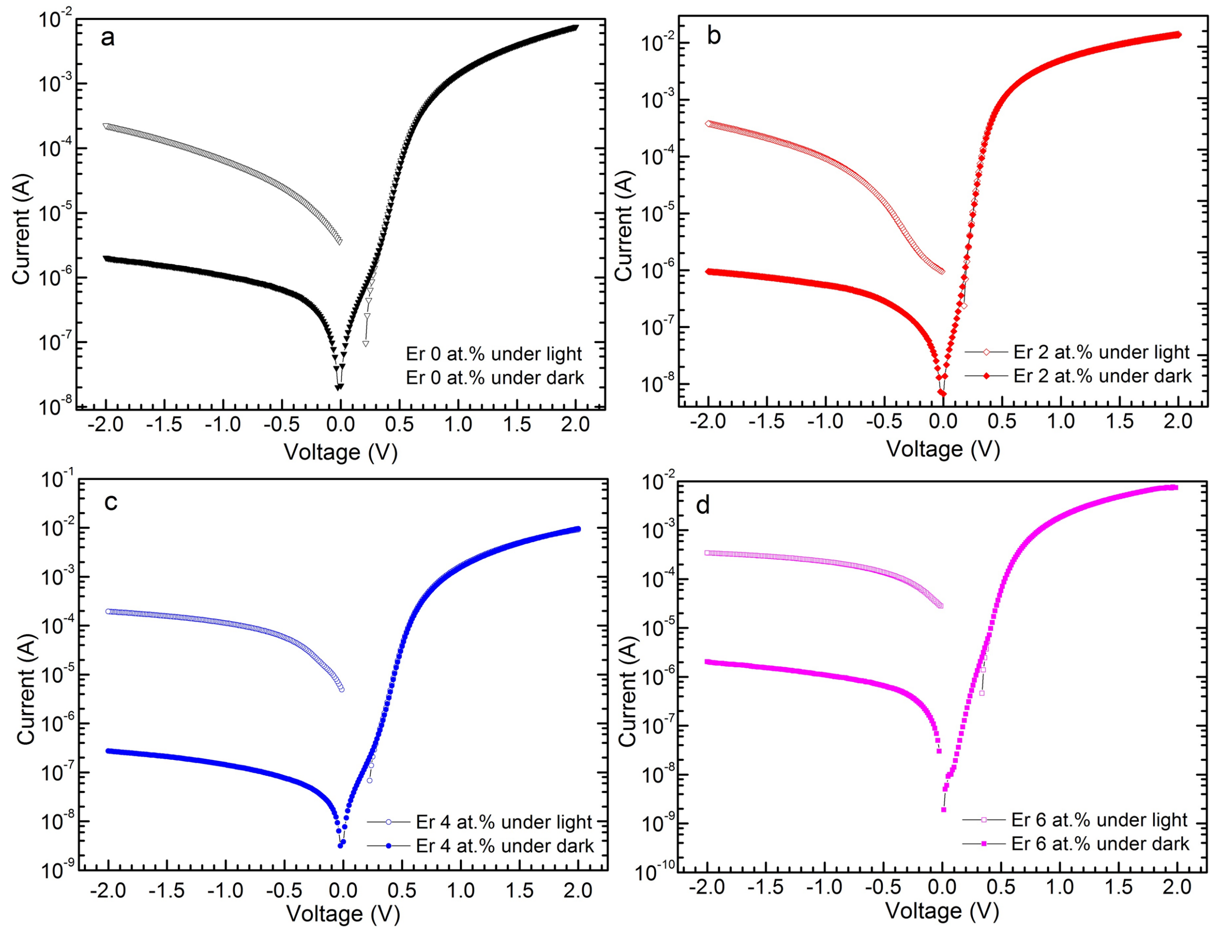


Figure 4.31: (Color online) Room temperature semi-logarithm *I-V* measurements under dark and illumination of Pd/Er-doped ZnO/n-Si/AuSb Schottky diodes.

absorbed and electron-hole pairs are generated in the depletion region [164]. The leakage current in the reverse bias increased when the diodes were exposed to the light. The values of the leakage current in reverse region under the dark and illuminated conditions are illustrated in Table 4.10. The difference between the current under the dark and illuminated conditions in the diodes on Er 2 at.% and Er 4 at.% was higher than of the diodes on Er 0 at.% and Er 6 at.%. The forward bias characteristics seem unaffected by the illumination conditions. Therefore the Er-doped Schottky diodes respond to the visible light and can be used in photodiodes and photovoltaic applications.

The *C-V* technique has been employed to study the diodes characteristics such as the SBH and carrier concentration ($N_D$). Figure 4.32 shows the *C-V* measurements of Pd/Er-doped ZnO/n-Si/AuSb Schottky diodes at room temperature measured at 1 MHz. Under reverse bias, the junction capacitance dominates. However, in the forward bias the diffusion capacitance dominates [165, 166]. From Figure 4.32 (a) the capacitance is affected by the Er doping. The capacitance was lower in the Er-doped material. The diode on Er 4 at.% exhibited the lowest

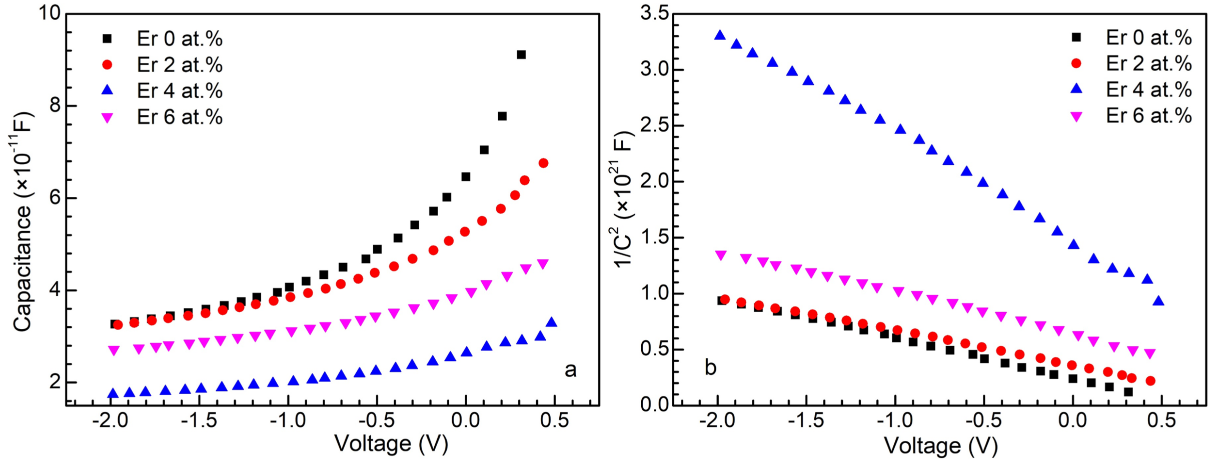


Figure 4.32: (Color online) Room temperature *C*-*V* measurements of Pd/Er-doped ZnO/n-Si/AuSb Schottky diodes at 1 MHz.

Table 4.9: The Schottky diode parameters obtained from *I*-*V* and *C*-*V* measurements at room temperature.

| Sample | SBH (eV) | | Ideality | Saturation current, $I_s$ | Series | $N_D$ | Degree of rectification |
|---|---|---|---|---|---|---|---|
| Er at.% | *I*-*V* | *C*-*V* | Factor | $\times 10^{-9}$ (A) | Resistance($\Omega$) | ($\times 10^{15}$cm$^{-3}$) | (orders of magnitude) |
| 0 | 0.65 | 0.89 | 2.16 | 18.25 | 67 | 1.77 | 3 |
| 2 | 0.74 | 1.0 | 1.12 | 0.872 | 99 | 5.89 | 5 |
| 4 | 0.71 | 1.62 | 1.79 | 1.25 | 43 | 0.75 | 5 |
| 6 | 0.72 | 1.88 | 1.37 | 0.410 | 60 | 1.72 | 5 |

capacitance. In order to obtain the parameters of the diodes from *C*-*V* measurements, the $1/C^2$ vs $V$ is plotted in Figure 4.32 (b). The carrier concentration and the SBH can be obtained from *C*-*V* measurements using Equation 2.9. After fitting the straight line in Figure 4.32 (b) a carrier concentration ($N_D$) of $\sim 10^{15}$ cm$^{-3}$ was obtained. SBH and carrier concentration obtained from *C*-*V* measurements were plotted versus Er concentration in Figure 4.33 and summarized in Table 4.9. It could be observed that the carrier concentration increased as the Er concentration increased up to 2 at.%. At 4 at.% Er the capacitance decreased sharply, then it increased again at 6 at.%. The diodes on Er 4 at.% revealed lower carrier concentration of 0.75 $\times 10^{15}$cm$^{-3}$. It is seen in Table 4.9 that the SBH calculated from *C*-*V* measurements is greater than that obtained from *I*-*V* measurements in all diodes, this observation is commonly reported in the literature and attributed to the presence of an interface layer, inhomogeneity in SBH and the effect of the image force [66, 142, 143].

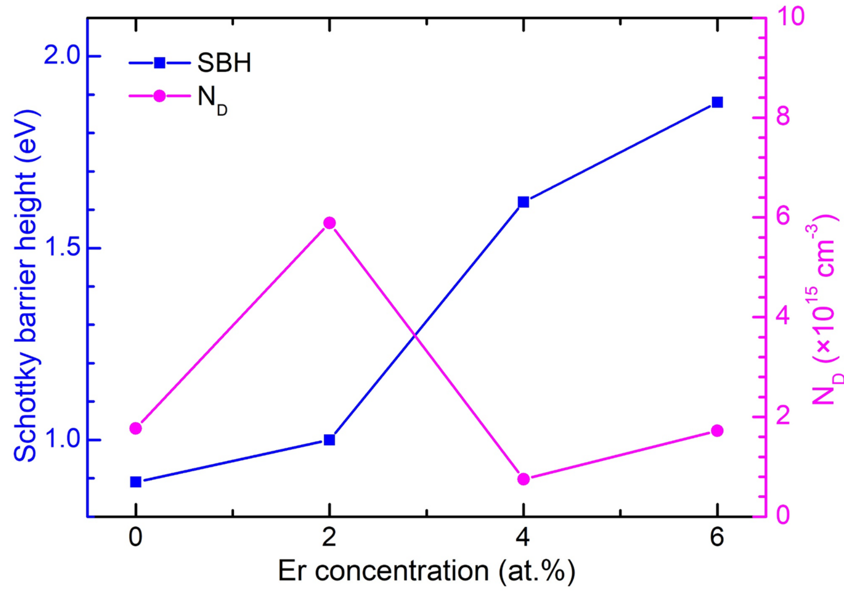


Figure 4.33: (Color online) SBH and carrier concentration vs the Er concentration obtained from *C-V* measurements of Pd/Er-doped ZnO/n-Si/AuSb Schottky diodes.

Table 4.10: The Schottky diode leakage current under reverse bias at -2 V under the dark and illumination from *I-V* measurements.

| Sample | leakage current (A) | |
|---|---|---|
| Er at.% | under light | under dark |
| 0 | $2.23\times10^{-4}$ | $2.01\times10^{-6}$ |
| 2 | $3.81\times10^{-4}$ | $9.46\times10^{-7}$ |
| 4 | $1.94\times10^{-4}$ | $2.72\times10^{-7}$ |
| 6 | $3.40\times10^{-4}$ | $2.10\times10^{-6}$ |

### 4.3.5 DLTS measurements

The DLTS spectra for Er-doped ZnO thin films are shown in Figure 4.34. The DLTS spectra obtained from Pd/Er-doped ZnO/n-Si/AuSb Schottky diodes, recorded at a quiescent reverse bias $V_r$ = -1 V, filling pulse voltage $V_p$ = 0.2 V for the Er 0 and 2 at.%, and 0.5 V for the Er 4 and 6 at.%, filling pulse width of 1 ms and rate window of 80 Hz in the temperature range of 50 - 350 K. The DLTS spectrum revealed one peak in the diodes on the Er 2 at.% and 6 at.%, and two peaks on the diodes on Er 0 at.% and 4 at.%. A dominant peak with labelled as $E_4$ observed in all diodes except for the diode on the Er 6 at.%. After using Laplace-transform deep-level transient spectroscopy (L-DLTS), the $E_4$ peak was revealed to consist of only one energy level in both diodes on the Er 0 at.% and 2 at.%, and three energy levels in the diode on the Er 4 at.%. The defect labelled as $E_5$ observed in all diodes except for the diode on the Er 2 at.%. It was found that the $E_5$ consists of only one energy level in

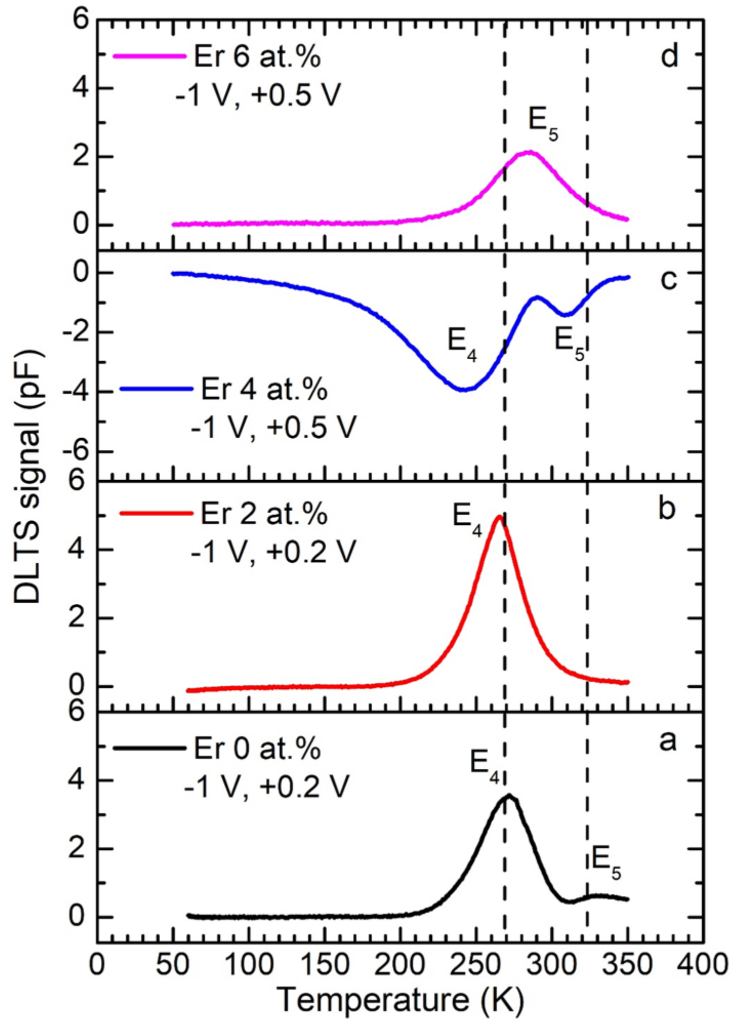


Figure 4.34: (Color online) DLTS spectra obtained from Pd/Er-doped ZnO/n-Si/AuSb Schottky diodes, recorded at a quiescent reverse bias $V_r$ = -1 V, filling pulse voltage $V_p$ = 0.2 V for Er 0 and 2 at.%, and 0.5 V for Er 4 and 6 at.%, filling pulse width of 1 ms and rate window of 80 Hz in the temperature range of 50 - 350 K.

the diode on the Er 0 at.%, and two energy levels in the diodes on the Er 4 at.% and 6 at.%. The activation enthalpies and the apparent cross sections of the $E_4$ and $E_5$ defects have been extracted from the Arrhenius plots shown in Figure 4.35. The results are shown in Table 4.11. After analysis of the Arrhenius plot, the $E_4$ defect yielded an activation enthalpy of 0.44 eV and 0.37 eV and apparent capture cross sections of $8 \times 10^{-16}$ cm$^2$ and $3 \times 10^{-17}$ cm$^2$ in the diodes on the Er 0 at.% and 2 at.%, respectively. Whereas the $E_4$ defect revealed three energy levels in the diode on the Er 4 at.% with an activation enthalpy of 0.33 eV, 0.42 eV and 0.45 eV and apparent capture cross section of $2 \times 10^{-17}$ cm$^2$, $6 \times 10^{-16}$ cm$^2$ and $1.4 \times 10^{-14}$ cm$^2$, respectively. A similar peak ($E_4$) was observed in undoped ZnO thin films and reported in our previous work in Section 4.1.6 [144]. The $E_4$ defect has been attributed to the oxygen vacancy [119, 120, 145]. The $E_5$ defect exhibited an activation enthalpy of 0.75 eV and apparent capture cross sections of $6 \times 10^{-12}$ cm$^2$ in the diodes on the Er 0 at.%. Whilst

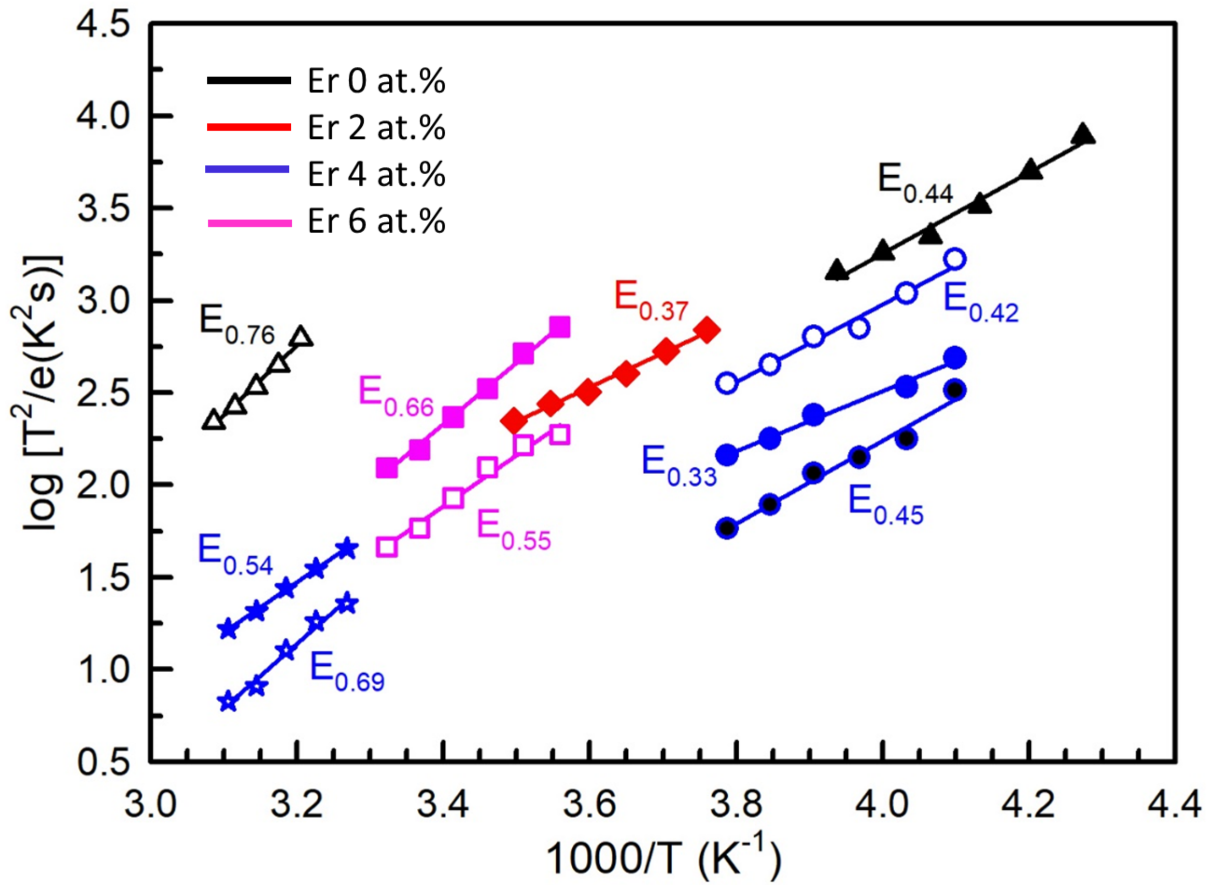


Figure 4.35: (Color online) Arrhenius plots of the defects in Pd/Er-doped ZnO/n-Si/AuSb Schottky diodes.

the $E_5$ defect consists of two energy levels in the diode on the Er 4 at.% with an activation enthalpy of 0.54 eV and 0.69 eV and apparent capture cross sections of $3 \times 10^{-14}$ $cm^2$ and $2 \times 10^{-11}$ $cm^2$, respectively. In the diode on the Er 6 at.%, the $E_5$ defect revealed two energy levels with an activation enthalpy of 0.55 eV and 0.66 eV and apparent capture cross sections of $6 \times 10^{-14}$ $cm^2$ and $2 \times 10^{-12}$ $cm^2$, respectively. Scheffler *et al*. [146] observed the peak with an activation enthalpy of 0.60 eV in n-type ZnO single crystals, and Tsiarapas *et al*. [147] observed the peak with the same activation enthalpy in 50 % and 66.6 % $H_2$ incorporated in polycrystalline ZnO thin films and they proposed that this defect is an extended defect. The Er-doped ZnO thin film's peaks shifted to the lower temperatures compared to the undoped ZnO peak. The shift could be attributed to the effect of the Er doping. The diode on Er 4 at.% exhibited the negative signal in DLTS spectra, and this not observed in other samples.

Table 4.11: The electronic properties of defects in Er-doped ZnO and Yb-doped ZnO thin films deposited on the n-Si substrate.

| Sample Er at.% | Defect label | $E_T(eV)$ | $\sigma_{ap}$ ($cm^2$) |
|---|---|---|---|
| 0 | $E_4$ | 0.44 | $8 \times 10^{-16}$ |
| | $E_5$ | 0.76 | $6 \times 10^{-12}$ |
| 2 | $E_4$ | 0.37 | $3 \times 10^{-17}$ |
| 4 | $E_4$ | 0.42 | $6 \times 10^{-16}$ |
| | | 0.33 | $2 \times 10^{-17}$ |
| | | 0.45 | $1.4 \times 10^{-14}$ |
| | $E_5$ | 0.54 | $3 \times 10^{-14}$ |
| | | 0.69 | $2 \times 10^{-11}$ |
| 6 | $E_5$ | 0.55 | $6 \times 10^{-14}$ |
| | | 0.66 | $2 \times 10^{-12}$ |

### 4.3.6 Summary

Er-doped ZnO thin films at different concentrations of Er were successfully prepared by the sol-gel spin coating technique. The surface morphology and structure of Er-doped ZnO were investigated. From the XRD results, the films had a hexagonal wurtzite structure, which was confirmed by Raman spectroscopy. The crystallite size decreased with increasing Er concentration. The optical properties were studied using UV-Vis spectroscopy and the optical band gap was found to increase with increasing the Er concentration. Schottky diodes fabricated on undoped and Er-doped ZnO thin films deposited by the sol-gel spin coating revealed good rectification behavior. Schottky barrier height was increased after Er doping. However, the ideality factor decreased. The effect of the dark and illumination conditions on Schottky barrier diode characteristics showed a sensitivity to light under reverse bias conditions. Furthermore, the diodes exhibited a strong response to the illumination, so that, these diodes can be used as photodiode or photosensor applications. The DLTS spectra revealed one peak in the diodes on the Er 2 at.% ($E_4$) and Er 6 at.% ($E_5$), and two peaks ($E_4$ and $E_5$) on the diodes on the Er 0 at.% and 4 at.%.

## 4.4 Structure and optical properties of (Er, Yb) co-doped ZnO thin films prepared by sol-gel spin coating, and electrical properties of Schottky diodes prepared thereon

### 4.4.1 Introduction

ZnO is a an ideal host lattice for doping with rare-earth elements such as Er and Yb, due to its wide, direct band gap of approximately 3.4 eV and large exciton binding energy of 60 meV at room temperature [1]. ZnO may be doped with rare-earth elements to tailor its optical, electrical and magnetic properties by altering its electronic structure. Thus it can be used for different applications such as optoelectronic devices, spintronic and photocatalytic applications [45]. Several researchers have reported on rare-earth (Er, Yb) co-doped ZnO for different uses [48, 167–169].

To study the electrical behaviour of (Er, Yb) co-doped ZnO thin films, metal-semiconductor contacts (M-S) have been used to produce devices such as Schottky barrier diodes. Schottky diodes fabricated on ZnO thin films reported by many researchers in the last years. All these studies have explored possibilities of developing and fabricating high performance Schottky diodes based on ZnO thin films for different purposes [65, 66, 129, 155, 156] but few study fabricated Schottky diodes on rare-earth doped ZnO [53, 144, 157, 170].

In this section, we fabricated and characterized (Er, Yb) co-doped ZnO thin film Schottky diodes fabricated using the sol-gel spin coating technique. We studied the electrical properties of the diodes using current-voltage (*I-V*) and capacitance-voltage (*C-V*) measurements. Investigation the effect of (Er, Yb) doping on surface morphology, structural and optical properties of the thin films were done using SEM, XRD and UV-vis spectroscopy. The defects in (Er, Yb) 2 at.% co-doped ZnO thin films were studied using DLTS and L-DLTS. Er and Yb in a 1 : 1 ratio was used to a total of 2 at.%, 4 at.% and 6 at.% doping was investigated.

### 4.4.2 Surface and structure of undoped and (Er, Yb) co-doped ZnO thin films

Figure 4.36 shows SEM images of undoped and (Er,Yb) co-doped ZnO thin films at different concentrations and annealed at 500 °C in air for 1 hour. The images show thin films with average crystallite size ranging from 26 nm (undoped) to 7 nm (6 at.%). The smaller crystallite size in the co-doped thin films could be attributed to the formation of rare-earth-O-Zn in the

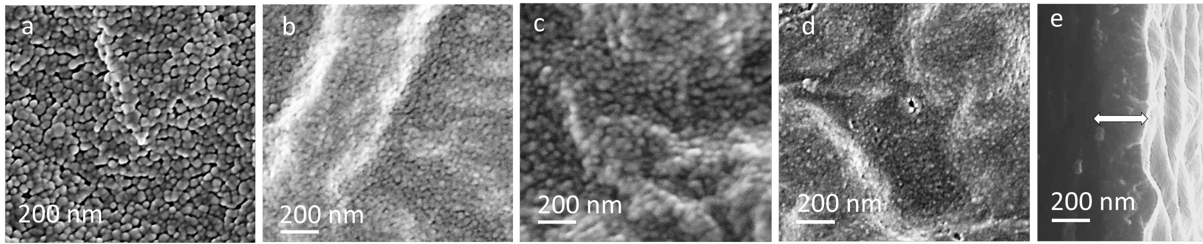


Figure 4.36: SEM images of (a) 0 at.% (b) 2 at.% (c) 4 at.% and (d) 6 at.% as well as (e) cross section of (Er, Yb) co-doped 6 at.% deposited on microscope slides, dried at 200 °C and annealed at 500 °C in air for 1 hour.

ZnO lattice. This formation plays a role in restraining the growth of the crystallites in the ZnO lattice [9, 123]. A cross section of a thin film with (Er, Yb) 6 at.% doping is shown in Figure 4.36 (e). The thickness of the film as measured from the cross section is 700 nm.

The XRD patterns of undoped and (Er, Yb) co-doped ZnO thin films are shown in Figure 4.37. The diffraction peaks observed in undoped and (Er, Yb) co-doped samples correspond to the hexagonal wurtzite structure of ZnO with JCPDS card number (76-0704). No secondary phase related to $Er_2O_3$ or $Yb_2O_3$ in any of the (Er, Yb) co-doped ZnO samples was detected, suggesting that all $Er^{3+}$ and $Yb^{3+}$ ions were successfully incorporated into the ZnO lattice. As seen in Figure 4.37, undoped ZnO thin films exhibited higher intensity diffraction peaks compared to (Er, Yb) co-doped samples. The (Er, Yb) co-doped samples revealed broad peaks with intensity decreasing as doping concentration increased. The full-width at half-maximum (FWHM) corresponding to the (002) plane increased as a result of increasing Er and Yb concentration.

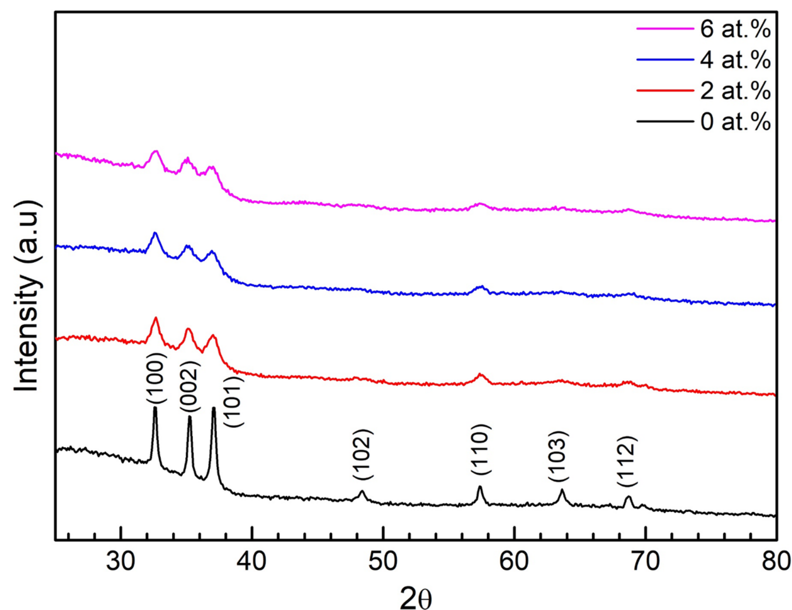


Figure 4.37: (Color online) The X-ray diffraction (XRD) patterns of Er and Yb co-doped ZnO thin films deposited onto microscope slides, dried at 200 °C and annealed at 500 °C in air for 1 hour.

Table 4.12: Structural, lattice parameters and optical band gap of Er and Yb co-doped ZnO thin films

| Sample | FWHM | $2\theta$ | $D$ (nm) | $\delta \times 10^{-3}$ (nm)$^{-2}$ | Lattice constants (Å) | | c/a | Band gap (eV) |
|---|---|---|---|---|---|---|---|---|
| (Er, Yb) at.% | (002) | (002) | (002) | (002) | $a$(100) | $c$ (002) | | |
| 0 | 0.336 | 35.243 | 26 | 1.5 | 3.171 | 5.093 | 1.606 | 3.22 |
| 2 | 0.749 | 35.150 | 12 | 6.9 | 3.168 | 5.106 | 1.612 | 3.15 |
| 4 | 0.828 | 35.074 | 10 | 10 | 3.172 | 5.117 | 1.613 | 3.19 |
| 6 | 1.302 | 35.075 | 07 | 20.4 | 3.169 | 5.117 | 1.615 | 3.20 |

The diffraction peaks at (002) of the (Er, Yb) co-doped ZnO shifted slightly towards lower diffraction angles (see Table 4.12) compared to undoped ZnO. The shift in the diffraction peaks is due to substitution of the large ionic radii $Er^{3+}$ (0.89 Å) and $Yb^{3+}$ (0.87 Å) ions in the place of $Zn^{2+}$ (0.74 Å) [171]. The average crystallite size $D$ of (Er, Yb) co-doped ZnO thin films was calculated from Equation 3.2 [172]. The plot of calculated crystallite size versus (Er, Yb) concentration is shown in Figure 4.38. It can be seen from Figure 4.38 that the calculated crystallite size $D$ decreased from 26 nm to 7 nm as the (Er, Yb) concentration increased from 0 at.% to 6 at.%. The incorporation of large ionic radii $Er^{3+}$ and $Yb^{3+}$ ions in ZnO lattice caused an increasing of the lattice constance ($c$) as the (Er, Yb) concentration increased. Also the differences in ionic radii cause lattice distortions [51].

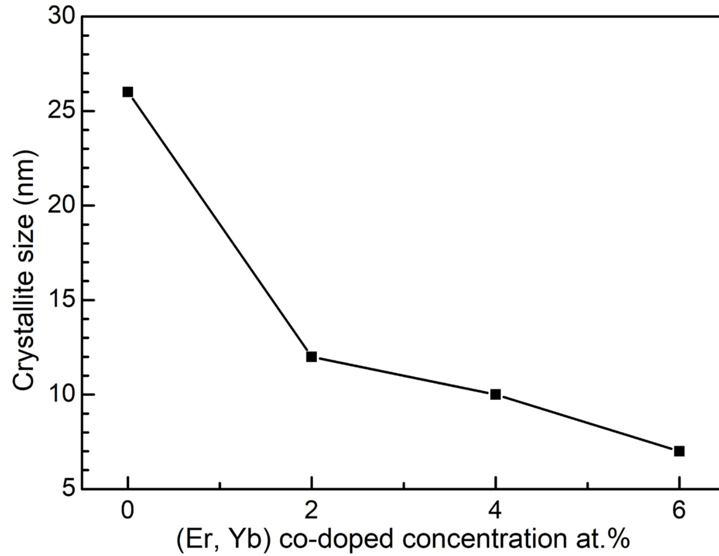


Figure 4.38: The crystallite size versus (Er, Yb) concentrations.

### 4.4.3 UV-Vis spectroscopy

Figure 4.39 shows the transmittance and absorbance spectra at room temperature of (Er, Yb) co-doped ZnO films at different concentrations. Undoped ZnO thin films exhibited higher average transmittance of 65.6 % (the average transmittance calculated at the wavelength of 550 nm). Whereas the co-doped thin films had an average transmittance of 52.4 %, 61.7 % and 62.3 % for (Er, Yb) co-doped 2 at.%, 4 at.% and 6 at.%, respectively at a wavelength of 550 nm. The transmittance of (Er, Yb) co-doped 2 at.% decreased, however, further increase in the Er and Yb concentration caused the transmittance to increase again. The decrease of transmittance could be attributed to scattering and reflection of the light due to surface roughness, nano pores and defects [161, 173]. Figure 4.39 (b) shows the absorbance spectra of undoped and (Er, Yb) co-doped ZnO thin films, and revealed sharp absorption peaks in the UV region. Undoped ZnO thin films showed an absorption peak at 362 nm and the absorption peaks shifted towards the lower wavelengths after co-doping by Er and Yb. The absorption peak can be attributed to the electronic transition from the valence band (VB) to the conduction band (CB) of ZnO thin films [167, 174]. The absorption decreased gradually in the visible and IR regions. The inset plot in Figure 4.39 (b) shows Tauc plot used to calculate the optical band gap using Equation 3.6 [105]. The band gap was obtained at the $h\nu$ axis intercept of an extrapolated linear fit of the graph as 3.22 eV, 3.15 eV, 3.19 eV and 3.20 eV for (Er, Yb) co-doped 0 at.%, 2 at.%, 4 at.% and 6 at.%, respectively. The optical band gap decreased after co-doping by (Er, Yb) when compared to undoped ZnO thin films (see Table 4.12). Similar observation have been reported in literature for (Er, Yb) co-doped ZnO nanoparticles [167].

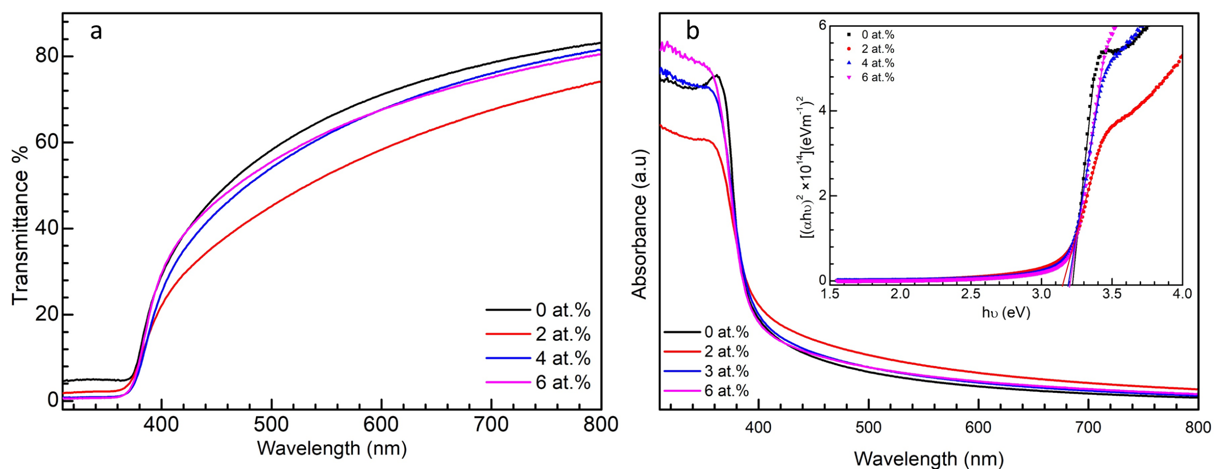


Figure 4.39: (Color online) UV-Vis spectra of (a) transmittance (b) absorbance and corresponding Tauc plot (inset) of (Er, Yb) co-doped ZnO thin films deposited on microscope slides, dried at 200 °C and annealed at 500 °C in air for 1 hour.

### 4.4.4 *I-V* and *C-V* measurements

Figure 4.40 shows the room temperature semi-logarithmic plot of typical *I-V* measurements on Schottky barrier diodes fabricated on undoped and (Er, Yb) co-doped ZnO thin films. The diodes on the (Er, Yb) co-doped ZnO thin films exhibited good rectification. Schottky diodes parameters shown in Tables 4.13 were obtained by performing a linear fit on the linear section of the forward bias region and using the thermionic emission Equation 2.5. The diodes on

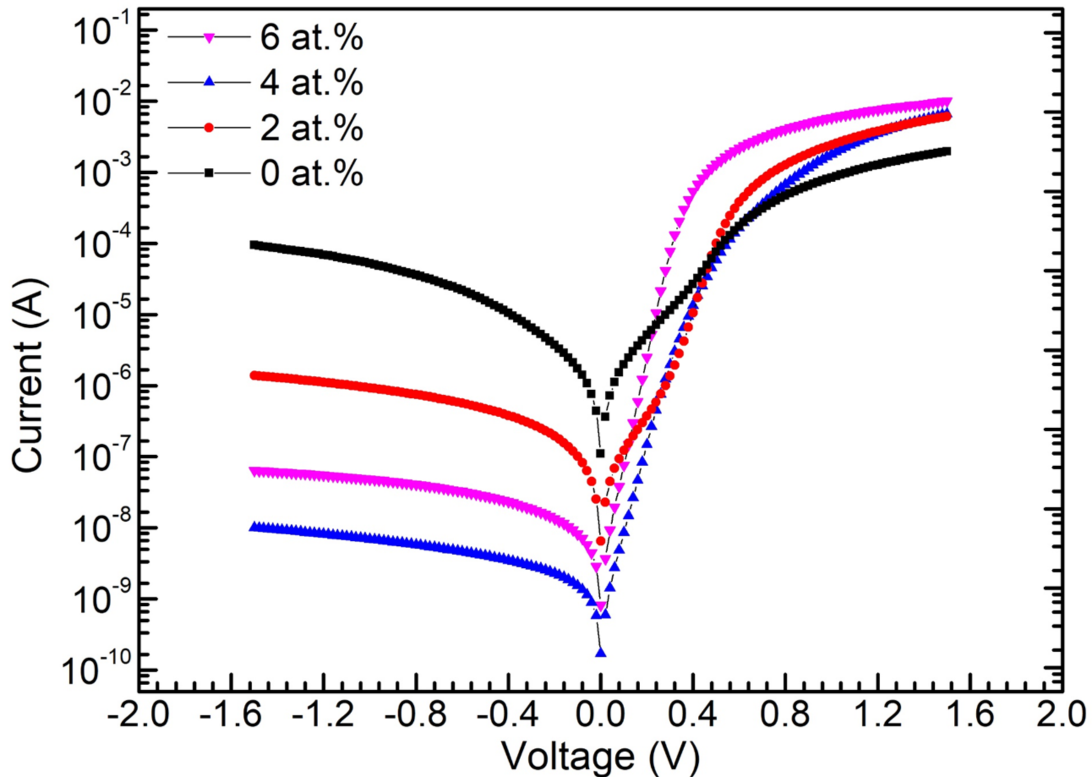


Figure 4.40: Color online) Room temperature semi-logarithmic plot of *I-V* measurements of Pd/(Er, Yb) co-doped ZnO/n-Si/AuSb Schottky diodes.

(Er, Yb) 4 at.% exhibited higher rectification compared with other diodes. The diodes on (Er, Yb) 0 at.% and 2 at.% showed a generation-recombination current transport mechanism at low voltages in the forward bias curve, while the thermionic emission current transport mechanism in the forward bias was dominant in diodes on (Er, Yb) 4 at.% and (Er, Yb) 6 at.%. As shown in Figure 4.40, at high voltage, all the diode characteristics deviated from linearity due to series resistance [12]. The diodes on the undoped material exhibited high leakage current and low SBH compared to the diodes on (Er, Yb) co-doped ZnO thin films. The variation of SBH and ideality factor values with (Er, Yb) doping level is shown in Figure 4.41. As can be seen from Figure 4.41 the SBH increased after co-doping with (Er, Yb). The diodes on co-doped ZnO thin films samples revealed higher SBH of 0.67 eV, 0.68 eV and 0.67 eV for the diodes on (Er, Yb) 2 at.%, 4 at.% and 6 at.%, respectively. The diode on the undoped material

revealed a lower Schottky barrier height of 0.54 eV. As shown in Figure 4.41, the ideality factor decreased with an increase in the (E, Yb) concentrations. The diode on the undoped had a high ideality factor of 3.85. The ideality factor values greater than unity can be attributed to the generation-recombination of electron-hole pairs, inhomogeneities of Schottky barrier height and series resistance [58, 164].

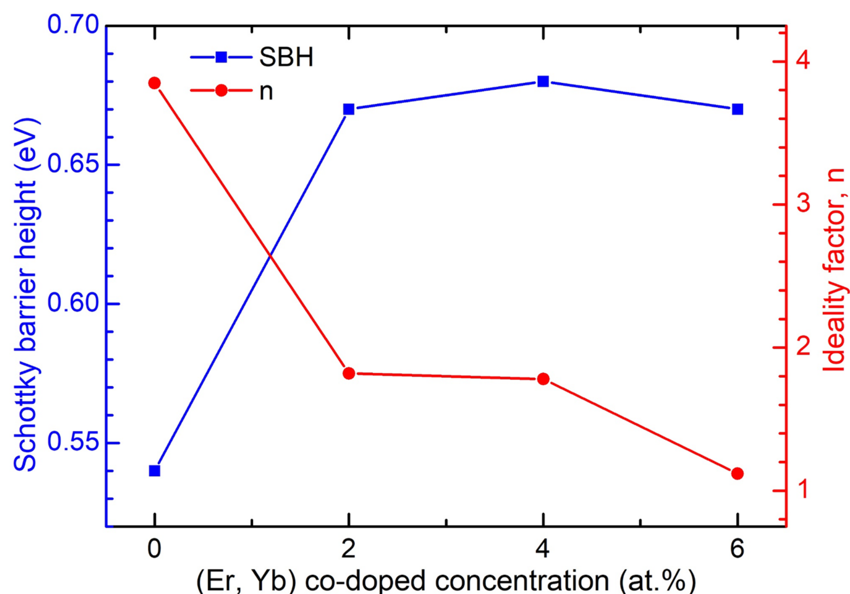


Figure 4.41: Color online) SBH and ideality factor vs (Er, Yb) co-doped concentration plot from the forward bias *I-V* measurements for Pd/(Er, Yb) co-doped ZnO/n-Si/AuSb Schottky diodes.

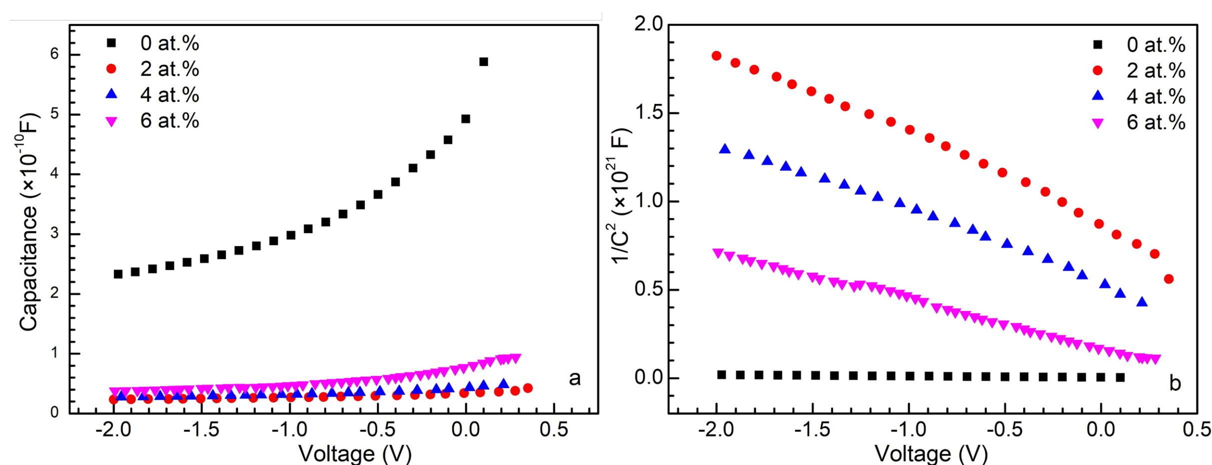


Figure 4.42: (Color online) Room temperature *C-V* measurements of Pd/(Er, Yb) co-doped ZnO/n-Si/AuSb Schottky diodes measured at 1 MHz.

Figure 4.42 shows the *C-V* measurements of Pd/(Er, Yb) co-doped ZnO/n-Si/AuSb Schottky diodes at room temperature measured at 1 MHz. As shown in Figure 4.42 (a) the diodes on (Er, Yb) co-doped ZnO thin films showed lower capacitance compared to the diode on undoped

material. Figure 4.42 (b) shows the plot of $1/C^2$ vs $V$. The carrier concentration and the SBH were obtained from a straight line fit in Figure 4.42 (b) using Equation 2.9. The SBH and carrier concentration obtained are shown in Table 4.13. The diode on undoped ZnO thin films revealed a higher carrier concentration of $2.7 \times 10^{17}$ cm$-3$ compared to those co-doped with Er and Yb. There was a variation between SBH obtained from *C-V* and *I-V* measurements except for the diode on (Er, Yb) 6 at.% that exhibited the same value for the SBH. This variation is attributed to inhomogeneity in SBH [66, 142, 143].

Table 4.13: The Schottky diode parameters determined from *I-V* and *C-V* measurements, measured at room temperature.

| Sample | SBH (eV) | | Ideality | Saturation current, $I_s$ | Series | $N_D$ | Degree of rectification |
|---|---|---|---|---|---|---|---|
| (Er, Yb) at.% | *I-V* | *C-V* | Factor | $\times 10^{-9}$ (A) | Resistance(Ω) | (cm$^{-3}$) | (orders of magnitude) |
| 0 | 0.54 | 0.55 | 3.85 | 450 | 364 | $2.7 \times 10^{17}$ | 1.5 |
| 2 | 0.67 | 1.97 | 1.82 | 2.02 | 106 | $4.3 \times 10^{15}$ | 4 |
| 4 | 0.68 | 1.49 | 1.78 | 2.11 | 95 | $5.2 \times 10^{15}$ | 6 |
| 6 | 0.67 | 0.67 | 1.12 | 2.19 | 115 | $7.0 \times 10^{15}$ | 5 |

### 4.4.5 *DLTS* measurements

The DLTS spectra of (Er, Yb) 2 at.% co-doped ZnO thin films is shown in Figure 4.43. It shows one peak with a level labelled as $E_{0.48}$.

The labelling of defects by (E) refers to an electron trap and subscript number is refers to an activation enthalpy below the conduction band. When investigated by Laplace-transform deep-level transient spectroscopy (L-DLTS), the peak exhibited only one energy level. The activation enthalpies with the apparent cross sections of the $E_{0.48}$ defect have been extracted from the Arrhenius plots shown in Figure 4.44. After analysis of the Arrhenius plot in Figure 4.44, the (Er, Yb) co-doped ZnO defect yielded an activation enthalpy of 0.48 eV and apparent capture cross sections of $2 \times 10^{-16}$ cm$^2$. This defect has been observed in undoped ZnO thin films reported in our previous work in Section 4.1.6 [144]. As previously mentioned this defect is common to ZnO thin films, and could be attributed to the oxygen vacancies [119, 120, 145]. Finally, we want to mention that we didn't obtain DLTS results from the other samples, possibly due to problems arising from instability in the capacitance at low temperature.

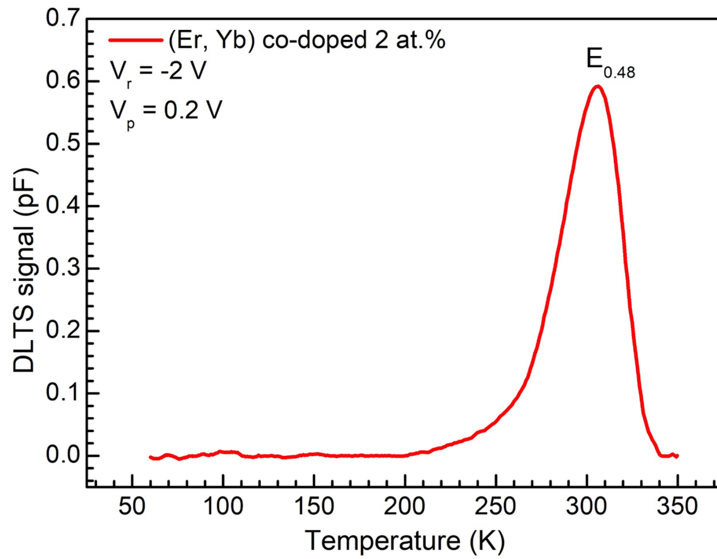


Figure 4.43: DLTS spectra obtained from Pd/(Er, Yb) co-doped ZnO/n-Si/AuSb Schottky diodes, recorded at a quiescent reverse bias $V_r$ = -2 V, filling pulse voltage $V_p$ = 0.2 V, filling pulse width of 1 ms and rate window of 80 Hz in the temperature range of 50 - 350 K.

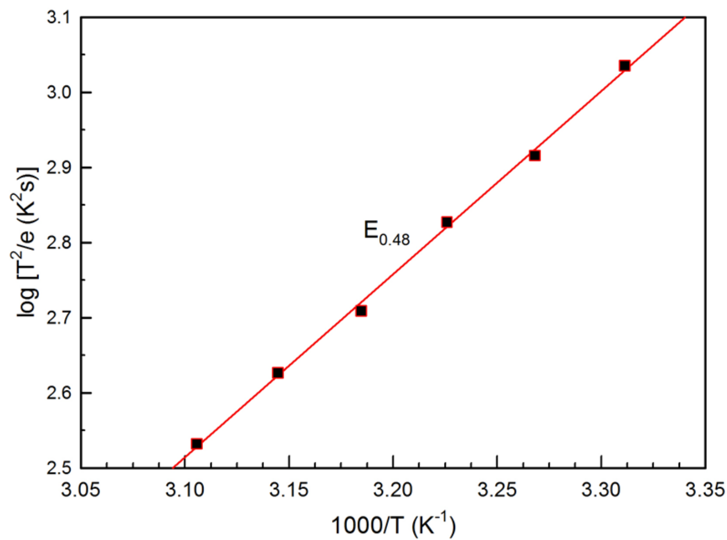


Figure 4.44: Arrhenius plots of the defect in (Er, Yb) 2 at.% co-doped ZnO thin films.

### 4.4.6 Summary

(Er, Yb) co-doped ZnO thin films at different concentrations were successful prepared by the sol-gel spin coating technique. The surface morphology and structure of the (Er, Yb) co-doped ZnO were investigated. From the XRD results, the films had a hexagonal wurtzite structure. The crystallite size decreased as the (Er, Yb) concentration increased. The optical properties were studied using UV-Vis spectroscopy and the optical band gap was found to decrease with increasing (Er, Yb) doping concentration. Schottky diodes were successful

fabricated on undoped and (Er, Yb) co-doped ZnO thin films. The diodes revealed good rectification behavior. SBH increased with increasing doping concentration while the ideality factor decreased. The *C-V* SBH increased after co-doping with (Er, Yb), and the carrier concentration decreased. The diode on (Er, Yb) co-doped ZnO thin films had one peak in its DLTS spectrum with an activation enthalpy of 0.48 eV and apparent capture cross sections of $2 \times 10^{-16}$ cm$^2$. This defect has been previously observed in this study (see Section 4.1.6).

# Chapter 5

# Conclusions and future work

## 5.1 Conclusion

This Chapter presents the general conclusion of the experimental results and future work for this study.

Rectifying contacts on undoped and doped ZnO sol-gel spin coated thin films were fabricated by resistive deposition and characterized using current-voltage *(I-V)* and capacitance-voltage *(C-V)* measurements. The effect of rare-earth (Er and Yb) doping on the structure, optical and electrical properties of the ZnO thin films was studied. The defects on undoped and doped ZnO thin films were studied using DLTS and L-DLTS.

The SEM and XRD results were similar for all samples in this research study. All the films had hexagonal wurtzite ZnO structures and the crystallite size varied from one sample to another depending on the type of dopant or the concentration of the dopant.

For the undoped film, the crystallite size was 48 nm and the thickness 800 nm. The Raman spectrum exhibited a sharp peak corresponding to the $E_2$(high) mode of the wurtzite ZnO structure and other small peaks. The UV-vis spectra showed an absorption peak located in the UV region and the optical band gap obtained from a Tauc plot was 3.23 eV. Alpha particle irradiation caused decrease in Schottky barrier height (SBH) and free carrier concentration ($N_D$), increasing the ideality factor and leakage current. The DLTS and L-DLTS techniques were used to identify the defects in undoped ZnO thin films before and after alpha particle irradiation. It revealed defects before irradiation with an activation enthalpy of 0.41 eV. The defect with an activation enthalpy of 0.35 eV below the conduction band was observed after alpha particle irradiation. The 0.35 eV level was split using L-DLTS and found to consist of

two defects with activaton enthalpies of 0.53 eV and 0.36 eV.

SEM results of the Er-doped and Yb-doped (both in 3 at.%) showed that the doping increased the crystallite size and changed the grain to rod-shaped when annealed at 600 °C. XRD showed a peak related to $Yb_2O_3$, but no evidence of $Er_2O_3$ was found. The crystallite sizes were 42 nm, 51 nm and 54 nm for undoped, Er-doped and Yb-doped ZnO thin films, respectively. The temperature dependence of the electrical properties of Schottky diodes based on Er-doped and Yb-doped (both in 3 at.%) ZnO thin films deposited by the sol-gel technique were investigated over a temperature range of 50 - 290 K in steps of 40 K. The *I-V* characteristics showed that an increase in temperature causes an increase in rectification, the leakage current and Shottky barrier height. However, it causes a decrease in the ideality factor. From the *C-V* characteristics, it was found that the carrier concentration and Shottky barrier height were decreased with increasing temperature. SBH obtained from *C-V* measurements is greater than that SBH obtained from *I-V* measurements. The DLTS and L-DLTS techniques were used to identify the defects in Er-doped ZnO and Yb-doped ZnO thin films. It revealed defect with activation enthalpy of 0.41 eV in Er-doped ZnO thin films, and another defect with activation enthalpy of 0.54 eV in Yb-doped ZnO thin films.

The SEM showed small particles of undoped and Er-doped ZnO thin films. The XRD has shown the films have hexagonal wurtzite structures and crystallite size decreased with increasing Er concentration. The optical properties of Er-doped ZnO thin films with different doping concentrations were studied using UV-Vis spectroscopy. The optical band gap increased as the Er concentration increased. Pd/Er-doped ZnO/n-Si/AuSb Schottky diodes successfully fabricated by resistive deposition on undoped and Er-doped ZnO thin films. The effect of Er doping on the electrical properties of Schottky diodes was studied using *I-V* and *C-V* at room temperature. The diodes exhibited good rectification behavior at room temperature. The Schottky barrier height increased after doping, however, the ideality factor decreased. In order to study the effect of illumination on the Schottky barrier diodes characteristics, the diodes had *I-V* characteristics measured under illuminated and dark conditions. The current values under reverse bias increased as the diodes exhibited a strong response to the illumination. This makes these diodes candidates for photodiode or photosensor applications. The DLTS spectra exhibited one peak in the diodes on the Er 2 at.% and 6 at.%, and two peaks on the diodes on the Er 0 at.% and 4 at.%.

The XRD of (Er, Yb) co-doped ZnO thin films revealed small particles were 12 nm, 10 nm and 7 nm for (Er, Yb)co-doped 2 at.%, 4 at.% and 6 at/%, respectively. XRD results showed that the films have a hexagonal wurtzite structure. The crystallite size decreased as the (Er, Yb) co-doping concentration increased. UV-vis spectroscopy showed a sharp peak in the

UV region and a good transmittance in the visible and IR regions. The optical band gap was found to decreased after co-doped by (Er, Yb). The Schottky diodes fabricated by resistively deposition on undoped and (Er, Yb) co-doped ZnO thin films had a good rectification behavior. The SBH was increased by co-doping, however, the ideality factor decreased. The *C*-*V* SBH increased after co-doping by (Er, Yb), and the carrier concentration decreased after co-doped by (Er, Yb). The diode on (Er, Yb) co-doped ZnO thin films revealed one peak in DLTS spectra with an activation enthalpy of 0.48 eV and apparent capture cross sections of $2 \times 10^{-16}$ cm$^2$.

## 5.2 Future work

- Further characterization of the native and irradiation induced defects on rare-earth doped ZnO thin films using DLTS and L-DLTS techniques.
- More research work required to understand the nature of native defects in rare-earth doped ZnO thin films using the Hall effect technique and photoluminescence spectroscopy.
- Study the effect of thickness on the properties of Schottky barrier diodes.
- Study the effect of post-annealing for deposition thin films on structure, optical and electrical properties of rare-earth doped ZnO thin films.
- Study the effect of post-annealing on the defects on undoped and rare-earth doped ZnO thin films.

# Bibliography

[1] C Klingshirn, R Hauschild, H Priller, J Zeller, M Decker, and Hr Kalt. ZnO rediscovered–once again!? In *Advances in Spectroscopy for Lasers and Sensing*. Springer, 2006.

[2] Ümit Özgür, Ya I Alivov, Chunli Liu, A Teke, MAn Reshchikov, S Doğan, VCSJ Avrutin, S-J Cho, and H Morkoç. A comprehensive review of ZnO materials and devices. *Journal of Applied Physics*, 98:11, 2005.

[3] Chem Klingshirn. ZnO: material, physics and applications. *ChemPhysChem*, 8:782, 2007.

[4] Siti Salwa Alias and Ahmad Azmin Mohamad. *Synthesis of zinc oxide by sol-gel method for photoelectrochemical cells*. Springer, 2014.

[5] Linping Xu, Yan-Ling Hu, Candice Pelligra, Chun-Hu Chen, Lei Jin, Hui Huang, Shanthakumar Sithambaram, Mark Aindow, Raymond Joesten, and Steven L Suib. ZnO with different morphologies synthesized by solvothermal methods for enhanced photocatalytic activity. *Chemistry of Materials*, 21:2875, 2009.

[6] Peter KT Oldring. Coatings, colorants, and paints. In *Encyclopedia of Physical Science and Technology*. Elsevier, 2003.

[7] Klaus Ellmer, Andreas Klein, and Bernd Rech. *Transparent conductive zinc oxide: basics and applications in thin film solar cells*. Springer Science & Business Media, 2007.

[8] M Saleem, L Fang, QL Huang, DC Li, F Wu, HB Ruan, and CY Kong. Annealing treatment of ZnO thin films deposited by sol–gel method. *Surface Review and Letters*, 19:1250055, 2012.

[9] Honglin Li, Zhong Zhang, Jinzhao Huang, Ruxi Liu, and Qingbao Wang. Optical and structural analysis of rare earth and Li co-doped ZnO nanoparticles. *Journal of Alloys and Compounds*, 550:526, 2013.

[10] R Swapna, T SrinivasaReddy, K Venkateswarlu, and MC Santhosh Kumar. Effect of post-annealing on the properties of Eu doped ZnO nano thin films. *Procedia Materials Science*, 10:723, 2015.

[11] Anita Hastir, Nipin Kohli, and Ravi Chand Singh. Comparative study on gas sensing properties of rare earth (Tb, Dy and Er) doped ZnO sensor. *Journal of Physics and Chemistry of Solids*, 105:23, 2017.

[12] Simon M Sze and M. K Lee. *Semiconductor devices physics and technology*. John Wiley & Sons, 2012.

[13] Xin'an Zhang, Fusheng Hai, Ting Zhang, Caihong Jia, Xianwen Sun, Linghong Ding, and Weifeng Zhang. Analysis of the electrical characteristics of the Ag/ZnO Schottky barrier diodes on F-doped $SnO_2$ glass substrates by pulsed laser deposition. *Microelectronic Engineering*, 93:5, 2012.

[14] Caiying Mao, Wanjun Li, Fang Wu, Yuanyao Dou, Liang Fang, Haibo Ruan, and Chunyang Kong. Effect of Er doping on microstructure and optical properties of ZnO thin films prepared by sol–gel method. *Journal of Materials Science: Materials in Electronics*, 26:8732, 2015.

[15] Claus F Klingshirn, Andreas Waag, Axel Hoffmann, and Jean Geurts. *Zinc oxide: from fundamental properties towards novel applications*. Springer Science & Business Media, 2010.

[16] A Segura, JA Sans, FJ Manjon, A Munoz, and MJ Herrera-Cabrera. Optical properties and electronic structure of rock-salt ZnO under pressure. *Applied Physics Letters*, 83:278, 2003.

[17] Mohamed Henini. *Molecular Beam Epitaxy: From Research to Mass Production*. Elsevier, 2018.

[18] SB Kulkarni, UM Patil, RR Salunkhe, SS Joshi, and CD Lokhande. Temperature impact on morphological evolution of ZnO and its consequent effect on physico-chemical properties. *Journal of Alloys and Compounds*, 509:3486, 2011.

[19] Hadis Morkoç and Ümit Özgür. *Zinc oxide: fundamentals, materials and device technology*. John Wiley & Sons, 2008.

[20] Peter Capper, Safa Kasap, and Arthur Willoughby. *Zinc oxide materials for electronic and optoelectronic device applications*. John Wiley & Sons, 2011.

[21] Chennupati Jagadish and Stephen J Pearton. *Zinc oxide bulk, thin films and nanostructures: processing, properties, and applications*. Elsevier, 2011.

[22] Olga Dulub, Lynn A Boatner, and Ulrike Diebold. STM study of the geometric and electronic structure of ZnO (0001)-Zn,(0001)-O,(1010), and (1120) surfaces. *Surface Science*, 519:201, 2002.

[23] Bart Van Zeghbroeck. *Principles of semiconductor devices*. 2004.

[24] Bo E Sernelius, K-F Berggren, Z-C Jin, Ivar Hamberg, and Claes Göran Granqvist. Band-gap tailoring of ZnO by means of heavy Al doping. *Physical Review B*, 37:10244, 1988.

[25] Ben G.. Streetman and Sanjay Banerjee. *Solid state electronic devices*. Pearson Prentice Hall, 2006.

[26] DK Bhattacharya and Rajnish Sharma. *Solid State Electronic Devices*. Oxford University Press, 2013.

[27] Dirk Vogel, Peter Krüger, and Johannes Pollmann. Self-interaction and relaxation-corrected pseudopotentials for II-VI semiconductors. *Physical Review B*, 54:5495, 1996.

[28] V Strelchuk, O Kolomys, S Rarata, P Lytvyn, O Khyzhun, Chan Oeurn Chey, Omer Nur, and Magnus Willander. Raman submicron spatial mapping of individual Mn-doped ZnO nanorods. *Nanoscale Research Letters*, 12:351, 2017.

[29] Fredéric Decremps, Julio Pellicer-Porres, A Marco Saitta, Jean-Claude Chervin, and Alain Polian. High-pressure Raman spectroscopy study of wurtzite ZnO. *Physical Review B*, 65:092101, 2002.

[30] S Bouhouche, F Bensouici, M Toubane, A Azizi, A Otmani, K Chebout, F Kezzoula, R Tala-Ighil, and M Bououdina. Effect of $Er^{+3}$ doping on structural, morphological and photocatalytical properties of ZnO thin films. *Materials Research Express*, 5:056407, 2018.

[31] M Silambarasan, S Saravanan, and T Soga. Raman and photoluminescence studies of Ag and Fe-doped ZnO nanoparticles. *Int. J. Chem. Technol. Res*, 7:1644, 2015.

[32] Yin Song, Shengxia Zhang, Chonghong Zhang, Yitao Yang, and Kangyuan Lv. Raman spectra and microstructure of zinc oxide irradiated with swift heavy ion. *Crystals*, 9:395, 2019.

[33] Kiyotaka Wasa, Makoto Kitabatake, and Hideaki Adachi. *Thin film materials technology: sputtering of control compound materials*. Springer Science & Business Media, 2004.

[34] E Manikandan, MK Moodley, S Sinha Ray, BK Panigrahi, R Krishnan, N Padhy, KGM Nair, and AK Tyagi. Zinc oxide epitaxial thin film deposited over carbon on various substrate by pulsed laser deposition technique. *Journal of Nanoscience and Nanotechnology*, 10:5602, 2010.

[35] RN Gayen, K Sarkar, S Hussain, R Bhar, and AK Pal. ZnO films prepared by modified sol-gel technique. *Journal of the American Planning Association*, 49:470, 2011.

[36] Xiangdong Meng, Bixia Lin, Baijie Gu, Jujie Zhu, and Zhuxi Fu. A simple growth route towards ZnO thin films and nanorods. *Solid State Communications*, 135:411, 2005.

[37] R Ayouchi, D Leinen, F Martın, M Gabas, E Dalchiele, and JR Ramos-Barrado. Preparation and characterization of transparent ZnO thin films obtained by spray pyrolysis. *Thin Solid Films*, 426:68, 2003.

[38] Ke Sun, Wei Wei, Yong Ding, Yi Jing, Zhong Lin Wang, and Deli Wang. Crystalline ZnO thin film by hydrothermal growth. *Chemical Communications*, 47:7776, 2011.

[39] Oleg Lupan, Thierry Pauporté, Lee Chow, Bruno Viana, Fabienne Pellé, Luis K Ono, B Roldan Cuenya, and Helge Heinrich. Effects of annealing on properties of ZnO thin films prepared by electrochemical deposition in chloride medium. *Applied Surface Science*, 256:1895, 2010.

[40] G Murugadoss, R Jayavel, and M Rajesh Kumar. Structural and optical properties of highly crystalline Ce, Eu and co-doped ZnO nanorods. *Superlattices and Microstructures*, 82:538, 2015.

[41] T Ivanova, A Harizanova, T Koutzarova, and Bénédicte Vertruyen. Investigation of sol-gel yttrium doped ZnO thin films: structural and optical properties. *Journal of Physics: Conference Series*, 682:012023, 2016.

[42] Irinela Chilibon and José N Marat-Mendes. Ferroelectric ceramics by sol-gel methods and applications: a review. *Journal of Sol-gel Science and Technology*, 64:571, 2012.

[43] Alejandra López-Suárez, Dwight Acosta, Carlos Magaña, and Francisco Hernández. Optical, structural and electrical properties of ZnO thin films doped with Mn. *Journal of Materials Science: Materials in Electronics*, 31:7389, 2020.

[44] Rita John and Rajaram Rajakumari. Synthesis and characterization of rare earth ion doped nano ZnO. *Nano-Micro Letters*, 4:65, 2012.

[45] Sweta Shukla and Dhirendra Kumar Sharma. A review on rare earth (Ce and Er)-doped zinc oxide nanostructures. *Materials Today: Proceedings*, 34:793, 2021.

[46] Reza Zamiri, AF Lemos, Avito Reblo, Hossein Abbastabar Ahangar, and JMF Ferreira. Effects of rare-earth (Er, La and Yb) doping on morphology and structure properties of ZnO nanostructures prepared by wet chemical method. *Ceramics International*, 40:523, 2014.

[47] A Balakrishna, Trilok K Pathak, E Coetsee-Hugo, Vinod Kumar, RE Kroon, OM Ntwaeaborwa, and HC Swart. Synthesis, structure and optical studies of ZnO: $Eu^{+3}$, $Er^{+3}$, $Yb^{+3}$ thin films: Enhanced up-conversion emission. *Colloids and Surfaces A: Physicochemical and Engineering Aspects*, 540:123, 2018.

[48] Marta Lluscà, J López-Vidrier, Aldrin Antony, S Hernández, B Garrido, and J Bertomeu. Up-conversion effect of Er-and Yb-doped ZnO thin films. *Thin Solid Films*, 562:456, 2014.

[49] SD Senol. Hydrothermal derived nanostructure rare earth (Er, Yb)-doped ZnO: structural, optical and electrical properties. *Journal of Materials Science: Materials in Electronics*, 27:7767, 2016.

[50] Shi-Ling Li, Feng-Min Deng, Yong-Kai Ye, Gang Fu, Bing Liu, Feng-Xiang Wang, and Hai-Long Wang. Optical waveguide and 1.54 $\mu$m photoluminescence properties in RF sputtered Er/Yb-doped ZnO thin films. *Thin Solid Films*, 596:51, 2015.

[51] Reza Zamiri, Avito Rebelo, Hamid Reza Bahari Poor, and JMF Ferreira. Quantum cutting effect and photoluminescence emission at about 1,000 nm from Er-Yb co-doped ZnO nanoplates prepared by wet chemical precipitation method. *Applied Physics A*, 117:2289, 2014.

[52] Vinod Kumar, Anurag Pandey, Sanjay Kumar Swami, OM Ntwaeaborwa, HC Swart, and Viresh Dutta. Synthesis and characterization of $Er^{+3}$-$Yb^{+3}$ doped ZnO upconversion nanoparticles for solar cell application. *Journal of Alloys and Compounds*, 766:429, 2018.

[53] MAM Ahmed, Benard S Mwankemwa, E Carleschi, BP Doyle, Walter Ernst Meyer, and Jackie M Nel. Effect of Sm doping ZnO nanorods on structural optical and electrical properties of Schottky diodes prepared by chemical bath deposition. *Materials Science in Semiconductor Processing*, 79:53, 2018.

[54] Mustafa A Ahmed, Liza Coetsee, Walter E Meyer, and Jackie M Nel. Influence (Ce and Sm) co-doping ZnO nanorods on the structural, optical and electrical properties of the fabricated Schottky diode using chemical bath deposition. *Journal of Alloys and Compounds*, 810:151929, 2019.

[55] Dieter K Schroder. *Semiconductor Material and Device Characterization, Third Edition*. John Wiley & Sons, 2006.

[56] Rolf Enderlein and Norman JM Horing. *Fundamentals of semiconductor physics and devices*. World Scientific, 1997.

[57] BL Sharma. *Metal-semiconductor Schottky barrier junctions and their applications*. Springer Science & Business Media, 2013.

[58] EH Roderick and RH Williams. *Metal-Semiconductor Contacts*. Oxford University Press, 1988.

[59] Simon S Cohen, Gennady Sh Gildenblat, and NG Einspruch. VLSI electronics microstructure science. In *Metal-Semiconductor Contacts and Devices*. Academic, 1986.

[60] Zhen Zhang and John T Yates Jr. Band bending in semiconductors: chemical and physical consequences at surfaces and interfaces. *Chemical Reviews*, 112:5520, 2012.

[61] J-P Colinge and Cynthia A Colinge. *Physics of semiconductor devices*. Springer Science & Business Media, 2005.

[62] Walter Ernst Meyer. *Digital DLTS studies on radiation induced defects in Si, GaAs and GaN*. PhD thesis, University of Pretoria, 2007.

[63] Sheng S Li. *Semiconductor physical electronics*. Springer Science & Business Media, 2012.

[64] Aniruddh Bahadur Yadav, Kunal Singh, Amritanshu Pandey, and S Jit. Annealing-temperature effects on the properties of ZnO thin films and Pd/ZnO Schottky contacts grown on n-Si (1 0 0) substrates by vacuum deposition method. *Superlattices and Microstructures*, 71:250, 2014.

[65] Divya Somvanshi and Satyabrata Jit. Analysis of *I–V* characteristics of Pd/ZnO thin film/n-Si Schottky diodes with series resistance. *Journal of Nanoelectronics and Optoelectronics*, 9:21, 2014.

[66] Şakir Aydoğan, Kübra Çınar, H Asıl, Cevdet Coşkun, and Abdulmecit Türüt. Electrical characterization of Au/n-ZnO Schottky contacts on n-Si. *Journal of Alloys and Compounds*, 476:913, 2009.

[67] Şakir Aydoğan, Maria Luisa Grilli, Mehmet Yilmaz, Zakir Çaldiran, and Hatice Kaçuş. A facile growth of spray based ZnO films and device performance investigation for Schottky diodes: determination of interface state density distribution. *Journal of Alloys and Compounds*, 708:55, 2017.

[68] M Asghar, K Mahmood, Faisal Malik, and MA Hasan. Growth and interface properties of Au Schottky contact on ZnO grown by molecular beam epitaxy. In *Journal of Physics: Conference Series*, volume 439, page 012031. IOP Publishing, 2013.

[69] RuiJuan Zhu, XinAn Zhang, JunWei Zhao, RuoPing Li, and WeiFeng Zhang. Influence of illumination intensity on the electrical characteristics and photoresponsivity of the Ag/ZnO Schottky diodes. *Journal of Alloys and Compounds*, 631:125, 2015.

[70] H Sheng, S Muthukumar, NW Emanetoglu, and Yicheng Lu. Schottky diode with Ag on (1120) epitaxial ZnO film. *Applied Physics Letters*, 80:2132, 2002.

[71] YZ Li, XM Li, and XD Gao. Effects of post-annealing on Schottky contacts of Pt/ZnO films toward UV photodetector. *Journal of Alloys and Compounds*, 509:7193, 2011.

[72] Yasemin Caglar, Mujdat Caglar, and Saliha Ilican. XRD, SEM, XPS studies of Sb doped ZnO films and electrical properties of its based Schottky diodes. *Optik*, 164:424, 2018.

[73] Sheng-Joue Young, Liang-Wen Ji, Shoou-Jinn Chang, YP Chen, and SM Peng. ZnO Schottky diodes with iridium contact electrodes. *Semiconductor Science and Technology*, 23:085016, 2008.

[74] Ezekiel Omotoso. *Electrical characterization of process-and radiation-induced defects in 4H-SiC*. PhD thesis, University of Pretoria, 2015.

[75] Leonard J Brillson and Yicheng Lu. ZnO Schottky barriers and ohmic contacts. *Journal of Applied Physics*, 109:8, 2011.

[76] Hari Singh Nalwa. *Handbook of surfaces and interfaces of materials, five-volume set*. Elsevier, 2001.

[77] A Rogalski and F Sizov. Terahertz detectors and focal plane arrays. *Opto-Electronics Review*, 19:346, 2011.

[78] Sergio Pizzini. *Physical chemistry of semiconductor materials and processes*. John Wiley & Sons, 2015.

[79] Roger Narayan. *Encyclopedia of biomedical engineering*. Elsevier, 2018.

[80] Hans J Queisser and Eugene E Haller. Defects in semiconductors: some fatal, some vital. *Science*, 281:945, 1998.

[81] Musa M Can, S Ismat Shah, Matthew F Doty, Chelsea R Haughn, and Tezer Fırat. Electrical and optical properties of point defects in ZnO thin films. *Journal of Physics D: Applied Physics*, 45:195104, 2012.

[82] Wilbert Mtangi. *Electrical characterization of process, annealing and irradiation induced defects in ZnO*. PhD thesis, University of Pretoria, 2013.

[83] Michel Lannoo. *Point defects in semiconductors I: theoretical aspects*. Springer Science & Business Media, 2012.

[84] Chin-Che Tin. Deep-level transient spectroscopy. In *Characterization of Materials, 2 Volume Set*. Wiley Online Library, 2002.

[85] F Danie Auret and Prakash NK Deenapanray. Deep level transient spectroscopy of defects in high-energy light-particle irradiated Si. *Critical Reviews in Solid State and Materials Sciences*, 29:1, 2004.

[86] DV Lang. Deep-level transient spectroscopy: A new method to characterize traps in semiconductors. *Journal of Applied Physics*, 45:3023, 1974.

[87] Shandirai Malven Tunhuma, M Diale, Matshisa Johannes Legodi, Jackie M Nel, TT Thabete, and Francois Danie Auret. Defects induced by solid state reactions at the tungsten-silicon carbide interface. *Journal of Applied Physics*, 123:161565, 2018.

[88] Cor Claeys and Eddy Simoen. *Metal Impurities in Silicon-and Germanium-Based Technologies*. Springer, 2018.

[89] Yasuhito Zohta and Miyoko Oku Watanabe. On the determination of the spatial distribution of deep centers in semiconducting thin films from capacitance transient spectroscopy. *Journal of Applied Physics*, 53:1809, 1982.

[90] L Dobaczewski, P Kaczor, ID Hawkins, and AR Peaker. Laplace transform deep-level transient spectroscopic studies of defects in semiconductors. *Journal of Applied Physics*, 76:194, 1994.

[91] FD Auret, SA Goodman, M Hayes, MJ Legodi, HA Van Laarhoven, and David C Look. Electrical characterization of 1.8 mev proton-bombarded ZnO. *Applied Physics Letters*, 79:3074, 2001.

[92] Joseph I Goldstein, Dale E Newbury, Joseph R Michael, Nicholas WM Ritchie, John Henry J Scott, and David C Joy. *Scanning electron microscopy and X-ray microanalysis*. Springer, 2017.

[93] Mubarak Yagoub Adam Yagoub. *Effect of broadband excitation ions in the luminescence of $Ln^{3+}$ doped $SrF_2$ nanophosphor for solar cell application*. PhD thesis, University of the Free State, 2015.

[94] BJ Inkson. Scanning electron microscopy (SEM) and transmission electron microscopy (TEM) for materials characterization. In *Materials Characterization Using Nondestructive Evaluation (NDE) Methods*. Elsevier, 2016.

[95] Energy dispersive X-ray spectroscopy (EDX). available from: https://www.copperpodip.com/post/what-is-edx-energy-dispersive-x-ray-spectroscopy.

[96] J Epp. X-ray diffraction (XRD) techniques for materials characterization. In *Materials Characterization Using Nondestructive Evaluation (NDE) Methods*. Elsevier, 2016.

[97] X-Ray diffraction (XRD). available from: https://wiki.anton-paar.com/en/x-ray-diffraction-xrd/.

[98] B.D. Cullity and S.R. Stock. *Elements of X-ray Diffraction, Third Edition*. Prentice-Hall, 2001.

[99] Katherine JI Ember, Marieke A Hoeve, Sarah L McAughtrie, Mads S Bergholt, Benjamin J Dwyer, Molly M Stevens, Karen Faulds, Stuart J Forbes, and Colin J Campbell. Raman spectroscopy and regenerative medicine: a review. *NPJ Regenerative Medicine*, 2:1, 2017.

[100] Jason S Lupoi, Erica Gjersing, and Mark F Davis. Evaluating lignocellulosic biomass, its derivatives, and downstream products with Raman spectroscopy. *Frontiers in Bioengineering and Biotechnology*, 3:50, 2015.

[101] Eric Le Ru and Pablo Etchegoin. *Principles of Surface-Enhanced Raman Spectroscopy: and related plasmonic effects*. Elsevier, 2008.

[102] R Tomovska, A Agirre, A Veloso, and JR Leiza. *Characterization Techniques for Polymeric Materials*. Elsevier, 2014.

[103] K Dyamenahalli, A Famili, and R Shandas. Characterization of shape-memory polymers for biomedical applications. In *Shape Memory Polymers for Biomedical Applications*. Elsevier, 2015.

[104] Jin Zhong Zhang. *Optical properties and spectroscopy of nanomaterials*. World Scientific, 2009.

[105] Brian D Viezbicke, Shane Patel, Benjamin E Davis, and Dunbar P Birnie III. Evaluation of the Tauc method for optical absorption edge determination: ZnO thin films as a model system. *Physica Status Solidi (b)*, 252:1700, 2015.

[106] Fellipy S Rocha, Anderson J Gomes, Claure N Lunardi, Serge Kaliaguine, and Gregory S Patience. Experimental methods in chemical engineering: Ultraviolet visible spectroscopy UV-Vis. *The Canadian Journal of Chemical Engineering*, 96:2512, 2018.

[107] L Dobaczewski, AR Peaker, and K Bonde Nielsen. Laplace-transform deep-level spectroscopy: The technique and its applications to the study of point defects in semiconductors. *Journal of Applied Physics*, 96:4689, 2004.

[108] David C Look, DC Reynolds, Joseph W Hemsky, RL Jones, and JR Sizelove. Production and annealing of electron irradiation damage in ZnO. *Applied Physics Letters*, 75:811, 1999.

[109] Muhammad Saleem, Liang Fang, Aneela Wakeel, M Rashad, and CY Kong. Simple preparation and characterization of nano-crystalline zinc oxide thin films by sol-gel method on glass substrate. *World Journal of Condensed Matter Physics*, 2:10, 2012.

[110] MN Kamalasanan and Subhas Chandra. Sol-gel synthesis of ZnO thin films. *Thin Solid Films*, 288:112, 1996.

[111] M Abdolahpour Salari, Betül Güzeldir, and Mustafa Sağlam. The effects of gamma irradiation on electrical characteristics of Zn/ZnO/n-Si/Au-Sb structure. In *AIP Conference Proceedings*, volume 1935, page 050002. AIP Publishing LLC, 2018.

[112] Huai-Shan Chin and Long-Sun Chao. The effect of thermal annealing processes on structural and photoluminescence of zinc oxide thin film. *Journal of Nanomaterials*, 2013:4, 2013.

[113] Moumita Pal, Susanta Bera, Saswati Sarkar, and Sunirmal Jana. Influence of Al doping on microstructural, optical and photocatalytic properties of sol-gel based nanostructured zinc oxide films on glass. *Rsc Advances*, 4:11552, 2014.

[114] Emre Gür, C Coşkun, and S Tüzemen. High energy electron irradiation effects on electrical properties of Au/n-ZnO Schottky diodes. *Journal of Physics D: Applied Physics*, 41:105301, 2008.

[115] Simon S Cohen and Gennady Sh Gildenblat. *Metal-Semiconductor Contacts and Devices*. Academic Press, 2014.

[116] Richard L Anderson. Experiments on Ge-GaAs heterojunctions. In *Electronic Structure of Semiconductor Heterojunctions*. Springer, 1988.

[117] FZ Bedia, Asma Bedia, Boumediene Benyoucef, and Saad Hamzaoui. Electrical characterization of n-ZnO/p-Si heterojunction prepared by spray pyrolysis technique. *Physics Procedia*, 55:61, 2014.

[118] Min Wei, Chun-Fu Li, Xue-Ran Deng, and Hong Deng. Surface work function of transparent conductive ZnO films. *Energy Procedia*, 16:76, 2012.

[119] Francois Danie Auret, Stewart Alexander Goodman, Matshisa Johannes Legodi, Walter Ernst Meyer, and David C Look. Electrical characterization of vapor-phase-grown single-crystal ZnO. *Applied Physics Letters*, 80:1340, 2002.

[120] Wilbert Mtangi, Francois Danie Auret, Pieter Johan Janse van Rensburg, Sergio MM Coelho, Matshisa Johannes Legodi, JM Nel, WE Meyer, and Albert Chawanda. A comparative study of the electrical properties of Pd/ZnO Schottky contacts fabricated using electron beam deposition and resistive/thermal evaporation techniques. *Journal of Applied Physics*, 110:094504, 2011.

[121] M-B Bouzourâa, Y Battie, S Dalmasso, M-A Zaibi, M Oueslati, and A En Naciri. Temperature dependent optical properties of ZnO thin film using ellipsometry and photoluminescence. *Superlattices and Microstructures*, 117:457, 2018.

[122] Fenglin Xian and Xiangyin Li. Effect of Nd doping level on optical and structural properties of ZnO: Nd thin films synthesized by the sol–gel route. *Optics & Laser Technology*, 45:508, 2013.

[123] E Asikuzun, O Ozturk, L Arda, AT Tasci, F Kartal, and C Terzioglu. High-quality c-axis oriented non-vacuum Er doped ZnO thin films. *Ceramics International*, 42:8085, 2016.

[124] Y Chen and XL Xu. Effect of oxygen deficiency on optical band gap shift in Er-doped ZnO thin films. *Physica B: Condensed Matter*, 406:3121, 2011.

[125] CL Heng, T Wang, WY Su, HC Wu, MC Yang, LG Deng, PG Yin, and TG Finstad. Intense ultraviolet photoluminescent emission from Yb doped ZnO thin films on Si after high temperature annealing. *Journal of Alloys and Compounds*, 695:2232, 2017.

[126] Eugenio H Otal, Elsa Sileo, Myriam H Aguirre, Ismael O Fabregas, and Manuela Kim. Structural characterization and EXAFS wavelet analysis of Yb doped ZnO by wet chemistry route. *Journal of Alloys and Compounds*, 622:115, 2015.

[127] Shinobu Fujihara, Akira Suzuki, and Toshio Kimura. Ga-doping effects on electrical and luminescent properties of ZnO:(La, Eu) of red phosphor thin films. *Journal of Applied Physics*, 94:2411, 2003.

[128] Meehleketo A Mayimele, Mmantsae Diale, Wilbert Mtangi, and Francois D Auret. Temperature-dependent current–voltage characteristics of Pd/ZnO Schottky barrier diodes and the determination of the Richardson constant. *Materials Science in Semiconductor Processing*, 34:359, 2015.

[129] Divya Somvanshi and Satyabrata Jit. Mean barrier height and Richardson constant for Pd/ZnO thin film-based Schottky diodes grown on n-Si substrates by thermal evaporation method. *IEEE Electron Device Letters*, 34:1238, 2013.

[130] Christos Tsiarapas, Dimitra Girginoudi, and Nikolaos Georgoulas. Electrical characteristics of Pd Schottky contacts on ZnO films. *Materials Science in Semiconductor Processing*, 17:199, 2014.

[131] CL Heng, W Xiang, WY Su, HC Wu, YK Gao, PG Yin, and TG Finstad. Strong near band edge emission of (Ce, Yb) co-doped ZnO thin films after high temperature annealing. *Optical Materials Express*, 7:3041, 2017.

[132] Nan Jiang, Song Ye, and Bo Yang. Microstructure of Yb and Li co-doped ZnO by electron microscopy. *Materials Chemistry and Physics*, 142:37, 2013.

[133] Faran Baig, Muhammad Waseem Ashraf, Ali Asif, and Muhammad Imran. A comparative analysis for effects of solvents on optical properties of Mg doped ZnO thin films for optoelectronic applications. *Optik*, 208:164534, 2020.

[134] Parmod Kumar, Vikas Sharma, Ankita Sarwa, Ashish Kumar, Rajan Goyal, K Sachdev, S Annapoorni, K Asokan, D Kanjilal, et al. Understanding the origin of ferromagnetism in Er-doped ZnO system. *RSC Advances*, 6:89242, 2016.

[135] Jing Zhao, Xiaoqin Yan, Ya Yang, Yunhua Huang, and Yue Zhang. Raman spectra and photoluminescence properties of In-doped ZnO nanostructures. *Materials Letters*, 64:569, 2010.

[136] Reza Zamiri, Ajay Kaushal, Avito Rebelo, and JMF Ferreira. Er doped ZnO nanoplates: Synthesis, optical and dielectric properties. *Ceramics International*, 40:1635, 2014.

[137] Youjin Zheng, Qiang Lü, Jialiang Wang, Guohai Zhang, Yang Gao, and Zhanbo Liu. Emission behaviors of $Yb_2O_3$ nanoparticles pumped by 980 nm laser at different power densities. *Optics & Laser Technology*, 63:39, 2014.

[138] RT Tung. Electron transport at metal-semiconductor interfaces: General theory. *Physical Review B*, 45:13509, 1992.

[139] Murat Gülnahar. Temperature dependence of current-and capacitance–voltage characteristics of an Au/4H-SiC Schottky diode. *Superlattices and Microstructures*, 76:394, 2014.

[140] Jun Chen, Qingsong Wang, Jiabing Lv, Hengjing Tang, and Xue Li. Current–voltage–temperature and capacitance–voltage–temperature characteristics of TiW alloy/p-InP Schottky barrier diode. *Journal of Alloys and Compounds*, 649:1220, 2015.

[141] Adem Kocyigit, Ikram Orak, Şakir Aydoğan, Z Çaldıran, and Abdulmecit Turut. Temperature-dependent *C-V* characteristics of Au/ZnO/n-Si device obtained by atomic

layer deposition technique. *Journal of Materials Science: Materials in Electronics*, 28:5880, 2017.

[142] Cevdet Coskun, Nebi Gedik, and Ercan Balcı. The effect of high-energy electron irradiation on ZnO-based ohmic and Schottky contacts. *Semiconductor Science and Technology*, 21:1656, 2006.

[143] E Omotoso, FD Auret, E Igumbor, SM Tunhuma, HT Danga, PNM Ngoepe, BA Taleatu, and WE Meyer. The influence of thermal annealing on the characteristics of Au/Ni Schottky contacts on n-type 4H-SiC. *Applied Physics A*, 124:395, 2018.

[144] MEI Ahmed, Fatemeh Taghizadeh, Francois Danie Auret, Walter Ernst Meyer, and Jackie M Nel. The effect of alpha particle irradiation on electrical properties and defects of ZnO thin films prepared by sol-gel spin coating. *Materials Science in Semiconductor Processing*, 101:82, 2019.

[145] Colin Leach, Karen D Vernon-Parry, and Naheed K Ali. Deep level transient spectroscopy study of the effect of Mn and Bi doping on trap formation in ZnO. *Journal of Electroceramics*, 25:188, 2010.

[146] L Scheffler, Vl Kolkovsky, EV Lavrov, and J Weber. Deep level transient spectroscopy studies of n-type ZnO single crystals grown by different techniques. *Journal of Physics: Condensed Matter*, 23:334208, 2011.

[147] Christos Tsiarapas, Dimitra Girginoudi, Evangelos Ioannou Dimitriadis, and Nikolaos Georgoulas. Investigation on deep level defects in polycrystalline ZnO thin films. *Journal of Vacuum Science & Technology B, Nanotechnology and Microelectronics: Materials, Processing, Measurement, and Phenomena*, 35:031203, 2017.

[148] E Hasabeldaim, OM Ntwaeaborwa, RE Kroon, and HC Swart. Structural, optical and photoluminescence properties of Eu doped ZnO thin films prepared by spin coating. *Journal of Molecular Structure*, 1192:105, 2019.

[149] Shuji Komuro, Tooru Katsumata, Takitaro Morikawa, Xinwei Zhao, Hideo Isshiki, and Yoshinobu Aoyagi. 1.54 $\mu$m emission dynamics of erbium-doped zinc-oxide thin films. *Applied Physics Letters*, 76:3935, 2000.

[150] R Vettumperumal, S Kalyanaraman, and R Thangavel. Optical constants and near infrared emission of Er doped ZnO sol-gel thin films. *Journal of Luminescence*, 158:493, 2015.

[151] Y Chen, XL Xu, GH Zhang, H Xue, and SY Ma. Blue shift of optical band gap in Er-doped ZnO thin films deposited by direct current reactive magnetron sputtering technique. *Physica E: Low-Dimensional Systems and Nanostructures*, 42:1713, 2010.

[152] Lei Miao, Sakae Tanemura, Lili Zhao, Xiudi Xiao, and Xiao Ting Zhang. Ellipsometric studies of optical properties of Er-doped ZnO thin films synthesized by sol–gel method. *Thin Solid Films*, 543:125, 2013.

[153] S Fareed, Arifa Jamil, Naveen Tiwari, and MA Rafiq. Influence of Cr doping on Schottky barrier height and visible light detection of ZnO thin films deposited by magnetron sputtering. *Micro and Nano Engineering*, 2:48, 2019.

[154] Ivan Procházka, J Cizek, F Lukac, Oksana Melikhova, Jan Valenta, Vladimír Havránek, Wolfgang Anwand, Vladimir A Skuratov, and Tatiana S Strukova. Characterisation of irradiation-induced defects in ZnO single crystals. *Journal of Physics: Conference Series*, 674:012014, 2016.

[155] Jidong Jin, Jacqueline S Wrench, James T Gibbon, David Hesp, Andrew Shaw, Ivona Z Mitrovic, Naser Sedghi, Laurie J Phillips, Jianli Zou, Vinod R Dhanak, et al. Schottky diodes on ZnO thin films grown by plasma-enhanced atomic layer deposition. *IEEE Transactions on Electron Devices*, 64:1225, 2017.

[156] Lintu Rajan, C Periasamy, and Vineet Sahula. Electrical characterization of Au/ZnO thin film Schottky diode on silicon substrate. *Perspectives in Science*, 8:66, 2016.

[157] Mustafa A. Ahmed, Walter Meyer, and J.M. Nel. Structural, optical and electrical properties of a Schottky diode fabricated on Ce doped ZnO nanorods grown using a two step chemical bath deposition. *Materials Science in Semiconductor Processing*, 87:187, 2018.

[158] C Jayachandraiah and Dr Krishnaiah. Erbium induced Raman studies and dielectric properties of Er-doped ZnO nanoparticles. *Advanced Materials Letters*, 6:743, 2015.

[159] NK Divya and PP Pradyumnan. Solid state synthesis of erbium doped ZnO with excellent photocatalytic activity and enhanced visible light emission. *Materials Science in Semiconductor Processing*, 41:428, 2016.

[160] J Sivasankari, S Sankar, S Selvakumar, L Vimaladevi, and R Krithiga. Synthesis, structural and optical properties of Er doped, Li doped and Er + Li co-doped ZnO nanocrystallites by solution-combustion method. *Materials Chemistry and Physics*, 143:1528, 2014.

[161] Chien-Yie Tsay and Wen-Che Lee. Effect of dopants on the structural, optical and electrical properties of sol–gel derived ZnO semiconductor thin films. *Current Applied Physics*, 13:60, 2013.

[162] Saman Habashyani, Ahmet Özmen, Sakir Aydogan, and Mehmet Yilmaz. An examination of correlation between characteristic and device performance of ZnO films as a function of La content. *Vacuum*, 157:497, 2018.

[163] H-Y He, J-F Huang, J Fei, and J Lu. La-doping content effect on the optical and electrical properties of La-doped ZnO thin films. *Journal of Materials Science: Materials in Electronics*, 26:1205, 2015.

[164] Havva Elif Lapa, Ali Kökce, Durmuş Ali Aldemir, Ahmet Faruk Özdemir, and Şemsettin Altındal. Effect of illumination on electrical parameters of Au/(P3DMTFT)/n-GaAs Schottky barrier diodes. *Indian Journal of Physics*, 94:1901, 2020.

[165] Enise Ozerden, Yusuf Selim Ocak, Ahmet Tombak, Tahsin Kilicoglu, and Abdulmecit Turut. Electrical and photoelectrical properties of Ag/n-type Si metal/semiconductor contact with organic interlayer. *Thin Solid Films*, 597:14, 2015.

[166] Chih-Hsien Chen and I Shih. Hybrid organic on inorganic semiconductor heterojunction. *Journal of Materials Science: Materials in Electronics*, 17:1047, 2006.

[167] Irshad Ahmad. Inexpensive and quick photocatalytic activity of rare earth (Er, Yb) co-doped ZnO nanoparticles for degradation of methyl orange dye. *Separation and Purification Technology*, 227:115726, 2019.

[168] Xiuqing Meng, Chaoren Liu, Fengmin Wu, and Jingbo Li. Strong up-conversion emissions in ZnO: $Er^{+3}$, ZnO: $Er^{+3}$–$Yb^{+3}$ nanoparticles and their surface modified counterparts. *Journal of Colloid and Interface Science*, 358:334, 2011.

[169] Krisana Kobwittaya, Yushi Oishi, Toshio Torikai, Mitsunori Yada, Takanori Watari, and Hom Nath Luitel. Bright red upconversion luminescence from $Er^{+3}$ and $Yb^{+3}$ co-doped ZnO-$TiO_2$ composite phosphor powder. *Ceramics International*, 43:13505, 2017.

[170] MAM Ahmed, Walter Ernst Meyer, and Jackie M Nel. Structural, optical and electrical properties of the fabricated Schottky diodes based on ZnO, Ce and Sm doped ZnO films prepared via wet chemical technique. *Materials Research Bulletin*, 115:12, 2019.

[171] RK Kalaiezhily, G Saravanan, V Asvini, N Vijayan, and K Ravichandran. Tuning violet to green emission in luminomagnetic Dy, Er co-doped ZnO nanoparticles. *Ceramics International*, 44:19560, 2018.

[172] BD Cullity and SR Stock. *Elements of X-ray diffraction*. Pearson, 2001.

[173] E Asikuzun, O Ozturk, L Arda, and C Terzioglu. Preparation, growth and characterization of nonvacuum Cu-doped ZnO thin films. *Journal of Molecular Structure*, 1165:1, 2018.

[174] Li-Sha Zhang, Kin-Hang Wong, Ho-Yin Yip, Chun Hu, Jimmy C Yu, Chiu-Yeung Chan, and Po-Keung Wong. Effective photocatalytic disinfection of E. coli K-12 using AgBr-Ag- $Bi_2WO_6$ nanojunction system irradiated by visible light: the role of diffusing hydroxyl radicals. *Environmental Science & Technology*, 44:1392, 2010.